FACULTY OF ENGINEERING
AND ARCHITECTURE

A Combined Experimental and Computational Study on the Feasibility of Carotid Stenosis Detection by Means of Laser Doppler Vibrometry

Viviana Mancini

Doctoral dissertation submitted to obtain the academic degree of
Doctor of Biomedical Engineering

Supervisors
Prof. Patrick Segers, PhD* - Kristian Valen-Sendstad, PhD**

* Department of Electronics and Information Systems
Faculty of Engineering and Architecture, Ghent University
** Simula Research Laboratory, Norway

December 2020

GHENT
UNIVERSITY

ISBN 978-94-6355-443-5
NUR 954
Wettelijk depot: D/2020/10.500/120

Members of the Examination Board

Chair

Honoray prof. Ronny Verhoeven, PhD, Ghent University

Other members entitled to vote

Prof. Charlotte Debbaut, PhD, Ghent University
Prof. Joris Degroote, PhD, Ghent University
Prof. Stephen Greenwald, PhD, Queen Mary University of London, United Kingdom
Prof. Umberto Morbiducci, PhD, Politecnico di Torino, Italy
Prof. Frans van de Vosse, PhD, Technische Universiteit Eindhoven, the Netherlands

Supervisors

Prof. Patrick Segers, PhD, Ghent University
Kristian Valen-Sendstad, PhD, Simula Research Laboratory, Norway

PREFACE

Doing a PhD has been an extraordinary and rewarding journey, which allowed me to grow both professionally and personally, and - hopefully - to provide something useful to others. I would like to express my gratitude to the amazing people who have supported and guided me throughout these years.

First of all, I would like to thank my supervisors. Patrick met me online in a Skype interview, to which my housemates felt the debatable urge to participate as well by walking behind me. Besides that first impression, he allowed me to join the bioMMeda group at UGent, and he guided me in any aspect of the PhD life, encouraging my critical thinking after our many scientific discussions. I am very grateful also for introducing me to the "unstable" fluid dynamical world, allowing me to meet Kristian, who since then has been teaching and guiding me (despite the commute from Ghent to Oslo is not feasible on an every-day basis). The month I spent at Simula was a thrilling experience, which then became a long-lasting fruitful collaboration, to which I owe so much for the success of my PhD. I would like to thank Jan, who showed great interest and empathy during the limited time I had the honor to work with him.

Thanks to the jury members of this PhD committee for their time and interest in this research, and for the valuable comments and revisions of my PhD thesis, with a special mention to Steve who has been following the development of the study since its first weeks.

I would like to extend my thanks to the entire CARDIS consortium, for their valuable comments and suggestions throughout the project, and for the enjoyable time together. I now have an admirable knowledge in coffee beans thanks to Yanlu, Louise and Daniela.

A special thank to Aslak, who has been able to not lose his temper too often. Thank you for being there despite the challenges of your own PhD. I wish you the best of luck.

Many thanks to all my past and present colleagues at bioMMeda for the coffee breaks, the chats and the companionship. To Jurgen and Saskia for the support, to Hicham, Carlos, Alessio and Giorgia for the Italian office chats, to Darya for her shopping support, to Gerlinde and Lise for the amazing photograph I have now on my desk, to Daime for the intense BBB sessions, to Ghazal and Amith for the beers together, to Matthias for not getting mad because I still have no clue on how to spell his name correctly (hopefully I got it right here), to David and Nic for being there for any doubt in my first weeks, to Danilo for his price-winner Lasagna, to Federico who changed office after a few months for "mysterious" reasons. How not to mention the great hikes we had at the Smoky Mountains with Alessandra, and the amazing trip to the Grand Canyon at 5am with Annette and Mathias. Thank you all for having made the office life so fun!

Many thanks also to my current colleagues at Livanova, for their support in this final stage of the PhD.

I would like to thank my Dutch-learning Gentenaar friends Jackie, Vish and Mercedes for their great friendship which made Belgium look more like home. Thanks from Federico to Jose', Maria and Nuno for making me do the parmigiana (ok ok from me too). Thanks to Bart, who let me be a princess just for one day. Thanks to Annalucia and Lorenzo, for showing me that life sometimes can be difficult, but together it is possible to overcome everything.

Many thanks to my Italian friends, who have waited for this moment as much as I have. To Guido and Celine for their support. To Silvia for having answered to random calls at any time of the day despite the chaos of her huge life changes, and to Bruno for having let her talk on the phone for a little longer. To Giorgio, Corrado, Bruna and the rest of the gang, for having welcomed me back in Milan. To Gabriella, Valentina, Giuliana, Fabiola, Marco, Emanuele, Vincenzo, Francesco, Alberto and Vittorio for the trips together, and in general for being there always. To Gabriella, for the laughs and the tears, or simply for being family.

Un grazie a Mariangela per la sua grinta e a Umbi per avermi fatto riscoprire Spiderman. A Gabriella e tutti i Rossi per la loro energia travolgente. A Fabio e Emanuela per il supporto e i consigli.

Uno speciale ringraziamento va alla mia famiglia, nonna e nonni, zii, cugini e parenti, per essermi stati vicini in questi anni lontano da casa. A mamma, papa' e Cinzia per essere la mia ancora nella tempesta e per aver saputo lasciarmi volare quando necessario. Per aver sempre creduto in me, spero di avervi resi orgogliosi. Vi devo tutto.

E infine grazie a Federico, per essere stato molto piu' di un compagno di viaggio, un esempio di perseveranza, il mio porto sicuro. Questi ultimi tempi non sono stati certo facili, ma il futuro con te fa meno paura.

Viviana, December 2020

TABLE OF CONTENTS

Preface xi

Table of contents xiii

List of Figures xvii

List of Tables xix

Abbreviations and symbols xxi

Summary xxiii

Samenvatting xxvii

Introduction xxxi

I Background 1

1 Clinical rationale 3
- 1.1 Cardiovascular system 3
- 1.2 Carotid arteries 8
- 1.3 Stenosis 10
- 1.4 Carotid stenosis and stroke: current treatments and diagnostic procedures 14

2 Fluid dynamics in the cardiovascular system 17
- 2.1 Navier-Stokes equations 17
  - 2.1.1 Continuity equation 18
  - 2.1.2 Momentum equation 19
  - 2.1.3 Simplifications leading to Poiseulle's law 19
- 2.2 Flow regimes 22
  - 2.2.1 Pipe flow 22

2.2.2 Sudden contraction and sudden expansion 24
2.2.3 Curvature 24
2.2.4 Pulsatility 25
2.3 Blood flow in the cardiovascular system 25
2.3.1 Carotid aneurysms 28
2.3.2 Atherosclerosis and carotid stenosis 28
2.4 Fluid dynamics of stenotic carotid arteries 29
2.5 Existence and smoothness problem of the Navier-Stokes equations 30
2.6 Kolmogorov's theory on turbulent energy cascade 30

3 Rationale for a numerical approach 33
3.1 Analytical approach 33
3.2 Experimental approach 33
3.3 Numerical approach 34
3.4 A CFD parametric study of an experimental technology: a combined effort 38

II Flow instabilities: predictors of carotid stenosis 41

4 High-frequency instabilities: a strategy in-silico study 43
4.1 Introduction 43
4.2 Methods 45
4.3 Results 50
4.3.1 General Flow Features 50
4.3.2 Sensitivity Analysis 51
4.3.2.1 Spatial Refinement Study 51
4.3.2.2 Temporal Refinement Study 54
4.3.3 Large Eddy Simulations 54
4.3.3.1 Constant Flow Simulations 54
4.3.3.2 Pulsatile Flow Simulations 57
4.4 Discussion 59
4.5 Conclusions 64
4.6 Appendix A 65
4.6.1 Mesh sensitivity analysis 65
4.6.2 Time step sensitivity analysis 65
4.6.3 Sub grid scale models 65
4.7 Appendix B 72

5 Laser Doppler vibrometry: a feasibility in-vitro study 75
5.1 Introduction 75

5.2 Materials and methods 77
  5.2.1 Model reconstruction 77
  5.2.2 Experimental set-up 78
  5.2.3 Flow conditions 79
  5.2.4 Signal Processing 81
    5.2.4.1 Power Spectral Density 81
  5.2.5 Statistical analysis 82
5.3 Results 83
  5.3.1 Spectrograms 84
  5.3.2 Normalized Spectra 84
  5.3.3 Sensitivity Analysis 85
    5.3.3.1 Compliant vs. Stiff models 85
    5.3.3.2 Measurement location 87
5.4 Discussion 87
5.5 Acknowledgements 92

6 Flow instabilities for stenosis detection: a combined approach 93
6.1 Introduction 94
6.2 Materials and Methods 95
  6.2.1 Computational Fluid Dynamical Model 95
  6.2.2 Post Processing of Computational Data 97
  6.2.3 Validation against Computational Data 99
  6.2.4 Metrics Correlating with Flow Instabilities 100
  6.2.5 Proof-of-concept for Sensitivity, Specificity and Accuracy of an LDV Device for Stenosis Detection . . . 101
6.3 Results 102
  6.3.1 Computational Findings 102
  6.3.2 Validation against in-vitro Experiments 102
  6.3.3 Metrics Correlating with Flow Instabilities in Stenosed and Healthy Models 104
    6.3.3.1 Frequency-Based Stenosis Indicators . . . 107
    6.3.3.2 LDV for Stenosis Detection: Proof-of-concept 109
6.4 Discussion 111
  6.4.1 Validation Strategy 111
  6.4.2 Computational Model 111
  6.4.3 Healthy Model 112
  6.4.4 Reynolds Number 112
  6.4.5 Fictitious Population 112
  6.4.6 Future Work 113
6.5 Conclusions 115
6.6 Acknowledgements 116

Conclusions **119**
Research Goals 119
What about the clinical practice? 121
Take-home message 122

Bibliography **123**

LIST OF FIGURES

1.1 Systemic Circulation 5
1.2 Structure of blood vessels 6
1.3 Elastic versus muscular arteries 7
1.4 Right common carotid artery 8
1.5 Typical waveforms of the carotid arteries 9
1.6 Stenosis morphology 11
1.7 Plaque composition 11
1.8 Stenosis severity 12
1.9 Stenosis extension 13
1.10 Procedures for carotid stenosis 15

2.1 Flow in a pipe 18
2.2 Laminar, Unstable, or Turbulent Flow 23
2.3 Sudden contraction or expansion 24
2.4 Geometrical risk factors 26
2.5 Complex flow in the carotid bifurcation I 26
2.6 Complex flow in the carotid bifurcation II 27
2.7 Aneurysm initiation 28
2.8 Laminar or Unstable Stenotic Flow 29
2.9 Energy cascade in turbulent flows 32

3.1 Experiments on rigid-pipe stenosis in 1983 34
3.2 Flowchart of a CFD simulation 35
3.3 Numerical discretization methodologies 36
3.4 DNS and LES for turbulent scales 38

4.1 Patient-specific stenotic carotid bifurcation 46
4.2 Typical carotid artery waveform 47
4.3 Signal decomposition 50
4.4 General flow features 51
4.5 Sensitivity analysis - vortical structures 52
4.6 Sensitivity analysis - time-averaged tke 53
4.7 Sensitivity analysis - Power Spectral Density 54

4.8 Sub-Grid Scale Models - added viscosity and resulting flow field 55
4.9 Sub-Grid Scale Models - time-averaged tke 56
4.10 Sub-Grid Scale Models - vortical structures 57
4.11 Sub-Grid Scale Models - ν_{SGS}, time-averaged tke and tke' 58
4.12 Spatial sensitivity analysis - tke 66
4.13 Temporal sensitivity analysis - tke 67
4.14 Sub-grid scale models - ν_{SGS} for constant and pulsatile flow rates 68
4.15 Sub-grid scale models - tke for constant and pulsatile flow rates 69
4.16 Sub-grid scale models - tke' for constant and pulsatile flow rates 70
4.17 Dimensioneless cell sizes $l+$ 71
4.18 Power Spectral Density - additional centerline locations 72
4.19 Power Spectral Density at -3.6d 72
4.20 Power Spectral Density at -1.4d 73
4.21 Power Spectral Density at 0.6d 73
4.22 Power Spectral Density at 2.6d 74
4.23 Power Spectral Density at 4.6d 74

5.1 Patient-specific *in-vitro* model 78
5.2 The assembled experimental loop 80
5.3 Recorded time traces 81
5.4 Signal processing workflow 83
5.5 Spectrograms 85
5.6 Normalized spectra 86
5.7 Sensitivity to flow rate 86
5.8 Estimated Marginal Means 88

6.1 *In-silico* models 96
6.2 Postprocessing 99
6.3 Overview of CFD results 103
6.4 Validation 104
6.5 Metrics Correlating With Flow Instabilities 106
6.6 Q_{ICA} Correlating With Flow Instabilities 107
6.7 Flow Instabilities at several Degrees of Stenosis 108
6.8 Estimate of LDV Prediction Ability 110

LIST OF TABLES

2.1 Reynolds number 23

4.1 Mesh characteristics 46
4.2 Simulations details 48
4.3 List of simulations 49
4.4 Computational cost - constant flow rate 57
4.5 Computational cost - pulsatile flow rate 59
4.6 Richardson extrapolation 61

5.1 Test conditions overview 84
5.2 Significance value of $Freq \cdot Q_{ICA}$ 90

6.1 List of CFD data 98
6.2 Estimate of LDV prediction accuracy 98
6.3 List of EXP data 100
6.4 Correlation between Q_{ICA} and IFI to obtain fictitious population 111

ABBREVIATIONS AND SYMBOLS

The following list summarizes the most commonly used abbreviations and symbols in this thesis.

Abbreviations

CARDIS	Early stage CARdio vascular disease Detection with Integrated Silicon photonics
CCA	Common Carotid Artery
CFD	Computational Fluid Dynamics
CPU	Central Processing Unit
CVD	Cardiovascular Disease
CVS	Cardiovascular System
dB	decibels
DNS	Direct Numerical Simulation
ECA	External Carotid Artery
EMMs	Estimated Marginal Means
EXP	Experimental
FDA	Food & Drug Administration
FFT	Fast Fourier transform
FSI	Fluid Structure Interaction
ICA	Internal Carotid Artery
K	Thousand
LDV	Laser Doppler Vibrometry
LES	Large Eddy Simulation
M	Million
PDE	Partial Differential Equation
PP	Pulse Pressure
PSD	Power Spectral Density
ROC	Receiver Operating Characteristics
SD	Standard Deviation
SGS	Sub-Grid Scale

Symbols

μ	Dynamic Viscosity	[kg/m/s]
ν	Kinematic Viscosity	[m^2/s]
ν_{SGS}	Sub-Grid Scale Kinematic Viscosity	[m^2/s]
$\vec{g}$	Gravity Vector	[m/s^2]
$\vec{v}$	Velocity Vector	[m/s]
ρ	Density	[kg/m^3]
Δt	Time step size	[s]
Δ	Sub-Grid Scale model cut-off length scale	[m]
AUC	Area Under The Curve	[-]
BP	Blood Pressure	[mmHg]
C_m	Sub-Grid Scale model constant	[-]
CO	Cardiac Output	[ml/min]
D	Arterial Diameter	[m]
D_m	Sub-Grid Scale model specific differential operator	[-]
E	Young's Elasticity modulus	[Pa]
FP	False Positive	[-]
HR	Heart Rate	[1/min]
J	Youden Index	[-]
L	Arterial Length	[m]
L_S	Stenosis Length	[m]
p	Measured order of convergence	[-]
Q	Volumetric Flow rate	[m^3/s]
R	Lumen Resistance	[kg/m^4/s]
Re	Reynolds number	[-]
S_{ij}	Strain tensor of the resolved scales	[Pa]
Sn	Sensitivity	[-]
Sp	Specificity	[-]
SV	Stroke Volume	[ml]
tke	Turbulent kinetic energy	[m^2/s^2]
tke'	High-pass filtered tke	[m^2/s^2]
TP	True Positive	[-]
v	Velocity Magnitude	[m/s]
w	Flow Pulsation	[1/s]
Wo	Womersley number	[-]
WSS	Wall Shear Stress	[Pa]
e	Dissipation rate	[m^2/s^3]

SUMMARY

INTRODUCTION

Early detection of asymptomatic carotid stenosis is crucial for treatment planning in the prevention of ischemic stroke. Auscultation, the current first-line screening methodology, comes with severe limitations that urge for novel and robust techniques. Laser Doppler vibrometry (LDV) is a promising method for inferring carotid stenosis by measuring stenosis-induced vibrations.

Within the context of an H2020 funded Early stage CARdio Vascular Disease Detection with Integrated Silicon Photonics (CARDIS) project, we have developed a compact multi-beam array prototype LDV system based on an optical chip and suitable for use in a clinical setting for, among other things, measurement of arterial stiffness.

The goal of the current thesis was to evaluate the feasibility of LDV for carotid stenosis detection. The intended use for such device would be first-line cardiovascular screening, identifying individuals at risk so that they can be referred to specialized centers for further follow-up using dedicated and established diagnostic techniques such as ultrasound, magnetic resonance imaging or computed tomography angiography.

Specifically, we focused on the development and validation of a computational methodology to gain a deeper understanding the intensity of flow instabilities as a predictor for carotid stenosis, and assessing the ability of LDV to measure flow instabilities at skin level on the neck.

This dissertation is composed of three main parts. Part I provides a general introduction on carotid stenosis and explains the principles behind the physical phenomena under investigation. This part also provides an overview of the combined experimental and computational workflow for investigating complex fluid dynamical problems. Part II presents the developments obtained throughout the PhD as a result of the collaboration between the Ghent University, Simula Research Laboratory and the Queen Mary University of London. The last part offers an overview of the main results, with special attention to the applicability of the results to the clinical practice. Below, a summary of each part and chapter is provided.

PART I - BACKGROUND

Clinical rationale

This chapter provides the basis of the anatomy and physiology of the human arterial tree, which is necessary to understand and follow the work described in this dissertation. It continues by explaining the pathologic condition of the carotid artery stenosis, and its devastating consequences if not promptly detected and treated. An overview of the possible current diagnostic procedures shows the necessity for novel methodologies.

Fluid dynamics in the cardiovascular system

The understanding of the fluid dynamics phenomena related to carotid stenosis is the primary focus of this chapter. The carotid arteries are prone to the onset of disturbed flow regimes as a result of geometrical factors, despite facing a relatively low Reynolds number. As a result, aneurysms and stenoses develop in the carotid arteries, further disturbing the blood flow. The Navier-Stokes equations describe the fluid dynamical phenomena. The applicability of the analytical Navier-Stokes equations is limited to simple viscous\laminar problems, whilst instability and turbulence are relatively complex ones. Therefore, turbulence models, such as the one of Kolomogorov, have been developed to describe how the kinetic energy behaves at the several scales of a turbulent flow.

Rationale for a combined experimental and numerical approach

As a result of the complexity of the post-stenotic flow, it is not possible to obtain a simplified analytical solution of the Navier-Stokes equations. However, experimental and numerical approaches can be used to study such phenomena. The numerical methodology allows for a three-dimensional analysis of the fluid phenomena in time. The workflow of a typical computational simulation is described in this chapter, with a focus on the need of an experimental counterpart as ground-truth to prove the ability of the solver to reliably replicate the physics of the phenomenon. However, experiments are laborious, expensive and often not replicable. On the contrary, numerical methodologies are relatively cheaper and self-repeatable. Therefore, in this chapter we report the strategy used in the current work to combine the experimental and computational methodologies and perform a parametric study to allow an estimate of the ability of LDV to detect carotid stenosis.

PART II - FLOW INSTABILITIES: PREDICTORS OF CAROTID STENOSIS

High-frequency instabilities: a pragmatical in-silico study

This chapter is concerned with the development of the numerical methodology to obtain the flow field in a patient-specific carotid bifurcation with a 76

% stenosis in the internal carotid artery. The trade-off between accuracy and computational cost at constant and pulsatile flow rates is discussed by comparing the reference Direct Numerical Simulation (DNS) with several Large Eddy Simulations (LES), implemented with various sub-grid scale models. In this regard, the turbulent kinetic energy and the numerically-added viscosity are compared.

Laser Doppler vibrometry: a feasibility in-vitro study

The experimental methodology presented in this chapter aims to prove the ability of LDV to measure intra-arterial flow features and, consequently, the stenosis-induced flow instabilities. Specifically, it focuses on assessing the frequency-based sensitivity of the device to changes in physiologically varying flow rates.

Flow instabilities for stenosis detection: a combined approach

This chapter provides the evaluation of the possibility of using flow instabilities as marker for the presence of carotid stenosis. Firstly, we focused on the validation of the computational methodology, by comparing the intensity of flow instabilities recorded throughout the experimental study and the ones computed using the computational methodology on the same patient-specific geometry. As the two datasets were found to be in good agreement, we used the validated computational model to evaluate the impact of flow rate, flow split and stenosis severity on the intensity of downstream stenosis flow instabilities. Finally, we evaluated sensitivity, specificity, and accuracy of using the intensity of flow instabilities as a marker for stenosis detection.

Conclusions

The final chapter summarizes and discusses the main achievements of this PhD research. We have provided a proof of principle concerning the ability of a Laser Doppler Vibrometer device to infer the presence of carotid stenosis. The chapter concludes with suggestions for further investigation to overcome some limitations of this research as well as to the applicability of the dissertation topics to the clinical context.

SAMENVATTING

INLEIDING

De vroegtijdige opsporing van vernauwing van de halsslagader (carotisstenose) bij patiënten zonder symptomen is cruciaal voor het plannen van een behandeling ter preventie van beroerte, waarbij de hersenen zuurstofschade kunnen oplopen. Auscultatie is de huidige methodologie die wordt gebruikt in de eerstelijnszorg bij screening voor carotisstenose, maar deze methode is onnauwkeurig en kent veel beperkingen. Er is dan ook nood aan nieuwe en meer robuuste technieken die inzetbaar zijn in een eerstelijnszorg. Wij geloven dat een techniek gebaseerd op Laser Doppler-vibrometrie (LDV) potentieel bruikbaar is waarbij LDV de trillingen die ontstaan als gevolg van de stroming van bloed door een vernauwde slagader, zou kunnen detecteren op het huidoppervlak in de nek.

Een internationaal onderzoeksteam heeft, in het kader van een door H2020 gefinancierd project (Early stage CARdio Vascular Disease Detection with Integrated Silicon Photonics (CARDIS)) een prototype ontwikkeld van een compact multi-beam array LDV-systeem. Aan de basis van de ontwikkeling ligt een binnen IMEC ontworpen optische chip, waardoor de apparatuur kan worden geminiaturiseerd en goedkoper kan worden gebouwd dan huidige industriële systemen. Het doel van CARDIS is om het toestel bruikbaar te maken voor de klinische praktijk, met o.a. mogelijkheden tot uitvoeren van diagnostische/prognostische tests voor cardiovasculaire ziekte zoals het meten van arteriële stijfheid. Het doel van dit proefschrift betreft een uitbreiding van de toepassingen van het LDV systeem, waarbij we de haalbaarheid van LDV voor de detectie van carotisstenose wensen te evalueren. Het beoogde gebruik van een dergelijk apparaat is eerstelijns cardiovasculaire screening, waarbij personen met een verhoogd risico worden geïdentificeerd, zodat ze kunnen worden doorverwezen naar gespecialiseerde centra voor verdere opvolging met behulp van specifieke en gevestigde diagnostische technieken zoals echografie of MRI. De te detecteren trillingen op de huid ontstaan als gevolg van instabiliteiten in de stroming van het bloed doorheen de vernauwde halsslagader. We hebben ons in dit proefschrift dan ook specifiek gericht op (i) de ontwikkeling en validatie van een computationele methodologie om een beter begrip te krijgen van de intensiteit van stromingsinstabiliteiten als maat voor de voorspelling van de aanwezigheid van carotisstenose, en (ii) het inschatten van het potentieel om LDV te gebruiken voor de detectie van stromingsinstabiliteiten door meten van trillingen op huidniveau in de nek.

Dit proefschrift is opgebouwd uit drie grote onderdelen. Deel I biedt een algemene inleiding over carotisstenose en legt de principes uit achter de fysische verschijnselen die worden onderzocht. Dit deel geeft ook een overzicht van de gecombineerde experimentele en computationele aanpak in het onderzoek van complexe vloeistofdynamische problemen. Deel II omvat origineel onderzoek en beschrijft uitgebreid de realisaties van het doctoraatsonderzoek dat werd uitgevoerd in een samenwerking tussen de Universiteit Gent, Simula Research Laboratory en de Queen Mary University of London. Het laatste deel, tot slot, biedt nog een kort overzicht van de belangrijkste resultaten, met speciale aandacht voor de toepasbaarheid van de resultaten in de klinische praktijk. Hieronder vindt u een korte samenvatting van elk deel en hoofdstuk.

DEEL I - ACHTERGROND

Klinische basisgedachte

Dit hoofdstuk behandelt de basis van de anatomie en fysiologie van de menselijke arteriële boom, weliswaar beperkt tot de informatie die noodzakelijk wordt geacht om het werk beschreven in dit proefschrift te kunnen begrijpen en volgen. Vervolgens behandelen we de pathologie van de halsslagader - in het bijzonder carotisstenose – en schetsen we de mogelijk verwoestende gevolgen ervan als deze niet onmiddellijk wordt gedetecteerd en behandeld. Een overzicht van de mogelijke huidige diagnostische procedures voor de detectie van carotisstenose toont de behoefte aan nieuwe methodologieën.

Vloeistofdynamica in het cardiovasculaire systeem

De primaire focus van dit hoofdstuk is het toelichten van vloeistofdynamische verschijnselen die verband houden met carotisstenose. Geometrische factoren maken dat de halsslagadervertakking zeer vatbaar is voor de initiatie van verstoorde stromingsregimes, en dit ondanks het relatief laag Reynoldsgetal dat de stroming karakteriseert. Verstoorde stroming wordt gerelateerd aan het ontstaan van aneurysmata en vernauwing, die vervolgens op hun beurt de bloedstroom verder verstoren. Vloeistofdynamische verschijnselen kunnen mathematisch worden beschreven door de Navier-Stokes vergelijkingen. Deze vergelijkingen zijn complex, en analytische oplossingen zijn beperkt tot eenvoudige viskeuze laminaire problemen. Het stromingsprobleem dat wij dienen op te lossen is echter relatief complex, met het optreden van instabiliteit en turbulentie. Turbulentietheorieën, zoals die van Kolmogorov, hebben tot doel te beschrijven hoe de kinetische energie zich gedraagt op de verschillende schalen in een turbulente stroming.

Rationale voor een gecombineerde experimentele en numerieke benadering

Numerieke simulaties zijn uitermate geschikt voor een gedetailleerde driedimensionale analyse van de vloeistofverschijnselen in de tijd. De workflow van typische computersimulaties wordt in dit hoofdstuk beschreven. Numerieke simulaties leveren echter een benaderde oplossing op, en voor complexe problemen blijft er behoefte aan fysische experimenten om de accuraatheid van de oplossing en de numerieke code te aan te tonen, en te bewijzen dat de fysica van het bestudeerde fenomeen betrouwbaar kan worden gerepliceerd. Daarom wordt in dit hoofdstuk ook de strategie beschreven die in het huidige werk wordt gebruikt om de experimentele en computationele methodologieën te combineren, waarbij we een numerieke parametrische studie uitvoeren om een inschatting te kunnen maken van het potentieel van LDV om carotisstenose te detecteren.

Deel II - Stromingsinstabiliteit: voorspeller van halsslagaderstenose

Spectraalanalyse van stromingsinstabiliteiten: een pragmatische in-silico-studie

In dit hoofdstuk wordt de numerieke methodologie ontwikkeld om het stromingsveld te berekenen in een patiëntspecifiek model van de halsslagader met een 76 % stenose in de interne halsslagader. Het betreft een simulatie van transiënte/turbulente stroming onder constante en pulsatiele instroom, waarbij de afweging wordt gemaakt tussen nauwkeurigheid en rekenkost. De referentieberekening, Direct Numerical Simulation (DNS), wordt vergeleken met verschillende Large Eddy Simulations (LES), geïmplementeerd met verschillende sub-grid schaalmodellen. De turbulente kinetische energie en de numeriek toegevoegde viscositeit worden vergeleken.

Laser Doppler-vibrometrie: in-vitro haalbaarheidsonderzoek

Het doel van deze experimentele hydraulische studie, uitgevoerd in een fysisch model van de eerder vermelde patiëntspecifieke geometrie, is om praktisch aan te tonen dat LDV effectief in staat is om intra-arteriële stromingskenmerken te meten. LDV metingen worden uitgevoerd met het CARDIS prototype, simultaan met drukmetingen binnenin de halsslagader. Experimenten tonen aan dat stromingsinstabiliteiten aanleiding geven tot externe trillingen die met LDV kunnen worden gedetecteerd. Spectraalanalyse toont aan dat de intensiteit van gedetecteerde trillingen varieert met de aangelegde stroomsnelheden.

Stromingsinstabiliteiten voor stenosedetectie: een gecombineerde computationeel-experimentele aanpak

In dit hoofdstuk evalueren we, met gebruik van experimenten en het numerieke model, het gebruik van spectraalanalyse van stromingsinstabiliteiten als potentiële marker voor de aanwezigheid van carotisstenose. Een eerste stap was de validatie van de computationele methodologie, door de intensiteit van stroominstabiliteiten die tijdens het experimentele onderzoek zijn geregistreerd (met LDV) te vergelijken met waarden die zijn berekend met behulp van de computationele methodologie (druk- en snelheidsinformatie) op dezelfde patiëntspecifieke geometrie. Na verificatie dat beide datasets dezelfde spectrale informatie bevatten, hebben we het gevalideerde computermodel vervolgens gebruikt voor een ruimere parameterstudie om de impact van (i) stroomsnelheid; (ii) de verdeling van het debiet over de interne en externe halsslagader; en (iii) de ernst van stenose op de intensiteit van stromingsinstabiliteiten afwaarts van de stenose te evalueren. Ten slotte hebben we de gevoeligheid, specificiteit en nauwkeurigheid van het gebruik van de intensiteit van stroominstabiliteiten als een marker voor stenosedetectie geëvalueerd.

CONCLUSIES

In dit laatste hoofdstuk worden de belangrijkste resultaten van dit promotieonderzoek kort samengevat en besproken in een wat ruimere context. We besluiten dat het werk proof-of-principle aanlevert voor het gebruik van Laser Doppler Vibrometrie voor de detectie van halsslagaderstenose. De weg naar klinische toepassingen is echter nog lang en het hoofdstuk sluit dan ook af met suggesties voor verder onderzoek, strategieën om enkele beperkingen van het voorliggende onderzoek te overwinnen, en beschouwingen omtrent de toepasbaarheid van de methode in de klinische context.

INTRODUCTION

CONTEXT OF THE WORK

The World Health Organization estimated that 17.9 million people worldwide die each year due to cardiovascular diseases, ranking as the first cause of death globally. Among these, the majority (85 %) are due to myocardial infarction and stroke [1]. A stenosis in the internal carotid artery, resulting from the growth of an atherosclerotic plaque, is the most prominent cause of stroke [2], implying that a prompt detection of its onset could potentially prevent the occurrence of a stroke. However, asymptomatic carotid stenosis affects 7 % of women and over 12 % of men over 70 years of age [3], thus prompting the need for a specific detection pathway.

However, asymptomatic stenoses are not commonly diagnosed unless associated with other cardiovascular diseases (CVD) [4] such as coronary stenosis and hypertension, or risk factors such as diabetes [5], [6]. Thus, the possibility of assessing and stratifying the risk of a future stroke in asymptomatic patients with carotid stenosis is limited [3]. Furthermore, carotid ultrasound, which is routinely used for stenosis diagnosis in hospitals, is often too expensive and complex for use in first-line screening.

Auscultation is the current first-line screening methodology to detect asymptomatic carotid stenosis [7]–[9]. It is based on the audible bruit induced by the flow instabilities distal to the stenosis, whose presence is well established and proven by several studies [10]–[12]. However, carotid auscultation is well known to have limited value for the diagnosis of carotid artery stenosis, as its specificity is approximately 80 %, but the sensitivity is operator-dependent, varying from 50 % to 70 % [7], [13], [14]. Furthermore, auscultation was found to miss out on severe stenoses (> 75 %) [15]. Hence the urge for novel diagnostic methodologies.

THE CARDIS PROJECT AND LDV FOR STENOSIS DETECTION

Laser Doppler Vibrometry (LDV) has been shown over the years to be particularly suitable for detecting physiological signals from skin level displacement, for measurement of pulse wave velocity [16], breathing [17], or heart rate [18].

This PhD thesis was realized within the H2020 funded Early stage CARdio Vascular Disease Detection with Integrated Silicon Photonics (CARDIS) project. The aim of the CARDIS project was to develop a compact multi-beam array prototype LDV system [19] based on silicon photonics integrated LDV [20] with high spatio-temporal resolution (10 nm, 10 μs) [21], and suitable for use in a clinical setting.

Specifically, the CARDIS consortium aimed to investigate, demonstrate and validate the concept for the screening of arterial stiffness - by measuring pulse wave velocity [22], detection of stenosis and heart failure [23].

Hypothesizing that post stenotic flow instabilities impart energy to the arterial wall, giving rise to mechanical waves which propagate through the soft tissues up to the skin, there is a potential use of LDV for the detection of stenosis in superficial arteries, as a result of its high spatio-temporal resolution [21]. The intended use for such device would be first-line cardiovascular screening, identifying individuals at risk so that they can be referred to specialized centers for further follow-up using dedicated and established diagnostic techniques such as ultrasound.

RESEARCH GOALS

The purpose of the current dissertation was to provide a proof-of-concept on the use of LDV for carotid stenosis detection. In this respect, five main goals were defined:
Goal 1 - *Implementation of an efficient numerical model able to reliably replicate the flow field in a stenosed carotid artery*
Goal 2 - *Development of an experimental stenosed carotid artery model to obtain LDV traces*
Goal 3 - *Validation of the numerical model against the collected experimental measurements*
Goal 4 - *Conduction of a parametric study on the intensity of downstream-stenosis flow instabilities*
Goal 5 - *Obtaining a quantitative prediction of the feasibility of stenosis detection using LDV*
We achieved our goals as a result of the strong collaboration between the bioMMeda laboratory at Ghent University and the Simula Research Laboratory. Additionally, within the CARDIS project members, a special mention deserves the *Blizard Institute - Barts and The London* of Queen Mary University of London, for the impact of their collaboration.

DISSERTATION STRUCTURE OVERVIEW

This dissertation is divided in three major parts. Part I provides a background of the anatomy and physiology of the carotid arteries in chapter 1, an overview on physics of fluid dynamics in chapter 2, and an insight on the rationale for a combined experimental and computational approach for the current dissertation in chapter 3, respectively. In part II, the research goals achieved throughout the course of the PhD are reported. Specifically, chapter 4 is concerned with the best computational approach able to reliably replicate the downstream-stenosis turbulent-like flow, with a particular attention to the trade-off between accuracy and computational cost. Chapter 5 provides insights on the ability of the LDV to measure the flow instabilities. The experimental measurements are used for validation of the computational methodology, as reported in the first section of chapter 6, which later focuses on evaluating the best predictor for the presence of flow instabilities, and hence provides an estimate of the ability of an LDV device to detect early-stage carotid stenosis. Finally, the conclusions on the applicability of these research topics to the clinical practice are drawn in chapter 6.6.

LIST OF PUBLICATIONS

First-author peer-reviewed papers

- Mancini V., Bergersen A. W., Valen-Sendstad K., Segers P., Computed Post-Stenotic Flow Instabilities Correlate Phenotypically with Vibrations Measured Using Laser Doppler Vibrometry: Perspectives for a Promising In-Vivo Device for Early Detection of Moderate and Severe Carotid Stenosis, *Journal of Biomechanical Engineering, ASME collection*, vol. 142, no. 9, pp. 091007 1-13, 2020.
- Mancini V., Tommasin D., Li Y., Reeves J., Baets R., Greenwald S. and Segers P., Detecting Carotid Stenosis from Skin Vibrations using Laser Doppler Vibrometry – an *in-vitro* proof-of-concept, *PLoS ONE*, vol. 14, no. 6, pp. 1-17, 2019.
- Mancini V., Bergersen A. W., Vierendeels J., Segers P. and Valen-Sendstad K., High-Frequency Fluctuations in Post-stenotic Patient Specific Carotid Stenosis Fluid Dynamics: A Computational Fluid Dynamics Strategy Study, *Cardiovascular Engineering and Technology*, vol. 10, no. 2, pp. 277-298, 2019.
- Mancini V., Bergersen A. W., Segers P. and Valen-Sendstad K., Investigating the numerical parameter space for a stenosed patient-specific internal carotid artery model, *Progress in Applied CFD*, pp. 133-138, 2017.

Conference contributions

- Mancini V., Bergersen A. W., Valen-Sendstad K. and Segers P., Comparing Apples To Oranges; Measured Skin Vibrations Correlate Phenotypically With Computed Post-Stenotic Flow Instabilities. A Pragmatic But Robust Tool For Early Detection Of Carotid Stenoses?, oral presentation at the *16th International Symposium on Computer Methods in Biomechanics and Biomedical Engineering 2019*, Columbia University, New York, New York, USA.
- Mancini V., Bergersen A. W., Valen-Sendstad K. and Segers P., Intensity Of Stenosis-Induced Flow Instabilities Of The Internal Carotid Artery: A Computational Approach, poster presentation at the *Summer Biomechanics, Bioengineering and Biotransport Conference Proceedings 2019*, Seven Spring, Pennsylvania, USA.
- Mancini V., Bergersen A. W., Vierendeels J., Segers P. and Valen-Sendstad K., Can We Detect Carotid Artery Stenosis From Skin Vibrations : A Computational Investigation Of High-Frequent Flow Under Physiological Varying Flow Conditions, poster presentation at the *World Congress of Biomechanics 2018*, Dublin, Ireland.
- Mancini V., Tommasin D., Li Y., Baets R., Greenwald S. and Segers P., Detecting Carotid Stenosis From Skin Vibrations: Proof-Of-Principle From Hydraulic Bench Tests On A Compliant Stenotic Carotid Bifurcation Model, oral presentation at the *World Congress of Biomechanics 2018*, Dublin, Ireland.
- Mancini V., Tommasin D., Li Y., Baets R., Greemwald S. and Segers P., Can Laser Doppler Vibrometer Detect Carotid Stenosis From Skin Vibrations? Hydraulic Bench Tests On Patient-Specific Model, oral presentation at the *Association for Research into Arterial Structure and Physiology Conference 2018*, Guimaraes, Portugal.
- Mancini V., Bergersen A. W., Segers P. and Valen-Sendstad K., Prediction of Post Stenotic Flow Instabilities in a Patient Specific Common Carotid Artery Model, oral presentation at the *Summer Biomechanics, Bioengineering and Biotransport Conference 2017*, Tucson, Arizona, USA.
- Reeves J., Thacker S., Yousaf A., Birch M., Mancini V., Tommasin D., Marais L., Boutouyrie P., Segers P. and Greenwald S., Non-Contact Measurement of Carotid Artery Pulse Wave Velocity: Neck Phantom and Preliminary In-vivo Results, presented at the *Summer Biomechanics, Bioengineering and Biotransport Conference 2017*, Tucson, Arizona, USA.

- Mancini V., Bergersen A. W., Segers P. and Valen-Sendstad K., Can Large-Eddy Simulations Correctly Predict a Turbulent Stenotic Flow in a Patient-Specific Common Carotid Artery?, oral leading preentation at the *12th SINTEF International Conference on CFD in Oil & Gas, Metallurgical and Process Industries 2017*, Trondheim, Norway.

- Mancini V., Vierendeels J., Tommasin D., Shaw S., Swillens A., Yousaf A., Greenwald S. and Segers P., An Explorative CFD Study On Stenosis-Induced Flow Instabilities In The Carotid Artery, poster presentation at the *Summer Biomechanics, Bioengineering and Biotransport Conference 2016*, National Harbor, Maryland, USA.

- Mancini V., Vierendeels J., Tommasin D., Greenwald S. and Segers P., An Explorative Computational Fluid Dynamics Study On Stenosis-Induced Flow Instabilities In The Carotid Artery, poster presentation at the *National Day of Biomedical Engineering Conference 2016*, Brussels, Belgium.

I

Background

Chapters

1 **Clinical rationale** 3

2 **Fluid dynamics in the cardiovascular system** 17

3 **Rationale for a numerical approach** 33

CHAPTER 1

CLINICAL RATIONALE

This chapter provides an overview on the clinical rationale leading to the research topic of this dissertation. The first section provides a general introduction on the anatomy and physiology of our cardiovascular system, with a focus on the carotid arteries in the second section. The third section is concerned with carotid stenosis, and related current treatments and diagnostic procedures. An overview on a novel diagnostic procedure is provided in the final section.

1.1 CARDIOVASCULAR SYSTEM

The cardiovascular system (CVS) consists of the heart and of the blood vessels through which the blood circulates. The blood is a particulated fluid, as it is composed of a suspension of particles (erythrocytes, leukocytes and thrombocytes - 45 %) in a liquid part (plasma, 55 %). It accounts for approximately 8 % of body weight, with an average volume of 4-6 liters [24]. One of the functions of blood and the CVS is to distribute vital substances to the tissues. The heart is a muscular organ in the chest cavity, and can be functionally divided in a right and a left side, as they pump the blood into the pulmonary and the systemic circulations, respectively. Each side is anatomically divided in an atrium and a ventricle.

The pulmonary circulation oxygenates the blood returning from the systemic circulation. It starts in the right ventricle, which pumps the de-oxygenated blood towards the lungs via the pulmonary arteries, and ends in the left atrium, which collects the oxygenated blood via pulmonary veins. The systemic circulation allows the blood rich of oxygen and nutrients to reach each cell while carrying away metabolic wastes such as carbon dioxide. A schematic representation of the systemic circulation is provided in Figure 1.1. The systemic circulation is driven by the contraction of the left ventricle, which pumps the oxygenated blood in the aorta. Each segment of the aorta branches into smaller arteries until reaching the capillary beds, where the exchange of oxygen and nutrients with metabolic wastes occurs. The venous blood is then collected by gradually larger veins and returns to the right atrium via the inferior and superior vena cava [25].

Arteries and veins share the function of carrying blood between the heart and the cells. Blood flows in the lumen of the vessels, whose wall is usually constituted by three layers [26]:

- **tunica intima** is the innermost layer. It is constituted largely of endothelial cells and a variable amount of subendothelial connective tissue, better known as *lamina propria*, depending on the vessel size and function. The endothelial cells are arranged closely together, hence preventing the discontinuity in the vessel's lumen and minimizing blood's friction. Their thickness varies from 0.2 to 3 µm, and they are generally elongated in the direction of the blood flow. The tunica intima regulates transmural transport and converts blood flow wall shear stress to biomechanical signals.

- **tunica media** is the intermediate layer. It is composed mainly of concentric layers of circumferentially or helically arranged smooth muscles controlled by sympathetic nerves, and therefore regulates vasoconstriction (decrease of lumen diameter) and vasodilation (increase of lumen diameter). Collagen and elastin fibers are also present.

- **tunica externa** is the outermost layer. It is composed mainly of collagen and elastin fibers, as it integrates the vessel to its surrounding structures. This layer provides the vessels of elastic and compliant properties.

The three layers are separated from each other by elastic lamellae (*internal* between tunica intima and tunica media, and *external* between tunica media and tunica externa).

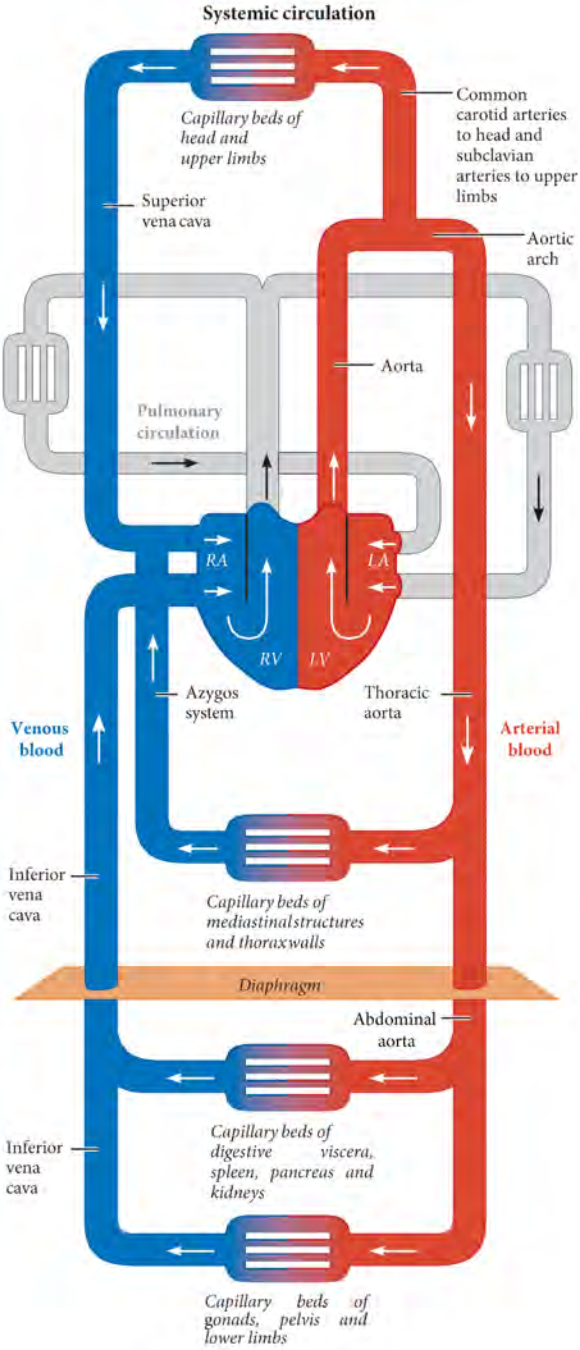

Figure 1.1: Schematic representation of the systemic circulation. The pulmonary circulation is shown in gray for comparison. Adapted from [24].

Overall, veins are typically thinner than arteries. The usual diameter and thickness of larger arteries is 1 cm and 1 mm, respectively, while it is 0.5 cm and 0.5 mm for larger veins [24]. As shown in Figure 1.2, the wall structure of arteries and veins is different [27] as a result of the different pressure regimes that occur in the two types of vessel: elastic arteries experience a pressure from 80 to 120 mmHg because the blood is being pumped directly in the arteries by the heart towards the rest of the body; veins, on the other hand, experience a lower pressure (1 to 15 mmHg), as a result of the flow **resi**stance of the microvasculature [28]. The tunica media is therefore typically thicker in arteries than in veins [29]. Furthermore, systemic veins and venules carry a large portion of the blood volume (60 %) and are therefore referred to as capacitance vessels. The tunica externa in veins is typically thicker than the one in arteries [29].

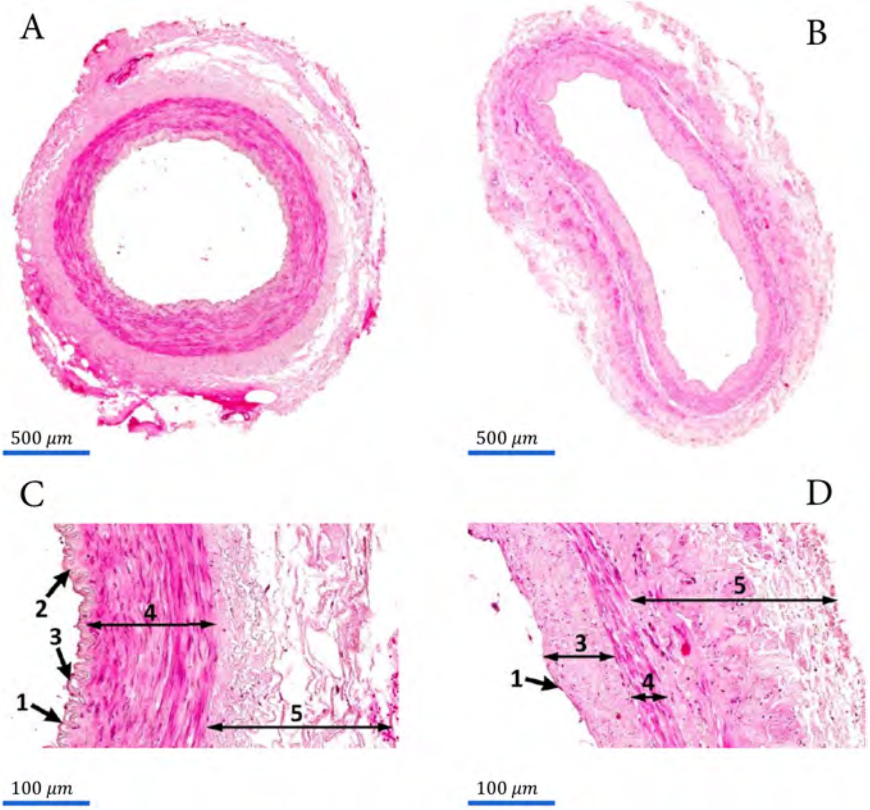

Figure 1.2: The histology of internal thoracic artery (A, C) and saphenous vein (B,D) allow to notice their structural differences. Arrows: 1—endothelium, 2—internal elastic lamina, 3—tunica intima, 4—tunica media, and 5—tunica externa. Adapted from [27] .

The different structure of an elastic and a muscular artery is noticeable in Figure 1.3. Vessels' size and composition depend on their location in the CVS. The large central arteries have more elastin and less smooth muscle cells than the more peripheral arteries [30]. Therefore, the central arteries are called *elastic*, while the more peripheral ones are called *muscular*. For instance, the aorta, the major artery of our body, is also the most elastic one, as it contains more elastin than any other vessel. Therefore, its tunica media is relatively larger than other arteries, resulting in a diameter between 1 and 2.5 cm.

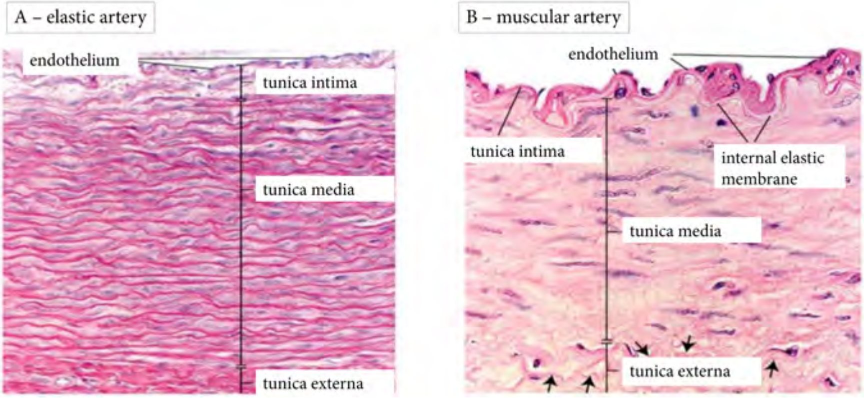

Figure 1.3: Histological images of (A) a large elastic artery and (B) a muscular artery. The media of the elastic artery consists of concentrically organized musculo-elastic complexes, while the medial organization of the muscular artery in musculo-elastic complexes has entirely disappeared. Adapted from [30].

1.2 CAROTID ARTERIES

At rest, approximately 13 % of the blood is normally carried to the brain in adults [24]. The carotid arteries are the main vessels supplying blood to the brain. The left common carotid artery (CCA) branches directly from the aortic arch, while both the right CCA and the right vertebral artery branch off from the right subclavian artery, as shown in Figure 1.4. The CCA branches into the external (ECA) and internal (ICA) carotid arteries. The ECA supplies most of face muscles and the tongue. The ICA, throughout its branches, supplies the orbits and more than 80 % of the cerebral blood. The remaining volume is carried mainly by the vertebral arteries, which, furthermore, are connected to the ICAs via the Circle of Willis, providing redundancy in the supply of cerebral blood [31].

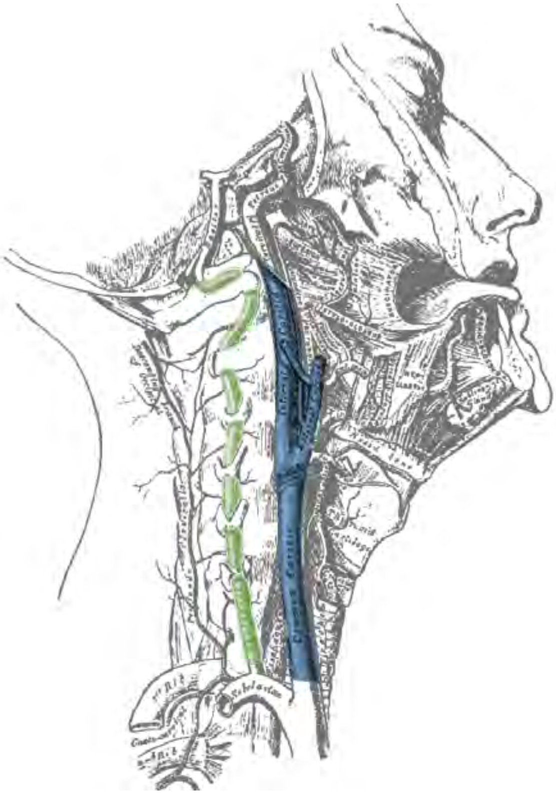

Figure 1.4: Representation of the right view of neck's arteries. The vertebral and carotid arteries are shown in green and blue, respectively. Adapted from [32].

Typical flow waveforms of the blood flowing through CCAs, ICAs and ECAs of older adults (60-76 years old, N=94) [33] are reported in Figure 1.5, where it is possible to notice that the pulsatility of the CCA is higher than the pulsatility of ICA. The damping is a consequence of a combination of increased destinsibility and increased resistance of the bifurcated arteries relatively to the upstream one.

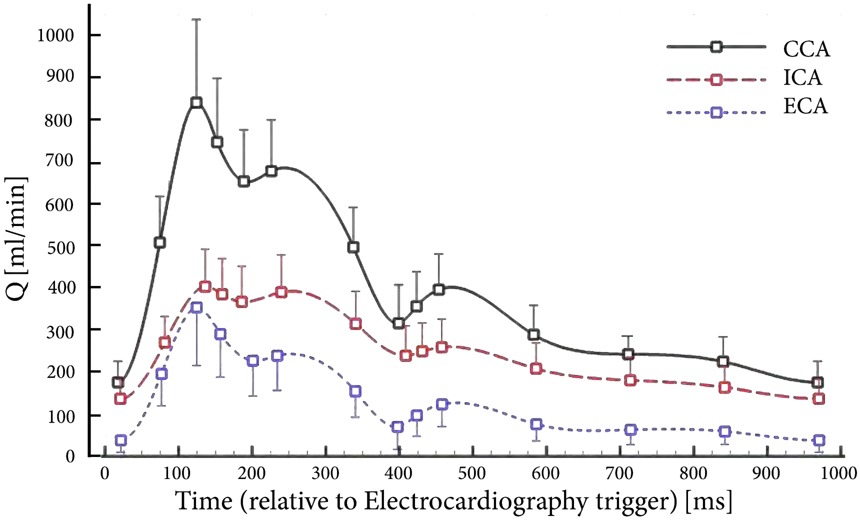

Figure 1.5: Representation of the volumetric flow rate of CCA, ICA and ECA averaged over 94 older adults. The time is relative to the trigger of the electrocardiogram. Adapted from [33].

As the percentage increase in area at a given pressure is lower in a larger artery, the CCA have less distensibility CD than the ICA, but its compliance C will be greater because of the larger absolute volume increase [34], [35] (see equations 1.1 and 1.2).

$$CD = \frac{\Delta V \; V_0}{\Delta P} \tag{1.1}$$

$$C = \frac{\Delta V}{\Delta P} \tag{1.2}$$

The vascular resistance R, based on Poiseuille's law (more thoroughly described in section 2.18), is defined in equation 1.3. It shows that the diameter D and the length of the vessel L, together with the dynamic viscosity of the blood μ and the flow rate Q at which it flows in the vessel lumen, have an impact on the vessel resistance. According to Blum [36], due to the decrease in diameter with each split, the vessel resistance at the n-th generation increases exponentially, as defined in equation 1.4. The total resistance of an arterial tract can be defined as the sum of the resistance of each arterial segment, see equation 1.5. Please note that Blum's theory of the build-up resistance does not take into account the impact of the presence of bifurcations and other fluid mechanical factors on the vascular resistance.

$$R = \frac{128\mu L}{\pi D^4} \tag{1.3}$$

$$R_{gen-n} = \frac{2.52^n}{2^{n-1}} \cdot R_{parent} \tag{1.4}$$

$$R_{tract} = R_{gen-1} + R_{gen-2} + \ldots + R_{gen-n} \tag{1.5}$$

Additionally, the ICA is of greater relevance for the presence of the carotid sinus, which is one of the sites in the CVS hosting baroceptors. The baroceptors are essential for homeostasis regulation, i.e. the maintenance of arterial blood pressure *BP* in the normal range: if the *BP* rises above the normal range (i.e. system imbalance) [37], the baroceptors are stimulated and hence send impulses to the cerebral centers controlling the vasomotor activities, inducing a decrease in the rate of vasomotor impulses. These stimuli result in vasodilatation (increase of the lumen diameter D), which leads to a decrease in vascular resistance R and, therefore, lowers *BP* to the normal range, based on the equation 1.6. Equation 1.6 is better known as Poiseuille's law [38], and it is more thoroughly described in section 2.1 (specifically, in equation 2.18). The same pathway applies in the case of lower BP, by enforcing vasoconstriction. Therefore, the presence of unstable or fluctuating fluid dynamics in ICA impact baroceptors and hence the entire CVS.

$$BP = R \cdot Q \tag{1.6}$$

1.3 STENOSIS

The abnormal constriction of the vessel lumen due to the growth of an atherosclerotic plaque is better known as stenosis, and it can occur at a variety of locations in the CVS such as systemic, pulmonary, and cerebral arteries [39]. As more thoroughly justified in section 2.3, among the arteries, the carotid arteries are particularly prone to the development of a stenosis.

As represented in Figure 1.6, a stenosis can be found in several morphologies in the human body, as found by [40] by performing angiography on 110 patients, depending on the extension of the atherosclerotic plaque. The composition of the plaque can also largely vary, as represented in Figure 1.7.

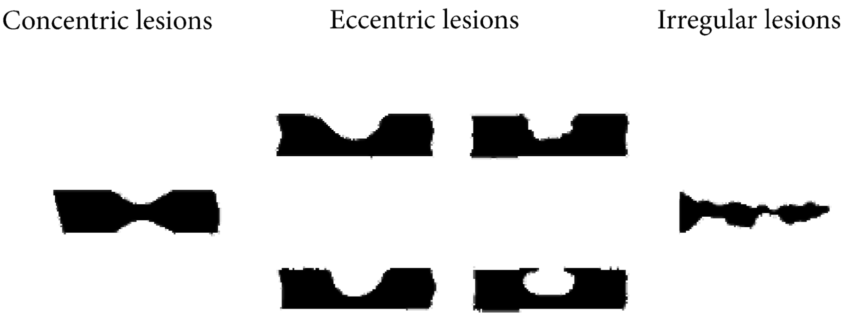

Figure 1.6: Diagram of stenotic artery angiographic patterns. Adapted from [41].

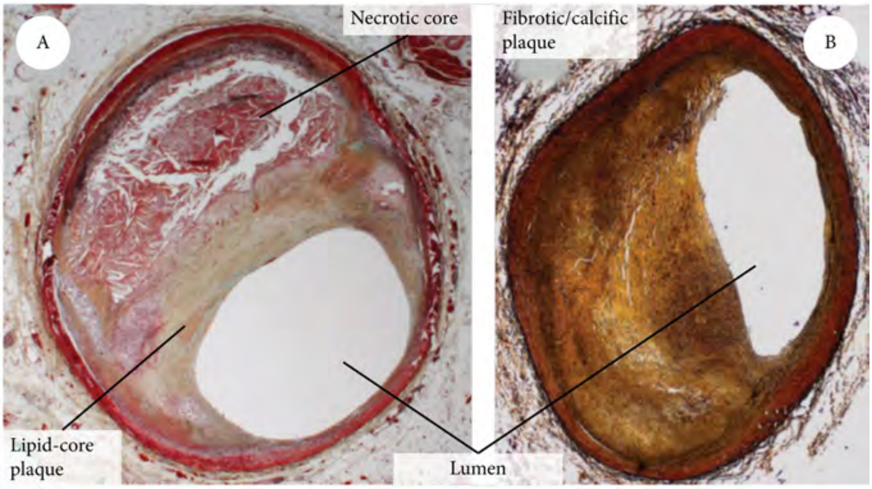

Figure 1.7: Intracoronary near-infrared spectroscopy histology sections of a lipid core (A) and a fibrotic-calficic core (B) atherosclerotic plaques obstructing an artery, leading to stenosis. Adapted from [42].

The severity of a stenosis, i.e. the percentage of obstruction (see equation 1.7 for the North American Symptomatic Carotid Endarterectomy Trial method, where $A = \frac{\pi D^2}{4}$ is the cross-sectional area), can vary from moderate to extremely severe, as depicted in Figure 1.8. Furthermore, the plaque can extend over a large portion of the artery [41], as reported in Figure 1.9.

$$severity = \frac{A_{downstream} - A_{stenosis}}{A_{downstream}} \cdot 100 \tag{1.7}$$

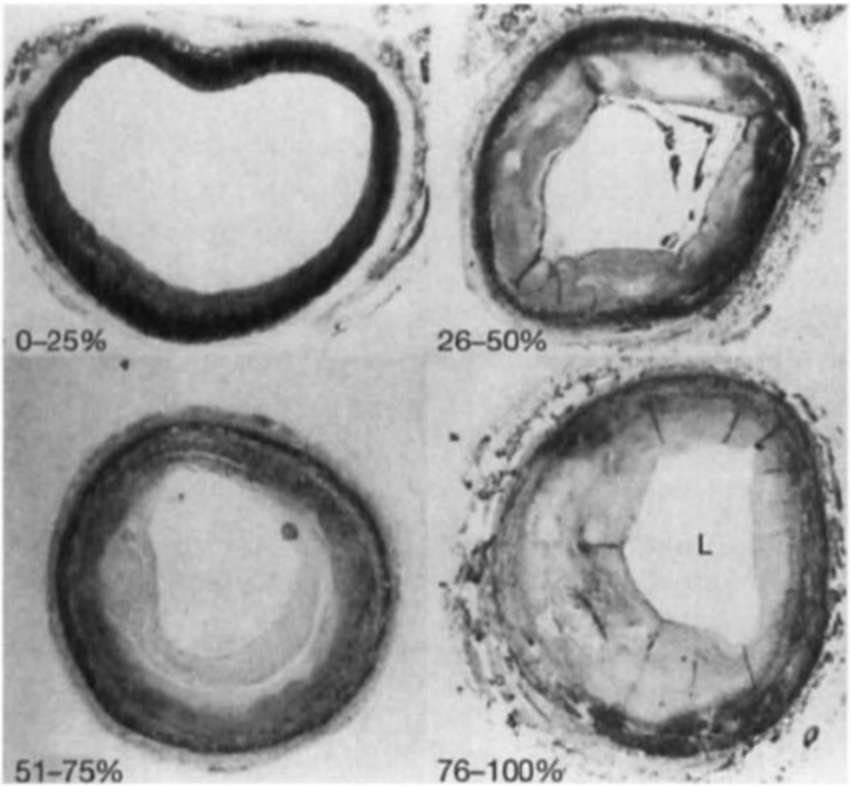

Figure 1.8: Four grades of luminal cross-sectional area reduction, L = lumen. Sections of epicardial coronary arteries adapted from [43].

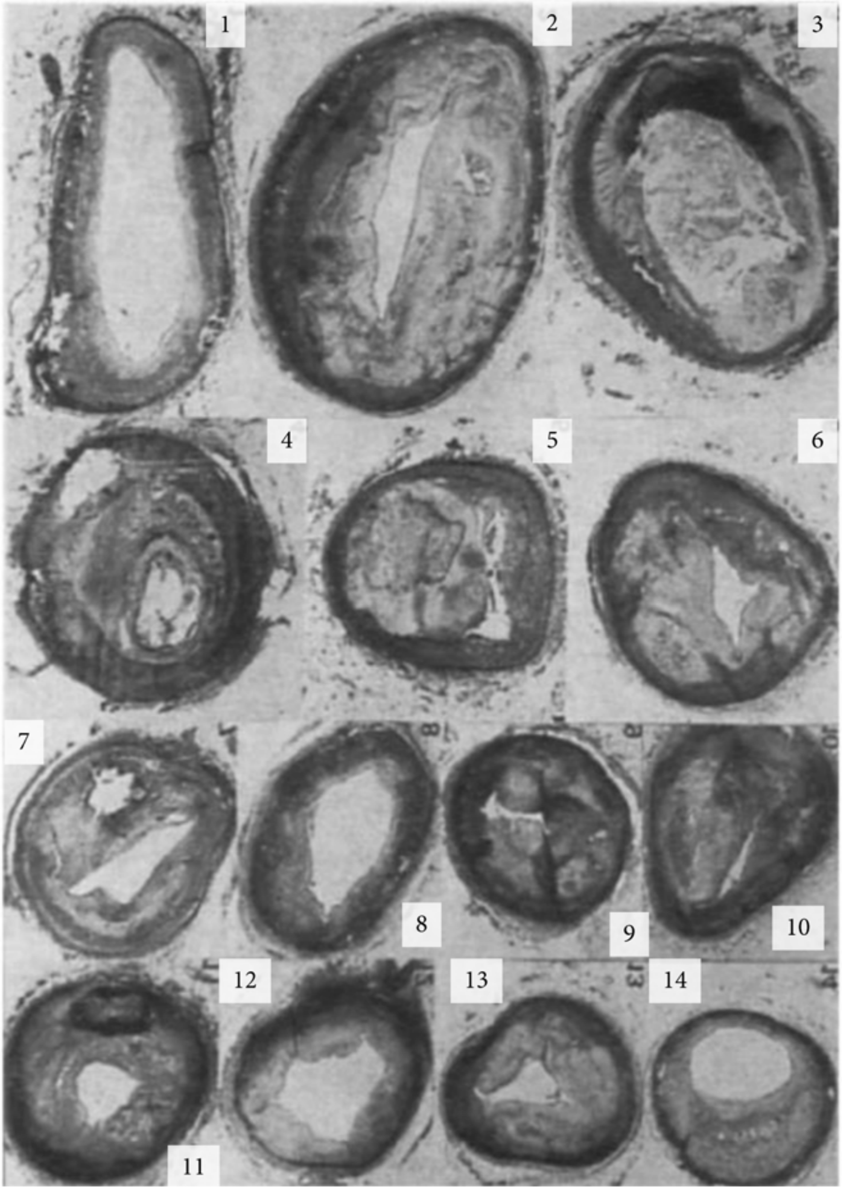

Figure 1.9: Composite of 5 mm coronary artery cross sections from ostium (1) to distal-most portion (14), with marked variation in luminal (L) shape, size, and course. Adapted from [41].

1.4 Carotid stenosis and stroke: current treatments and diagnostic procedures

The presence of a carotid stenosis could lead to a significant reduction or blockage of the blood flow towards the brain, causing ischemic stroke [2]. Stroke represents the third cause of death worldwide, as it accounted for more than three million deaths in 2017 alone [44]. If not fatal, stroke is a debilitating disease, as it can lead to hemiparesis (one-side facial paralysis) or hemiplegia (one-side body paralysis): the economical burden and social implications of stroke are dramatic. Moreover, recurrent stroke is frequent, as about 25 % of people who recover from their first stroke will have another stroke within 5 years [45]. Carotid artery stenosis alone is responsible for 6 out of 10 large-vessel atherothrombotic strokes [46].

As a result of several randomized control trials [7], the Society for Vascular Surgery has long considered carotid endarterectomy the best surgical treatment for carotid stenoses [47]. It consists in making an incision along the front of the neck, opening the carotid artery and removing the plaques that are clogging the artery, as depicted in Figure 1.10a. Carotid angioplasty and stenting surgery has emerged in the last decade as a less invasive alternative to carotid endarterectomy. As shown in Figure 1.10b, it consists in inserting a catheter in the stenosed artery and forcing the compression of the plaque towards the arterial wall using a balloon or a permanent stent. The advantage of carotid angioplasty and stenting surgery is due to fewer cardiovascular complications, milder sedation and absence of neck incisions. Medical therapy, such as combined antiplatelets drug therapy, the use of statin medication and anti-hypertensive agents as an aggressive correction of risk factors [7], is also a possible alternative or cooperator.

The elective therapy depends on the differentiation between symptomatic and asymptomatic patients, on the stenosis severity, and on other factors (i.e. age and sex) [47]. Specifically, carotid endarterectomy is recommended for symptomatic patients with > 60 % stenosis [48], but it has no benefits for patients with lower degree of stenosis if 30-60 % and it even increases the risk of stroke, both operative and ischemic, for patients with less than 30 % stenosis [49]. Carotid endarterectomy was found to provide fewer benefits on high-grade asymptomatic patients (for whom the risk of cardiac ischemia and vascular death is as high as 9.9 % annually [50]), with only a marginal benefit from revascularization [7] and a 1 % risk reduction of stroke per annum in two years [51]. However, there is disagreement concerning the underlying randomized control trials on carotid angioplasty and stenting surgery for asymptomatic patients, which has limited its use. The decision on whether to implement invasive treatment in patients with asymptomatic carotid artery stenosis is a difficult one [7].

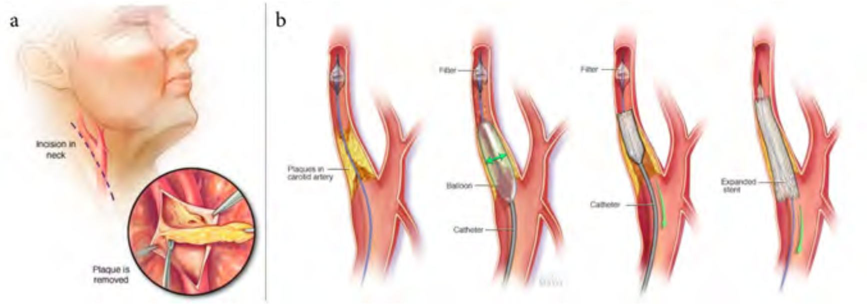

Figure 1.10: Endarterectomy (a) and stenting (b) are the current procedures for carotid stenosis. Adapted from [52].

The yield of prophylactic invasive treatments, on the other hand, would improve with the identification of asymptomatic patients at high risk of stroke, e.g. with a high-grade or a progressive stenosis [7]. Furthermore, early detection could decrease mortality [53]. The two main current diagnostic procedures for carotid stenosis are carotid auscultation and ultrasound. Auscultation is based on the presence of the carotid bruit, and relies on the experience of the practitioner to discern it. This technique therefore suffers from a lack of specificity and sensitivity, but it is still currently used by general practitioners because of its non-invasivity and inexpensiveness [54]. Ultrasound, which is routinely used for stenosis diagnosis in hospitals, is complex for use in first-line screening [55].

CHAPTER 2

FLUID DYNAMICS IN THE CARDIOVASCULAR SYSTEM

The study of fluid dynamics is concerned on how fluids behave when in motion. The primary focus of this chapter is to provide an overview of the fluid dynamics phenomena related to carotid stenosis. The relevant fluid dynamical equations are reported and then applied to the specific research topic of this dissertation in the first section 2.1. An overview of fluid dynamics and the flow regimes is provided in the second section 2.2, followed by their application to the cardiovascular system in the third section 2.3 and, specifically, to the carotid arteries in the fourth section 2.4. Finally, the existence and smoothness problem of the Navier-Stokes equations for turbulent fluids and the Kolmogorov theory of turbulence are reported in the sections 2.5 and 2.6, respectively.

2.1 NAVIER-STOKES EQUATIONS

To better understand the changes that a flow undergoes when entering and exiting a stenosis, it is worth introducing the incompressible Navier-Stokes equations. They consist of a system of two equations expressing the conservation of mass, i.e. the continuity equation (2.1), and the momentum equations (2.2), respectively. Both equations are partial differential equations (PDEs), as they involves partial derivatives of multiple unknown independent variables. D is the material derivative, ρ is the fluid density, $\overrightarrow{v}$ is the velocity vector, p is the pressure, $\overrightarrow{\tau}$ is the viscous stress tensor and $\overrightarrow{g}$ is the gravity acceleration [56].

$$\nabla \cdot \overrightarrow{v} = 0 \tag{2.1}$$

$$\rho \frac{D\overrightarrow{v}}{Dt} = -\nabla p + \nabla \cdot \overrightarrow{\tau} + \rho \overrightarrow{g} \tag{2.2}$$

Due to the complexity of the cardiovascular system, the arteries are often modeled as pipes in order to gain a first order insight on the fluid dynamics of the CVS by taking advantage of the thorough studies that have been made on pipes. Considering that we are interested in the motion of fluid in a simil-cylindrical pipe, both equations are going to be written in cylindrical coordinates where r, θ and z are the radial, angular and axial coordinates, respectively. Therefore, v_r, v_θ and v_z are the radial, angular and axial velocity components. Please refer to Figure 2.1 for a schematic representation of the problem and its coordinate system. The equations, which apply for a Newtonian fluid, are expressed by using the Eulerian formulation, i.e. the fluid motion is observed from an external view point and, therefore, the quantities are examined in function of time and position in a fixed reference frame.

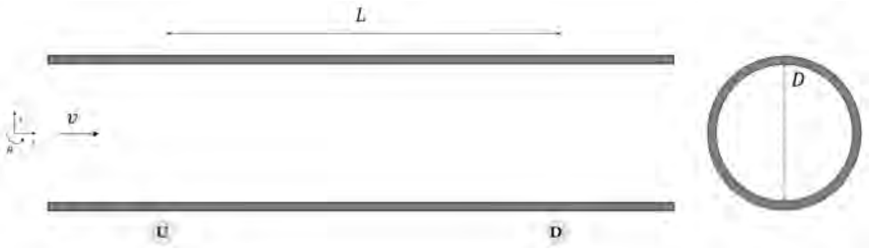

Figure 2.1: Schematic representation of a pipe with diameter D and length L, in which a fluid with kinematic viscosity ν is entering at velocity v. U: upstream, D: downstream. Coordinate system on the left side.

2.1.1 Continuity equation

The continuity equation for an incompressible fluid refers to the law that the mass of the fluid does not change. It is defined as in equation 2.3.

$$\frac{1}{r}\frac{\partial(r\, v_r)}{\partial r} + \frac{1}{r}\frac{\partial v_\theta}{\partial \theta} + \frac{\partial v_z}{\partial z} = 0 \tag{2.3}$$

2.1.2 Momentum equation

The momentum equation describes the momentum of a viscous fluid, which is a three-dimensional problem and, therefore, results in one equation for each velocity component. In cylindrical coordinates, they can be written as in 2.4, 2.5 and 2.6, where ρ and μ are the fluid properties, p is the pressure (scalar) and $\overrightarrow{g} = (g_r, g_\theta, g_z)$ is the gravitational acceleration.

$$\begin{aligned} r : \rho[\frac{\partial v_r}{\partial t} + v_r\frac{\partial v_r}{\partial r} + \frac{v_\theta}{r}\frac{\partial v_r}{\partial \theta} - \frac{v_\theta^2}{r} + v_z\frac{\partial v_r}{\partial z}] = -\frac{\partial p}{\partial r} + \rho g_r + \\ +\mu[\frac{1}{r}\frac{\partial}{\partial r}(r\frac{\partial v_r}{\partial r}) - \frac{v_r}{r^2} + \frac{1}{r^2}\frac{\partial^2 v_r}{\partial \theta^2} + \frac{\partial^2 v_r}{\partial z^2} - \frac{2}{r^2}\frac{\partial v_\theta}{\partial \theta}] \end{aligned} \tag{2.4}$$

$$\begin{aligned} \theta : \rho[\frac{\partial v_\theta}{\partial t} + v_r\frac{\partial v_\theta}{\partial r} + \frac{v_\theta}{r}\frac{\partial v_\theta}{\partial \theta} + v_z\frac{\partial v_\theta}{\partial z} + \frac{v_r v_\theta}{r}] = -\frac{1}{r}\frac{\partial p}{\partial \theta} + \rho g_\theta + \\ +\mu[\frac{1}{r}\frac{\partial}{\partial r}(r\frac{\partial v_\theta}{\partial r}) - \frac{v_\theta}{r^2} + \frac{1}{r^2}\frac{\partial^2 v_\theta}{\partial \theta^2} + \frac{2}{r^2}\frac{\partial v_r}{\partial \theta} + \frac{\partial^2 v_\theta}{\partial z^2}] \end{aligned} \tag{2.5}$$

$$\begin{aligned} z : \rho[\frac{\partial v_z}{\partial t} + v_r\frac{\partial v_z}{\partial r} + \frac{v_\theta}{r}\frac{\partial v_z}{\partial \theta} + v_z\frac{\partial v_z}{\partial z}] = -\frac{\partial p}{\partial z} + \rho g_z + \\ +\mu[\frac{1}{r}\frac{\partial}{\partial r}(r \cdot \frac{\partial v_z}{\partial r}) + \frac{1}{r^2}\frac{\partial^2 v_z}{\partial \theta^2} + \frac{\partial^2 v_z}{\partial z^2}] \end{aligned} \tag{2.6}$$

The terms on the left hand side, divided by ρ, refer to the accelerations of the fluid, specifically the local acceleration (time variant term) and the convective acceleration. The terms on the right hand side refer, in order of appearance, to the pressure gradient term, to the body force term, and to the viscous terms (identified by the dynamic viscosity μ).

2.1.3 Simplifications leading to Poiseulle's law

To solve the Navier-Stokes equations is extremely challenging. By reasoning on the physics of the problem of interest, it is possible to apply several assumptions to simplify the equations. Specifically in the context of a cylindrical pipe flow, both the continuity and the momentum equations of a laminar flow can be simplified when taking into account the following physically reliable assumptions:

- steady flow: the velocity of the fluid in any point does not change over time, hence all time derivatives are null $\Rightarrow \frac{\partial}{\partial t} = 0$;

- horizontal pipe: gravity does not play a role, hence all gravity terms are null ⇒ $\overrightarrow{g} = 0$;
- only longitudinal forces act on the fluid, i.e.:
  - no radial forces act on the fluid, hence all radial velocity terms and its derivatives are null ⇒ $v_r = 0$
  - no rotational forces act on the fluid, hence all rotational velocity terms and its derivatives are null ⇒ $v_\theta = 0$
- the cylindrical geometry is symmetric with respect to θ, hence v_z does not depend on $\theta \Rightarrow \frac{\partial v_z}{\partial \theta} = 0$

By applying these assumptions to the previous equations, we obtain the following:

$$2.3 \Rightarrow \frac{\partial v_z}{\partial z} = 0 \tag{2.7}$$

$$2.4 \Rightarrow 0 = -\frac{\partial p}{\partial r} \tag{2.8}$$

$$2.5 \Rightarrow 0 = -\frac{\partial p}{\partial \theta} \tag{2.9}$$

$$2.6 \ \& \ 2.7 \Rightarrow 0 = -\frac{\partial p}{\partial z} + \mu \frac{1}{r} \frac{\partial}{\partial r}\left(r \cdot \frac{\partial v_z}{\partial r}\right) \tag{2.10}$$

Equation 2.10 is the simplified form of the longitudinal component of the momentum equation. In order to solve it, it can be multiplied by $\frac{r}{\mu}$ and integrated by ∂r, obtaining equation 2.11, which can, in turn, be multiplied by $\frac{1}{r}$ and integrated once more by ∂r, obtaining 2.12 and two integration constants, C_1 and C_2.

$$\frac{r^2}{2\mu} \frac{\partial p}{\partial z} + C_1 = r \cdot \frac{\partial v_z}{\partial r} \tag{2.11}$$

$$\frac{r^2}{4\mu} \frac{\partial p}{\partial z} + C_1 \cdot \ln(r) + C_2 = v_z \tag{2.12}$$

In order to obtain the value of the integration constants of equation 2.12, we need to introduce the two following boundary conditions:

- the fluid velocity is finite at the centerline ($r = 0$) ⇒ $C_1 = 0$

- no slip condition: the fluid velocity is null at the pipe walls ($r = D/2$) $\Rightarrow C_2 = -\frac{D^2}{16\mu}\frac{\partial p}{\partial z}$

Furthermore, the pressure term refers to the pressure gradient along the cylindrical pipe. If we assume the pipe in Figure 2.1 to have arbitrary length L between point U for *upstream* and point D for *downstream*, then the pressure at the entrance of the pipe ($z = U$) is p_U and the pressure at the end ($z = D$) is p_D. Therefore, the pressure term can be written as in equation 2.13, where $p_U > p_D$.

$$\frac{\partial p}{\partial z} = \frac{p_U - p_D}{-L} = -\frac{\Delta p}{L} \tag{2.13}$$

By replacing the integration constants and the pressure term in equation 2.12, it is possible to obtain equation 2.14. It represents the physics of the fluid dynamical problem: it shows that the velocity of a fluid in a pipe depends on the pressure gradient along it, as the fluid flows left to right with an intensity proportional to $p_U - p_D$. Furthermore, it describes the parabolic profile of the longitudinal velocity through a pipe, which is null at the wall (see equation 2.15) and reaches its maximum at the center (see equation 2.16).

$$v_z = \frac{4r^2 - D^2}{16\mu}\frac{\Delta p}{L} \tag{2.14}$$

$$r = \frac{D}{2} : v_z = 0 \tag{2.15}$$

$$r = 0 : v_z = \frac{D^2}{16\mu}\frac{\Delta p}{L} \tag{2.16}$$

It is worth noticing that it is possible to rewrite equation 2.16 as function of volumetric flow rate Q (see equation 2.17), hence obtaining Poiseulle's law. It was previously presented in equation 1.6, and it is here re-presented as in equation 2.18 to highlight the relationship between the pressure drop and the fourth power of the diameter.

$$Q = v \cdot A \tag{2.17}$$

$$\Delta p = \frac{128\mu L}{\pi D^4} Q \tag{2.18}$$

2.2 FLOW REGIMES

A fluid in a pipe is commonly classified in three main regimes:

- Laminar flow: the fluid flows in infinitesimal parallel layers with no disruption between them;
- Unstable or transitional flow: the flow is not fully laminar nor fully turbulent;
- Turbulent flow: a turbulent flow can be defined by its properties [57]:
  - Diffusive - rapid mixing and spread of velocity fluctuations through the surrounding fluid;
  - Rotational and three-dimensional - high levels of fluctuating vorticity;
  - Irregular - chaotic changes, streamlines crossing
  - Dissipative - the turbulent kinetic energy decays rapidly into internal energy of the fluid as a result of the viscous forces.

2.2.1 Pipe flow

Historically, the existence of two distinct types of flows in a pipe was first observed in 1839 by Hagen [58]. However, the distinction between turbulent and laminar regimes was studied in 1883 by Osborne Reynolds [59], who also identified a dimensionless number able to discriminate between flow regimes, the Reynolds number (Re), defined as in equation 2.19. It represents the ratio between inertial and viscous forces, and it implies that the flow regime of a fluid depends on the combination of material properties of the fluid itself (kinematic viscosity ν, defined as the ratio between dynamic viscosity μ and density ρ), on its velocity v, and on the diameter of the pipe D. For instance, the flow of fluid with kinematic viscosity ν in a pipe of diameter D_1 can transition from laminar to transitional and eventually to turbulent by an increase of velocity $v_2 > v_1$ such that the Reynolds number varies across the thresholds reported in Table 2.1.

$$Re = \frac{v \cdot D}{\nu} \tag{2.19}$$

This is exemplified by panels a and b of Figure 2.2. An increase in cross-sectional area (hence $D_2 > D_1$, as depicted in Figure 2.2c) can lead to unstable flow despite the velocity v_1 is the same as in a pipe without restrictions (panel a). The combination of increased velocity and increased pipe diameter as in

Laminar Regime	**Transitional Regime**	**Turbulent Regime**
$Re < 2300$	$2300 < Re < 4000$	$Re > 4000$

Table 2.1: Commonly accepted thresholds for relationship between Reynolds number Re and flow regimes.

Figure 2.2d would lead to a further increase of Reynolds number and hence, possibly, to turbulence. Please note that the velocity profile for laminar flow (Figure 2.2a) is parabolic as previously reported in equation 2.14. It is implied that the flow at z_U in Figure 2.2 has already overcome the hydrodynamic entrance length and is therefore fully developed.

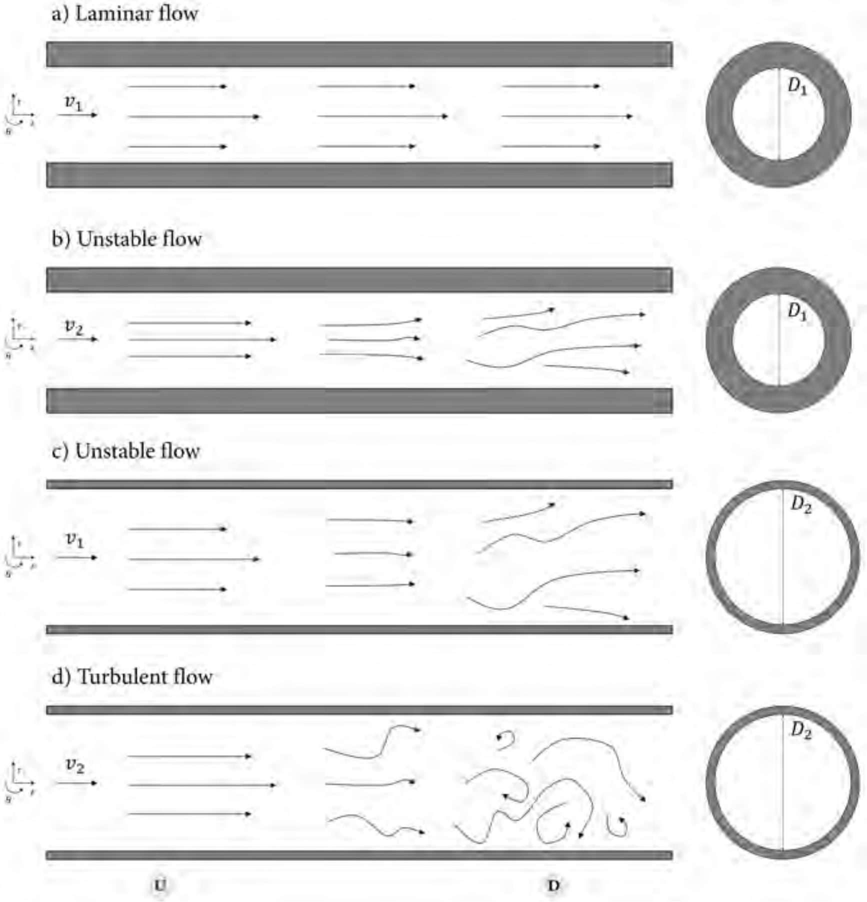

Figure 2.2: Schematic representation of the fluid traces for laminar, unstable and turbulent flow in a pipe. The velocity v_2 is higher than v_1. The diameter D_2 is larger than the diameter D_1. U:upstream, D:downstream

2.2.2 Sudden contraction and sudden expansion

The diameter is not the only geometrical feature with an impact on the flow field. For instance, flow in converging and diverging tubes are well known to have an impact, as depicted in Figure 2.3. Beside the previously reported relationship between pressure drop and volumetric flow in a pipe found by Poiseuille (equation 2.18), Young and Tsai [60], [61] reported that the pressure drop across a contraction or an expansion of a pipe Δp_{e-c} depends on the squared volumetric flow rate and on a coefficient K_t, as reported in equation 2.20. The coefficient K_t is a shape coefficient as its value depends on the shape (i.e. the converging or diverging angle) of the geometrical change.

$$\Delta p_{C-E} = \frac{\rho K_t}{2}\left(\frac{1}{A^2_{C-E}} - \frac{1}{A^2_P}\right)Q^2 \qquad (2.20)$$

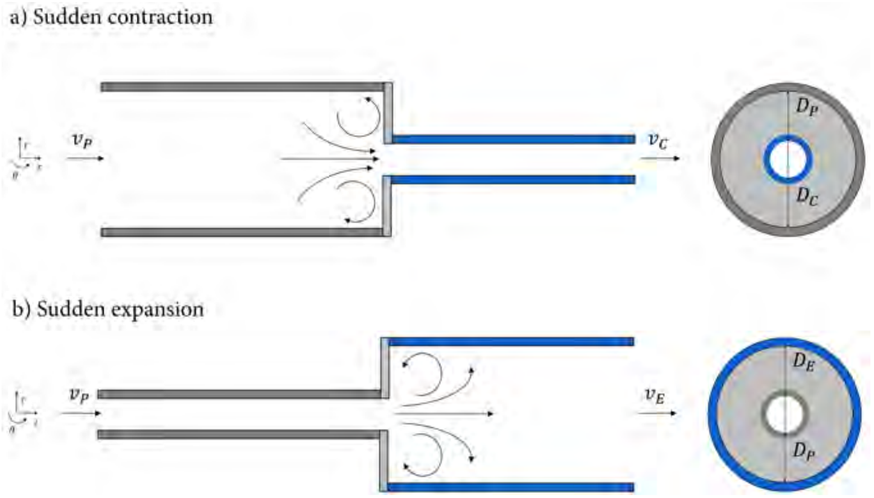

Figure 2.3: 2D schematic representation of the fluid traces for flow in a pipe with a sudden constriction (a) and sudden expansion (b). Adapted from [62].

2.2.3 Curvature

Furthermore, the curvature of the pipe has as well an impact on the flow field [63], [64]. As the flow enters the curvature site, the curved pipe walls impose curved streamlines and thus centrifugal forces. This will result in a radial pressure gradient that develops between the outer and the inner wall of the curved pipe, resulting in a skewed axial velocity profile. The secondary motion of the flow gives rise to two counter-rotating vortices in the normal plane, better known as Dean vortices [65]. The Dean number is defined as in equation 2.21, where δ is the ratio between the pipe diameter and 2 times the curvature radius. It represents the ratio between inertial *and* centripetal forces on viscous forces.

$$Dn = \delta^{0.5} Re \tag{2.21}$$

2.2.4 Pulsatility

Besides geometrical factors, the pulsatility of the flow can also have an impact on the flow regime. The Womersley number α [66] is defined in equation 2.22, where ω is the pulsation frequency, L is the pipe length and ν is the kinematic viscosity. The Womersley number α represents the ratio between transient inertial forces and viscous forces. The Womersley number has been claimed to be monotonically linked to the transition to turbulence in pulsatile flows [67]. On the other hand, a reduction of α was found to substantially delay the transition to turbulence to higher Re values [68].

$$\alpha^2 = L^2 \frac{\omega}{\nu} \tag{2.22}$$

2.3 BLOOD FLOW IN THE CARDIOVASCULAR SYSTEM

The typical Reynolds number in the CVS varies from 1 in small arterioles to approximately 4000 in the aorta and heart valves [69]. However, complex geometries are quite common in the cardiovascular tree. The biomechanical community is well aware of the so-called geometrical risk factors [70], such as sharply angulated branches of the bifurcation, asymmetric branching angles, and curvatures as the ones reported in Figure 2.4 and in Figure 2.5, where the velocity profiles in the carotid arteries rarely resemble the ones of a fully developed flow. These geometrical factors can lead to an altered wall shear stress (WSS), altered oscillatory shear index (OSI), and flow separation [70]. The geometry related flow disturbed phenomena are known to impair mechanotransduction mechanisms, which leads to pathological conditions [71].

The carotid bifurcation is considered one of the most critical tracts of the arterial tree for atherosclerosis, since it is predisposed to several geometrical risk factors [70], [72]. A representation of the complexity of the carotid arteries flow is reported in Figure 2.6. Focusing on the carotid arteries, the main pathological conditions that are caused by flow disturbed phenomena are aneurysms and atherosclerosis-induced stenosis, as previously introduced in section 1.3.

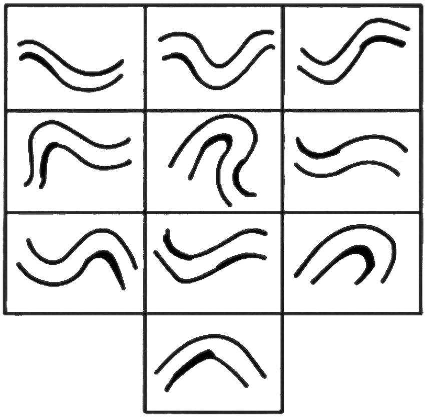

Figure 2.4: Drawings of the several geometrical risk factors that can be found in the carotid arteries. Adapted from [70].

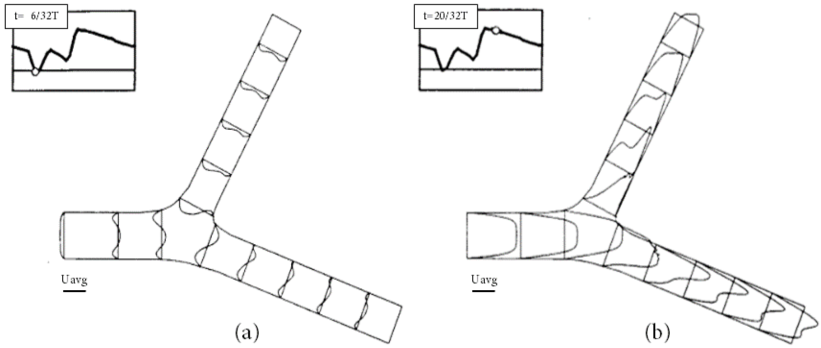

Figure 2.5: Non parabolic velocity profiles in the carotid arteries. Adapted from [69].

Figure 2.6: The flow separation region at the posterior wall of the internal carotid sinus is also the site of reverse velocities and secondary vortex patterns. Hydrogen bubble visualization of a carotid arteries model, adapted from [69].

2.3.1 Carotid aneurysms

Locally elevated WSS and OSI are highly correlated with the formation of aneurysms [73]. Furthermore, Valen-Sendstad et al [74] found high-frequency velocity fluctuations at the location at which aneurysms would have developed, as shown in Figure 2.7. The high-frequency fluctuations could be of relevance for understanding aneurysm initiation as it was found by Davies et al [75] that even low turbulent intensity caused the absence of cell alignment, indicative of impaired mechanotransduction.

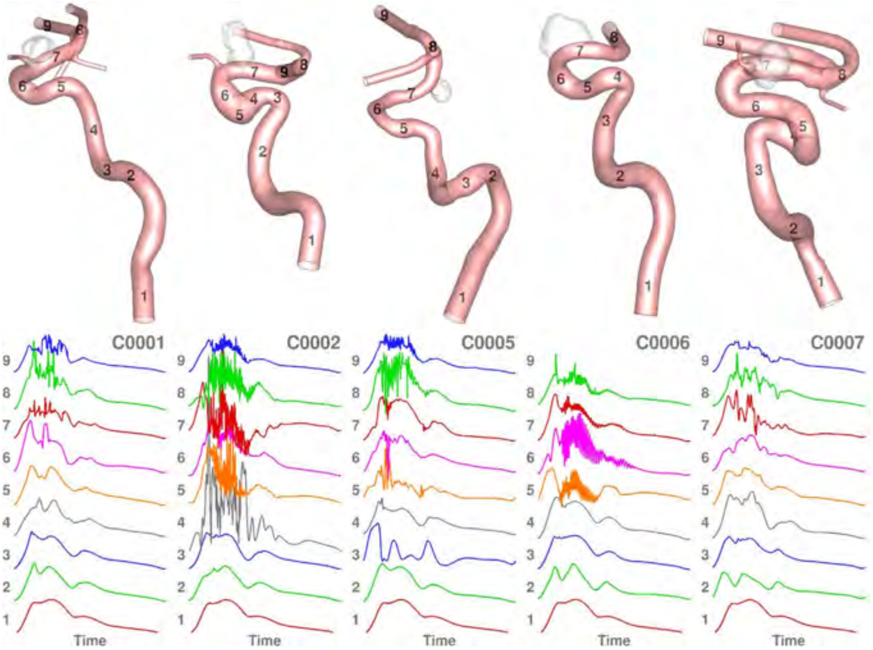

Figure 2.7: High-frequency velocity instabilities are thought to have a role in the initiation of ICA aneurysms. Adapted from [74]. Top: CFD models show extent of geometry, the (removed) aneurysm, and locations of the velocity probes. Bottom: corresponding velocity vs. time traces, normalized by their respective cycle averages, highlight varying degrees of flow instabilities.

2.3.2 Atherosclerosis and carotid stenosis

Low WSS and high OSI are known to be linked to the thickening of the arterial tunica intima, leading to atherosclerosis [9], [76]. Atherosclerosis is a chronic inflammation linked to the deposition of lipid material (better known as atheroma), in the sub-intimal layer of arterial walls [77], which protrude in the lumen of the artery. The occurrence of atherosclerosis is increased in the presence of risk factors such as, e.g., smoking, hypercholesterolemia, and diabetes [78].

The Reynolds number in a healthy carotid artery is approximately 300, based on the flow rate and diameters of Hoi et al [33] and Stergiopulos [79], for typical blood viscosity values. The Reynolds number in stenosed carotid arteries largely varies from 50 to 1200 with the stenosis severity [80], [81].

2.4 FLUID DYNAMICS OF STENOTIC CAROTID ARTERIES

It is in our interest to study the fluid dynamics in an idealized stenosed artery of diameter D, with only one entrance and only one exit, and with an inlet flow rate Q, constant throughout the pipe. The assumptions used to obtain equation 2.14 from the Navier-Stokes equations are valid in the current problem as well.

In Figure 2.8a, a fluid with kinematic viscosity ν is depicted flowing in a pipe of diameter D with velocity v. On the same conditions, the flow in an artery with a stenosis undergoes two changes, the first one by entering the stenosis, and the second one at its end. As shown in Figure 2.8b, the locations upstream, downstream and at the throat of the stenosis are referred to as U, D and S, respectively.

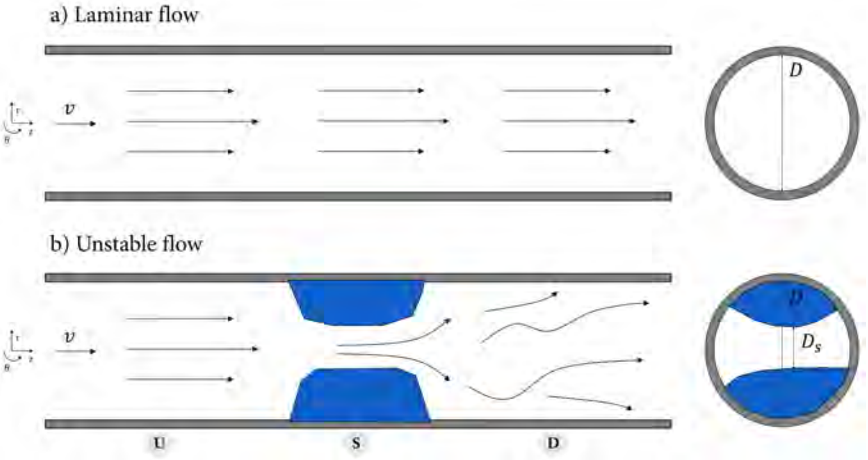

Figure 2.8: Schematic representation of the fluid traces for laminar flow in a pipe with diameter D (a) and unstable flow in a stenosed pipe with stenotic diameter D_S < D (b). The inlet velocity v and the fluid properties ν are the same. U: upstream of stenosis, S: stenosis throat, D: downstream stenosis.

By applying the previous equations to our problem, it is possible to understand that, with a constant flow rate ($Q_U = Q_S = Q_D$), the reduction of cross-sectional area A at the stenosis throat ($A_U = A_D > A_S$) induces a change in the resistance and hence in pressure and, in turn, in fluid velocity. Specifically, by entering the stenosis, the flow undergoes an acceleration, whilst the flow exiting the stenosis faces a deceleration: $v_S > v_U = v_D$. The change in downstream velocity is likely to induce flow instabilities and eventually turbulence, revealing a stenosis as an extremely risky geometrical factor. Flow instability or turbulence are three-dimensional time dependent processes which are characterized by a non-parabolic velocity profile, implying that the assumptions reported so far for the Navier-Stokes equations are not applicable. Therefore, it is not possible to obtain a simplified form of the Navier-Stokes equations for turbulent flows.

2.5 EXISTENCE AND SMOOTHNESS PROBLEM OF THE NAVIER-STOKES EQUATIONS

To this day, a solution of the Navier-Stokes equations has not been found yet, as a result of the mathematical difficulty of combining quadratic derivatives of several variables and time. The explicit solution has been found for a very limited number of cases, e.g. for the flow of a viscous fluid between two rotating cylinders (better known as Taylor–Couette flow), which are not applicable to most physiological and daily life situations. Therefore, the so-called *existence and smoothness* problem of the Navier-Stokes equations is a Millenium Prize problem, as the interest on turbulence is extremely high for its impact on several engineering applications, i.e. aeronautics, combustion and weather. Whilst the analytical problem remains unsolved, investigation on the physics of turbulence has been relentless, resulting in theories as the one reported in the following section.

2.6 KOLMOGOROV'S THEORY ON TURBULENT ENERGY CASCADE

In 1941, Kolmogorov introduced the concept of "cascade" to describe how energy is transferred from the larger to smaller scales into successively smaller eddies (i.e. fluid swirls), and how much energy is contained and/or dissipated by eddies of each size.

Consider a turbulent flow. At the large-scale, the turbulent flow has characteristic velocity v_0, length scale l_0 and time scale $t_0 = v_0/l_0$. The initial inertial energy is transferred at a transfer rate ϕ from the large-scale phenomena to subsequently smaller eddies by a degradation process (i.e. inertial range, at $l_\phi < l < l_e$), until the smallest eddies are dissipated by the viscosity forces at rate e (i.e. dissipation range, at $l < l_e$).

Furthermore, Kolmogorov hypothesized that the statistical properties of smaller scales are independent from the larger scales, as small-scale turbulent motions are statistically isotropic regardless of the eventual anisotropy of large-scales turbulent motions. This hypothesis implied that the flow properties at the small-scales depend only on the kinematic viscosity of the fluid

v, and on ϕ, which is reasonably equal to the rate at which the eddies are dissipated (e), providing equilibrium to the system. Therefore, the length, velocity and time scales at $l < l_e$ can be defined based on v and e, resulting in equations 2.23, 2.24 and 2.25, respectively.

$$\eta = \frac{v^{\frac{3}{4}}}{e^{\frac{1}{4}}}[m] \tag{2.23}$$

$$v_\eta = e^{\frac{1}{4}} v^{\frac{1}{4}} [\frac{m}{s}] \tag{2.24}$$

$$t_\eta = \frac{v^{\frac{1}{2}}}{e^{\frac{1}{2}}}[s] \tag{2.25}$$

Furthermore, the energy transfer rate ϕ is proportional to $\frac{v_0^3}{l_0}$, implying that the dissipation rate e is as well proportional to the larger scale phenomena, and can therefore be directly estimated. Therefore, by dimensionless analysis, it is possible to obtain the ratio between the small and large-scale results in equation 2.26, providing a relationship between small and large scales.

$$\frac{\eta}{l_0} = Re^{\frac{-3}{4}}, \frac{v_\eta}{v_0} = Re^{\frac{-1}{4}}, \frac{t_\eta}{t_0} = Re^{\frac{-1}{2}} \tag{2.26}$$

As demonstrated by Pope [82], the distribution of turbulent kinetic energy (tke) and of dissipation rate e in the different scales depends on the energy spectrum (E') in terms of wave number (κ, which is inversely proportional to the length scales: $\kappa = \frac{2\pi}{l}$), as reported in equations 2.27 and 2.28, respectively.

$$tke = \int_0^\infty E'(\kappa) d\kappa \tag{2.27}$$

$$e = \int_0^\infty 2v\kappa^2 E'(\kappa) d\kappa \tag{2.28}$$

As shown in equation 2.29, by applying Kolmogorov hypothesis, it is possible to obtain the expression of $E'(\kappa)$ in the inertial subrange (at $l_\phi < l < l_e$). The form of the energy spectrum provides a representation of how the turbulent kinetic energy distributes throughout the various wave numbers. The concepts of energy cascade are summarized in Figure 2.9.

$$E'(\kappa) = ce^{\frac{2}{3}} \kappa^{\frac{-5}{3}} \tag{2.29}$$

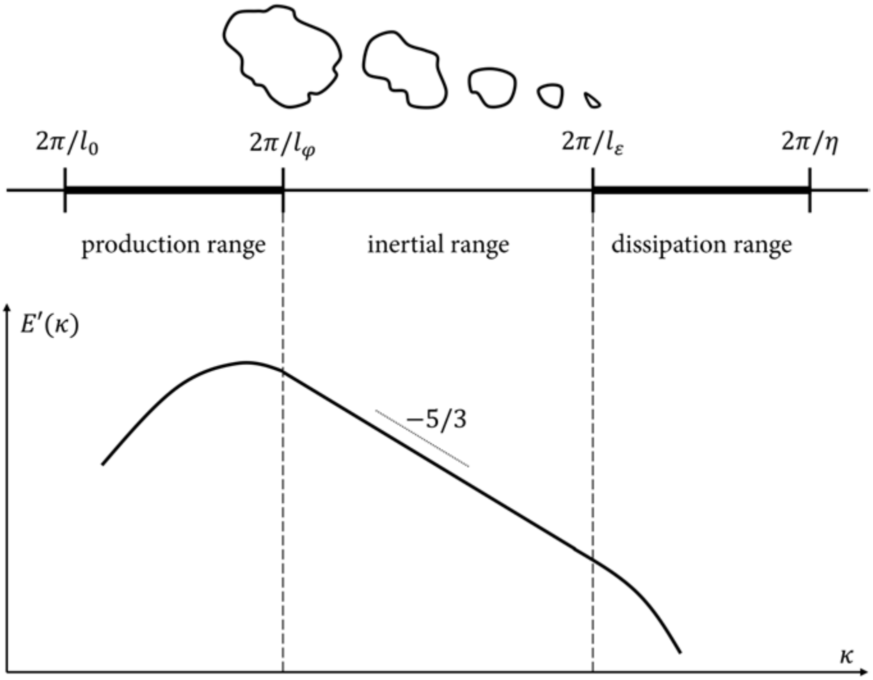

Figure 2.9: The energy of turbulent flows distributes differently in the production, inertial and dissipation ranges, as it depends on the length scale κ.

CHAPTER

3

RATIONALE FOR A COMBINED EXPERIMENTAL AND NUMERICAL APPROACH

The study of fluid dynamics is based on a threefold approach: analytical, experimental and numerical. This chapter reports an overview on each methodology in sections 3.1, 3.2 and 3.3, respectively. The rationale for performing a combined experimental and numerical analysis in the context of the current dissertation is reported in the final section 3.4.

3.1 ANALYTICAL APPROACH

As reported in the previous chapter (section 2.5), due to the severe limitations, the analytical solutions of the fundamental fluid dynamical equations have a very limited applicability, especially for unstable and turbulent flow, which is likely to be found downstream of a stenosis (section 2.4).

3.2 EXPERIMENTAL APPROACH

The empiric approach has always been helpful for improving the understanding of physical phenomena. For the relevance in the subject of study, it is worth mentioning the work that Giddens and Ahmed carried out: in 1983 they conducted experiments using Laser Doppler Anenometry on a rigid pipe with a 76 % symmetric restriction by imposing several Reynolds numbers (of

500, 1000 and 2000) with constant flow [8]. In the same year, they performed similar tests on a 25 % and a 50 % constriction [11] with several Reynolds numbers. Finally, they imposed a pulsatile flow rate on the rigid pipes with 25 %, 50 % and 75 % stenoses for a fixed Reynolds number of 600 [83]. The results of their analysis were extremely relevant for the understanding of the physics of the unstable flow downstream of a stenosis, as they observed several flow phenomena linked with the transition to different flow regimes, as depicted in Figure 3.1.

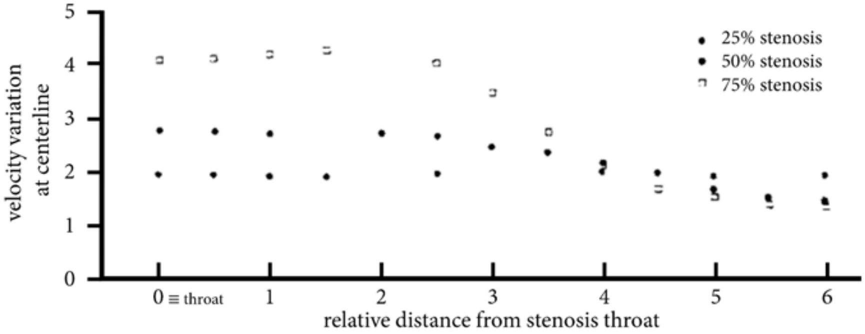

Figure 3.1: The experiments, carried out with constant flow at a Reynolds number of 2000 on three degrees of stenosis, detected a substantial difference of axial velocity at several centerline locations downstream the stenosis [11], adapted from same.

However, their investigation did not include models with more severe stenosis degrees, despite the atherosclerosis plaques are likely to grow enough to cause even more severe obstructions than a 75 %. Furthermore, over two years of investigation, they tested mainly constant flow or pulsatile flow with a fixed Reynolds number, whilst physiological pulsatile flow conditions are affected by intense variability, especially for a compromised CVS [84]. The material of the model was rigid, despite the compliant nature of arteries. Moreover, the experimental approach prevented the measurement of the relevant quantities at further locations. Point measures are intrinsically subjected to uncertainties and measurement errors. Furthermore, the time demand to obtain a sufficiently accurate and insightful experimental methodology is extremely time demanding. These limitations are typical of any experimental, or *in-vitro*, approach and, therefore, severely impact the possibility to perform complete parametric investigations of a fluid dynamical phenomenon.

3.3 NUMERICAL APPROACH

In order to overcome the limitations of the *in-vitro* and analytical approaches experienced by the entire fluid dynamical community, over the past century, scientists have developed a Computational Fluid Dynamics (CFD) approach. It consists in simulating the motion of a fluid, hence approximating the solution of the Navier-Stokes equations [85]. It allows to obtain a complete description of the flow variables (e.g. pressure and velocity) as function of space and time in the entire fluid domain [86]. If performed by using robust numerical strategy, CFD is able to produce reliable quantitative predictions and/or analyses of fluid flow phenomena.

In order to provide an overview of the approach, the process is presented in layman's terms in the current section. The CFD process can generally be divided in the steps shown in Figure 3.2.

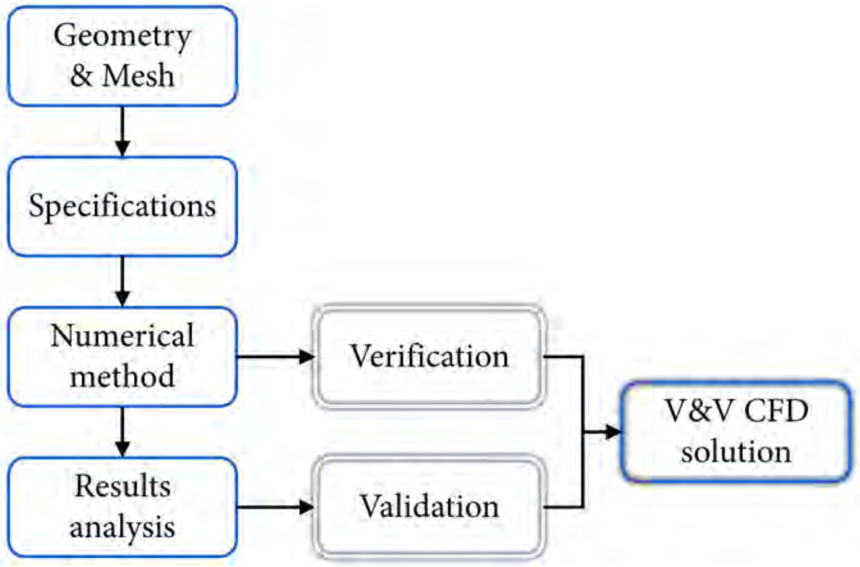

Figure 3.2: Strategic flowchart for a CFD simulation. Verification and validation result in a robust numerical solution.

- **Geometry & Mesh** - the geometry is the fluid domain, the mesh is the grid into which the geometry is subdivided (or *discretized*) [87]. For biomedical applications, the geometry is usually obtained (or *segmented*) from anatomical patient-specific images [88]. The grid cells can have different size, which defines the density of the mesh, and shape: for three-dimensional geometries, it is possible to create several types of cells, e.g. hexahedral or tetrahedral.

- **Specifications** - refer to the ensemble of boundary and other conditions applied to the specific numerical problem. The effort is to set specifications as similar as possible to the physical (see section 2.1) and physiological (Reynolds number, pulsatility, time dependency) reality [89]. For instance, the no-slip condition is usually applied to the walls. A physiological waveform as the one of Hoi et al [33] (see section 1.2) is typically used at the inlet of carotid arteries models (i.e. the CCA). A pressure or a flow condition is applied to the outlet of the model. In the presence of a bifurcated geometry, often a flow split condition (based on fixed values or on a Womersley model [90]) is set at the outlets.

- **Numerical method** - consists in the discretization and linearization of the variables of the integral form of the PDEs on each grid cell. The most common methods by which the equations are discretized are:
  - Finite Volume Method: the mesh is considered as a set of finite control volumes as in Figure 3.3a. The values of each variable ϕ (including pressures and velocities) are defined on a staggered grid. The discretized equations are obtained by integrating locally the governing equations over each control volume.

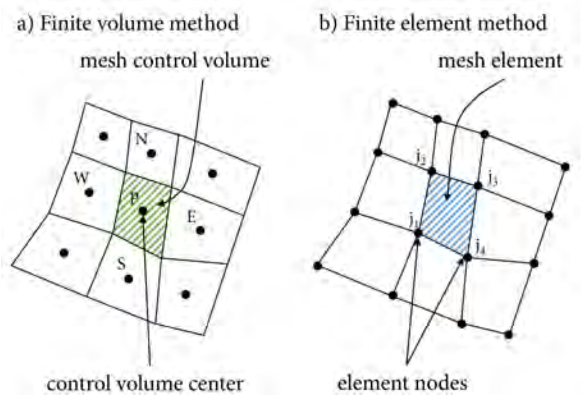

Figure 3.3: a) finite volume method or b) finite element method for numerical discretization of 2D domain. Adapted form [91].

  - Finite Element Method: it is based on the Galerkin method, which converts the continuous operator (i.e. the Navier-Stokes PDE) to a discrete formulation. The space is characterized by polynomial basis functions P_j, onto which the variables ϕ within each element are interpolated in terms of the values ϕ_j at a set of the nodal points $j = 1 : n$ (where $n = 4$ in the example of see Figure 3.3b), thus guaranteeing the continuity of the solution across the domain [91], as in equation 3.1.

$$\phi = \int_{j=1}^{n} P_j \phi_j \tag{3.1}$$

> Please note that the precise and comprehensive comparison of the two methods is out of the scope of this dissertation. Please refer to [91] for a more insightful description of the similarities and differences between finite element and finite volume methods. Among finite element methods, the spectral element method deserves particular attention because of its use of high-degree piecewise polynomials as basis functions. This is of primary importance to capture the dissipation of the turbulent kinetic energy, thus resulting in being particularly suitable for the analysis of unstable and turbulent flows [12], [92], typically at the cost of simpler geometries [93].

Furthermore, implementation methodologies [94] also impact the accuracy of the solution. For instance, the numerical schemes are typically iterative, as they aim to re-iterate the calculation until reaching the required threshold for accuracy.
There are several excellent commercial softwares (e.g. Fluent Ansys), which are applicable to any fluid dynamical problem. However the black box interface and the difficulty of tuning default settings into suitable settings (i.e. not too dissipative) may result in a lower suitability for transitional flows. On the other hand, open-source softwares are often developed with algorithms predisposed to efficiently solve specific fluid dynamical problems. For instance, the methodology applied in the current work was performed by means of *Oasis*, a high-performance Navier-Stokes equation solver, developed within Simula Research Laboratory, especially thought for solving unstable and turbulent flows. It is based on a finite element method fractional step method [95] and its code was verified whereby **verification** is the process of determining the mathematical correctness in the implemented numerical algorithms that could impact the accuracy of the computational results [96], [97].

In the context of unstable and turbulent flows, it is worth mentioning the difference between Direct Numerical Simulation (DNS) and Large Eddy Simulation (LES). In the DNS approach, the entire range of turbulent scales is resolved. A functional LES, on the other hand, resolves the larger scales and models the smaller ones (for $\kappa < \kappa_{LES} = \frac{2\pi}{l_{LES}}$ as in Figure 3.4) by using sub-grid scale (SGS) models [98]. SGS models are based on adding artificial viscosity ν_{SGS} to dissipate kinetic energy of the sub-grid scales. The resulting flow field depends on how the model is implemented (e.g. constant or dynamically calculated ν_{SGS}) [99], [100]. By modeling the smaller scales instead of resolving them, the LES approach is typically less expensive but less accurate than a DNS simulation [86]. Please refer to chapter 4, wherein the comparison between DNS and LES approaches for the study of fluid dynamics downstream of a stenosed carotid artery is discussed [101].

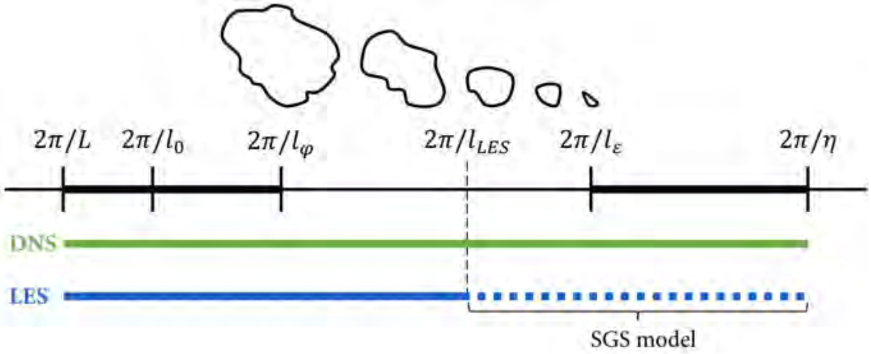

Figure 3.4: A Direct Numerical Simulation resolves all turbulent scales, whereas a Large Eddy Simulations models the smaller ones using a SGS model.

- **Results analysis** - consists in the investigation of the physical sense of the numerical solution. The assessment of the accuracy of computational methodology is performed by comparing the numerical solution against experimental measurements. This process is better known as **validation**, and its purpose is to identify and quantify the error and uncertainty in the numerical models against the real world [97]. The fluid solver *Oasis* used in the current work was validated against in vitro experimental measurements of jet breakdown location from the FDA nozzle benchmark [102] in 2018.

3.4 A CFD parametric study of an experimental technology: a combined effort

With the purpose of providing a proof-of-concept on the feasibility of carotid stenosis detection by using Laser Doppler Vibrometry, we performed several experimental measurements on both compliant and rigid replicas of the Computed Tomography Angiography images of an affected patient (please refer to chapter 5, [103]). It is important to state that similar difficulties of Giddens and Ahmed [8], [11], [83] (please refer to section 3.2) were encountered in our study as well. Despite our best effort to overcome the limitations of the experimental methodology (by performing tests on tubes with several materials, at several flow conditions and rates, and at several locations both upstream and downstream the stenosis), we were simply not able to perform measurements with several degrees of stenosis. Pleaser refer to chapter 5 for the complete methodology [103].

The intrinsic limitations of the experimental methodology prevented a parametric study, which lead to the use of CFD. The trade-off between accuracy and computational cost of DNS and LES approaches, for our context, was explored as reported in chapter 4, [101]. The validation of the computational methodology was hence performed as in chapter 6, [104], wherein the parametric study was subsequently conducted in order to assess the impact of degree of stenosis, flow rates, flow split, velocity and Reynolds number on the intensity of post-stenotic flow instabilities.

II

Flow instabilities: predictors of carotid stenosis

Chapters

4 **High-frequency instabilities: a strategy in-silico study** **43**

5 **Laser Doppler vibrometry: a feasibility in-vitro study** **75**

6 **Flow instabilities for stenosis detection: a combined approach** **93**

Chapter 4

High-frequency instabilities: a strategy in-silico study

This chapter introduces a Computational Fluid Dynamics methodology focused on turbulence modeling, specifically on the several approaches that could potentially allow to obtain an accurate estimate of the turbulent kinetic energy at the scales of interest. The chapter is based on the paper "High-Frequency Fluctuations in Post-stenotic Patient Specific Carotid Stenosis Fluid Dynamics: A Computational Fluid Dynamics Strategy Study", *Cardiovascular Engineering and Technology*, vol. 10, no. 2, pp. 277-298, 2019 [101].

4.1 Introduction

Carotid stenosis is a progressive and local buildup of plaque in the carotid bifurcation, leading to a local narrowing of the lumen. The major risk consists of plaque rupture with subsequent debris and thrombi being transported downstream where they can cause a blockage leading to a stroke and consequent neurologic deficits [105]. Asymptomatic carotid artery stenoses, which affects 1.6 % of the population [106], are rarely detected unless diagnosed with another associated cardiovascular disease [4].
A characteristic feature of stenoses is that the downstream flow is turbulent-like, with high-frequent pressure fluctuations [10]. These fluctuations can traverse the soft neck tissue as mechanical waves, and present as a bruit or skin vibration. The stenosis-induced turbulent-like flow is therefore a strong

marker for inferring the presence of a stenosis.

The current clinical practice for asymptomatic stenoses screening is auscultation of the carotid bruit [3]. Auscultation is only applied if the physician suspects presence of a stenosis, i.e. if correlated risk factors are present [4], and is operator-dependent, with low sensitivity [107] due to the presence of background noise [108]. Carotid auscultation is hence not sufficient to infer the presence of a stenosis, whose diagnosis hence requires confirmation by techniques which are usually not available to a general practitioner, i.e. ultrasound or tonometry.

To overcome the abovementioned challenges, the CARDIS project proposes to instead infer the presence of stenosis by measuring skin vibrations using a newly developed multi-beam laser Doppler vibrometry device [20], with increased temporal resolution, with 10 μs at a sample rate of 100 kHz, and reduced noise level [21]. The device has already proven suitable for measuring physiological signals from skin movements, such as pulse wave velocity and heart rate [16], [17]. The new device could allow rapid and consistent non-contact screening for asymptomatic carotid stenosis, and thus detection prior to a traumatic event. As part of this project, we combine *in-vitro* experiments and computational fluid dynamics (CFD) flow simulations to show a 'theoretical' proof of concept of the device before clinical testing. However, the efficacy of CFD relies on the robustness of the numerical methods and their ability to reproduce experimental results, and has proven challenging, especially for transitional flows [102]. In particular, the use of numerical schemes, such as first order UPWIND schemes, well-known to be dissipative [109], is common in the biomedical literature [110]. The choice of the correct numerical methodology is hence crucial for reliable simulations.

We have previously used an under-resolved Direct Numerical Simulation (DNS) approach with rigid walls for two biomedical benchmarks [102], [111] and biomedical applications such as aneurysms [74], [112], [113] and vascular junctions [114]. The first aim of this study was to find an adequate under-resolved DNS solution from a spatial and temporal refinement study with respect to the smallest scales, and from a pragmatic biomedical engineering point of view balancing the computational cost with accuracy.

Directly calculating the smallest scales of the turbulent-like flow requires large computational resources, and is therefore not routinely performed in the biomedical literature. However, we also know that the smallest scales have little energy, and only contribute to dissipation. We can therefore model these scales, for instance by means of large eddy simulations (LES). Applying LES can allow for the use of a coarser grid, since we can model the scales we do not capture, referred to as the sub-grid scales (SGS). LES simulations depend on the properties of the SGS model, for instance its ability to mimic the near-wall behavior. The second aim of this study was therefore to assess whether three commonly used SGS models (Smagorinsky, Sigma and

Dynamic Smagorinsky) are able to replicate our reference solution for both constant – at peak systole – and pulsatile flow rates on a coarser mesh, and thus reducing computational cost without significant loss of resolution of the high-frequent flow features. The study was performed in an anatomically correct model geometry, retrieved from a patient with significant carotid stenosis, subjected to physiologically relevant boundary conditions.

4.2 METHODS

Computed tomography angiography images of a common carotid bifurcation with severe stenosis (76 % narrowing computed by means of the *North American Symptomatic Carotid Endarterectomy Trial* method [105]) in the internal carotid artery (ICA) were obtained from a 75 years old male patient, who gave informed consent for the use and further processing of the images.

The medical images were segmented using 3D Slicer [115] to obtain an anatomically plausible model of the vasculature, and the inlets – the common carotid artery (CCA) - and outlets – the ICA and the external carotid artery (ECA) - were extruded using PyFormex [116] to ensure that the flow was fully developed. Depicted in Figure 4.1 are the full computational domain (a), and the region of interest (b). The relevant fields were evaluated in point **P**, on four slices (A, B, C and D), two orthogonal lines per slice (Figure 4.1c), and points along the centerline. Point **P** was located 8 mm, 1 CCA diameter (d), downstream of the stenosis, and the slices A, B, C, and D were located -0.75d, 0.0d, 0.6d, and 1.2d, relative to the center of the stenosis, respectively.

We used the Vascular Modelling Toolkit [117] to create five meshes with a local refinement in the stenosed and downstream region, with the same size ratio between the coarse and fine region for all meshes. The resulting meshes had 200 thousand (K), 2 million (M), 6 M, 22 M, and 50 M tetrahedral elements, now referred to as the $200K$, $2M$, $6M$, $22M$ and $50M$ meshes, respectively. Mesh details are listed in Table 4.1. An additional mesh with 11 million elements ($11M$) was created similarly in order to allow a preliminary common simulation, as better explained in the next paragraphs.

The fluid properties were set to mimic water, a Newtonian fluid with kinematic viscosity of $\nu = 1 \cdot 10^{-6}$ m^2/s to ease future comparison to *in-vitro* experiments. We applied two types of inlet conditions; a parabolic profile with constant flow rate of 520 ml/min leading to a Reynolds number (Re) of 1380, and a pulsatile Womersley flow (averaged flow rate of 370 ml/min) with period of 1 second and an averaged Re = 980 [11], see Figure 4.2. The

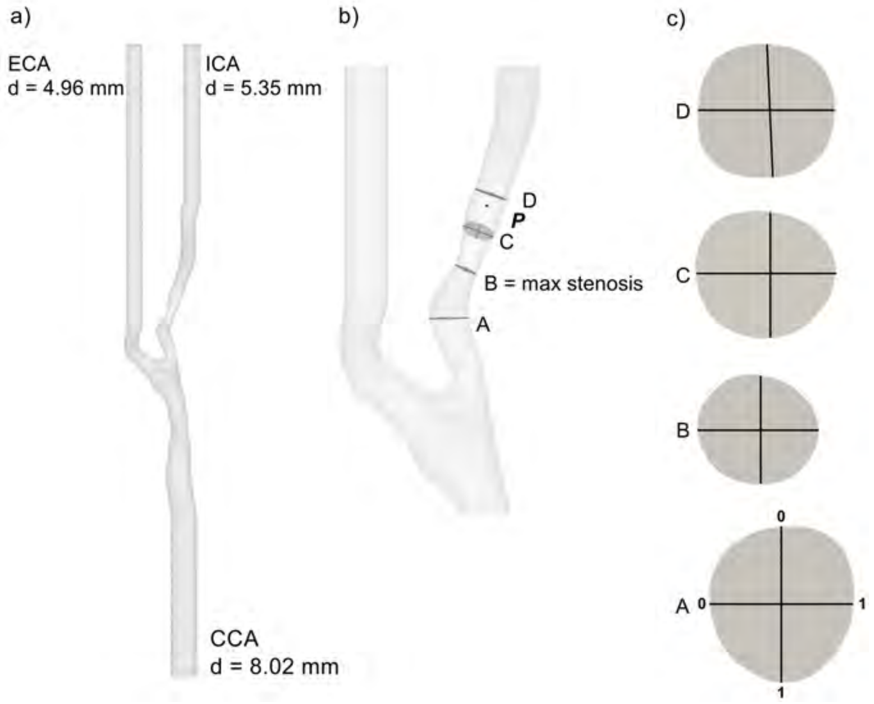

Figure 4.1: Patient-specific geometry with flow extensions, where 'd' indicates the diameters of CCA, ECA, and ICA. (b) The point **P**, the slices A, B, C, and D and two perpendicular lines on each slice, with a detail of each slide in (c), indicate where the velocity and pressure were sampled.

Mesh name	**Number of elements (approximation)** (-)	**Average cell length** Δx (m)	**Number of boundary layers** (-)
200K	$2 \cdot 10^5$	$9.13 \cdot 10^{-4}$	1
2M	$2 \cdot 10^6$	$4.63 \cdot 10^{-4}$	4
6M	$6 \cdot 10^6$	$3.04 \cdot 10^{-4}$	4
22M	$22 \cdot 10^6$	$1.92 \cdot 10^{-4}$	4
50M	$50 \cdot 10^6$	$1.44 \cdot 10^{-4}$	4

Table 4.1: Mesh characteristics

former is to enable rigorous worst-case assessment of the smallest temporal and spatial scales in the flow, although at the cost of losing the pulsatility in a physiological flow condition.

We assumed rigid walls, prescribed a no-slip boundary condition along the vessel walls, and enforced a flow split of 43.8% in the ICA/CCA, based on the model presented in Groen et al [118] by prescribing a Womersley profile on the ECA outlet and zero pressure at the ICA outlet.

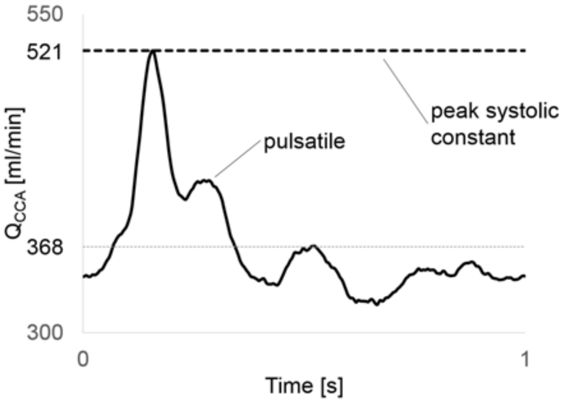

Figure 4.2: A typical carotid artery waveform (average 368 mL/min, peak 521 mL/min) was used in this study. Constant flow rate equivalent with peak systolic flow was set as inlet flow for the refinement study in order to allow a more rigorous assessment of grids resolution.

To cheaply washout initial transients associated with the artificial initial conditions we computed the flow at the 11M mesh for 2 physical seconds, equivalent of one and a half flow-throughs with model length of 0.2 m and peak inlet velocity of 0.15 m/s. We projected the last time step of the solution onto each mesh as an initial condition.

Simulations were performed using the open-source verified [95] and validated [102] finite element CFD solver *Oasis* [95], where special care was taken to ensure a kinetic energy-preserving and minimally-dissipative numerical solution of the Navier-Stokes equations. We used linear Lagrange elements $P_1 - P_1$ for both velocity and pressure.

The spatial refinement study was simulated with $\Delta t = 5 \cdot 10^{-5} s$, while the temporal refinement study was performed on the least computationally expensive mesh which gave adequate results with varying time step: $\Delta t = 1 \cdot 10^{-4}, 5 \cdot 10^{-5}, 1 \cdot 10^{-5}$ and $5 \cdot 10^{-6}$ seconds. The pair of Δt and mesh size that provided the best tradeoff between computational cost, and accuracy of resolving high-frequent flow features was used as the reference solution for comparison with the LES simulations.

A generic form of functional SGS models can be described as in equation 4.1, whereas the SGS viscosity (ν_{SGS}) is defined in equation 4.2.

$$\tau_{ij}^{SGS} - \frac{1}{3}\tau_{kk}^{SGS} \cdot \delta_{ij} = 2\rho\nu_{SGS}(S_{ij} - \frac{1}{3}S_{kk} \cdot \delta_{ij}) \tag{4.1}$$

$$\nu_{SGS} = (C_m \cdot \Delta)^2 \cdot D_m(\mathbf{u}) \tag{4.2}$$

The SGS tensor τ^{SGS} depends on the fluid density ρ, the strain tensor of the resolved scaled S, on the Dirac delta function δ and on the subgrid-scale viscosity ν_{SGS} , which is a function of the cut-off length scale Δ and of two model-specific parameters D_m and C_m. D_m is the model specific differential operator related to the resolved velocity field $\mathbf{u}$ and it sets the properties of the model, for instance, the near wall behavior. C_m is the model constant and it sets the amount of energy drained from the resolved scales.
We applied three different SGS models: the static Smagorinsky model [100] with $C_m = 0.168$, the Sigma model [119] with $C_m = 1.5$, and the dynamic Smagorinsky model, for which the model-specific parameters were updated every time step following Meneveau et al. (1996) [99]. The LES simulations were performed on the mesh with one spatial refinement level lower, i.e., on a coarser mesh, relative to the reference solution, but with the same Δt to ensure a fair comparison. The number of cores, reported in Table 4.2, was kept constant for each mesh, regardless of time step or SGS model. The workload of each simulation was obtained as number of cells divided by number of cores. All simulations were stopped after 5 physical seconds and flow statistics were based on the last four seconds, as one physical second was quantitatively found to be sufficient for washing out the artifacts from the initial condition. A list of all simulations can be found in Table 4.3.

For visual inspection of the coherent vortical structures in the turbulent-like post-stenotic flow we computed the Q-criterion as in equation 4.3, which

Mesh name	**Number of cells**	**Number of cores**	**Workload**	**Workload / $6M$ workload**
$200K$	$174.37 \cdot 10^3$	16	$1.09 \cdot 10^4$	0.06
$2M$	$1.84 \cdot 10^6$	16	$1.15 \cdot 10^5$	0.62
$6M$	$5.97 \cdot 10^6$	32	$1.87 \cdot 10^5$	1.00
$22M$	$22.43 \cdot 10^6$	96	$2.34 \cdot 10^5$	1.25
$50M$	$51.14 \cdot 10^6$	128	$4.00 \cdot 10^5$	2.14

Table 4.2: Number of cores and workload per core for each simulation. The number of nodes was kept constant for each mesh. There were 16 cores in each node.

Study	Mesh size	Δt (s)	Inlet type	SGS model
Spatial Refinement	**200K**	$5 \cdot 10^{-5}$	Constant	None
	2M	$5 \cdot 10^{-5}$	Constant	None
	6M	$5 \cdot 10^{-5}$	Constant	None
	22M	$5 \cdot 10^{-5}$	Constant	None
	50M	$5 \cdot 10^{-5}$	Constant	None
Temporal Refinement	$22M$	$1 \cdot 10^{-4}$	Constant	None
	$22M$	$5 \cdot 10^{-5}$	Constant	None
	$22M$	$1 \cdot 10^{-5}$	Constant	None
	$22M$	$1 \cdot 10^{-6}$	Constant	None
Large Eddy Simulation	$6M$	$5 \cdot 10^{-5}$	Constant	**Smag.**
	$6M$	$5 \cdot 10^{-5}$	Constant	**DynSmag.**
	$6M$	$5 \cdot 10^{-5}$	Constant	**Sigma**
	$6M$	$5 \cdot 10^{-5}$	Pulsatile	**Smag.**
	$6M$	$5 \cdot 10^{-5}$	Pulsatile	**DynSmag.**
	$6M$	$5 \cdot 10^{-5}$	Pulsatile	**Sigma**
Reference solution	$6M$	$5 \cdot 10^{-5}$	Pulsatile	None
	$22M$	$5 \cdot 10^{-5}$	Pulsatile	None

Table 4.3: List of the simulations performed for the three studies reported in this paper, with details on the mesh size, time step size, inlet type, end time and SGS model. The text in bold highlights the parameters changed in each category.

is a spatial region where the Euclidean norm of the vorticity tensor $\overrightarrow{\Omega}$ dominates the strain rate tensor $\overrightarrow{S}$ [120].

$$Q - criterion = \frac{1}{2}[|\overrightarrow{\Omega}|^2 - |\overrightarrow{S}|^2] > 0 \tag{4.3}$$

Reynolds decomposition was used for all constant flow rate simulations to separate the instantaneous velocity, $\mathbf{u}(\mathbf{x}, t)$, from the time averaged, $\overline{\mathbf{u}(\mathbf{x})}$, and fluctuating, $\mathbf{u}'(\mathbf{x}, t)$, components, i.e., $\mathbf{u} = \overline{\mathbf{u}} + \mathbf{u}'$. Taking the fluctuating velocity magnitude signal, $|\mathbf{u}'|$, as input we computed the power spectral density (PSD) using Welch's method [121] with 16 segments and a Hanning windowing function with 50 % overlap. The turbulent kinetic energy tke was calculated as in equation 4.4.

$$tke = \frac{1}{2}\sum_{i=1}^{3} \overline{\mathbf{u}'(\mathbf{x_i}, t)^2} \tag{4.4}$$

where $\mathbf{u}'(x_{i=1:3}, t)$ are the components of the fluctuating velocity.
For pulsatile simulations, however, the Reynolds decomposition was no longer directly applicable as it was not possible to obtain a mean flow without simulating tens of cardiac cycles to obtain a phase averaged mean. We therefore applied a high pass filter, like suggested by Khan et al [122], to the original pulsatile velocity $\mathbf{u}(x, t)$ to obtain a good approximation for $|\mathbf{u}'|$. We created a fast Fourier decomposition with 1000 components of the velocity signal, and we set the first 16 modes, representing the low frequencies, to 0, see Figure 4.3 for a visual example.

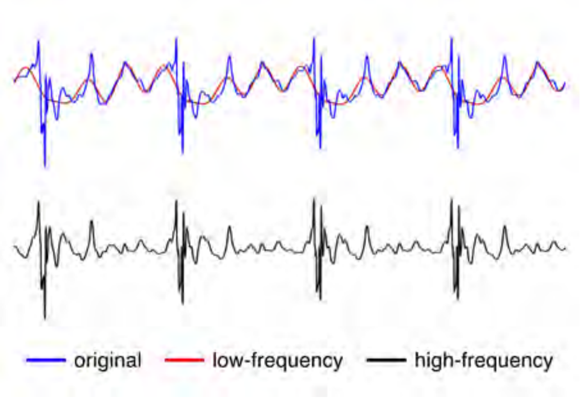

Figure 4.3: The original velocity signal was decomposed in 1000 harmonics and its low-frequency components were separated from the high-frequency components by means of a 16^{th} mode threshold.

4.3 RESULTS

4.3.1 General Flow Features

We first focused on the instantaneous flow features at t = 2.0 s obtained on the 22M-element mesh with $\Delta t = 5 \cdot 10^{-5}$ seconds and a constant flow rate (Figure 4.4). The top of Figure 4.4 shows that the flow in the CCA was stable until the carotid bifurcation, while vortical structures formed at the bifurcation. Moreover, because of the non-parabolic flow entering the ICA and pronounced curvature, the flow became unstable already upstream of the stenosis, as observed in the left most section of the zoomed in box, see Figure 4.4 – bottom panel. The flow accelerated through the stenosis before the jet broke down into an unstable flow downstream of the stenosis. The flow instabilities quickly dissipated further downstream, and the flow relaminarized.

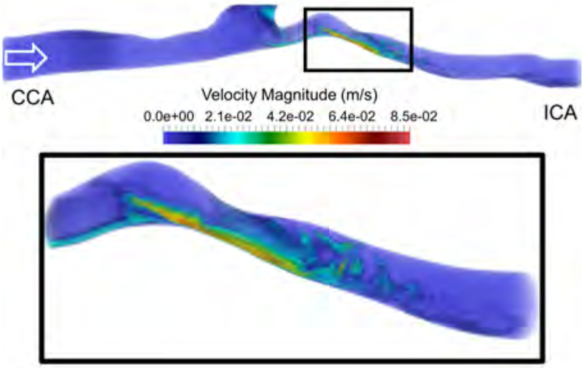

Figure 4.4: Top panel: volumetric rendering of the instantaneous velocity magnitude in the common and internal carotid arteries. Bottom panel: enlargement of the box in the top panel, focusing on the stenosis and downstream region. The flow became perturbed already before reaching the stenosis. The flow then accelerates in the stenosis and decelerates once out, causing the jet to break down into turbulent-like structures.

4.3.2 Sensitivity Analysis

4.3.2.1 Spatial Refinement Study

We first performed a qualitative assessment of the spatial refinement study based on the Q-criterion of instantaneous velocity fields in the ICA at identical time points (t = 2.0 s). In Figure 4.5, from left to right with increasing mesh resolution, one can observe a consistent increase in the number of vortices. In the $2M$ and $6M$ meshes, it is possible to observe some larger coherent vortical structures, while in the $200K$ mesh these were almost entirely absent. However, the $22M$ and $50M$ element simulations showed smaller and more complex structures and were hence phenotypically different from the $2M$ and $6M$. The vortices of the downstream region were visually easier to see in the $50M$ than in the $22M$, however one can observe the same type and distribution of vortices, showing similarities between the $22M$ and $50M$ meshes.

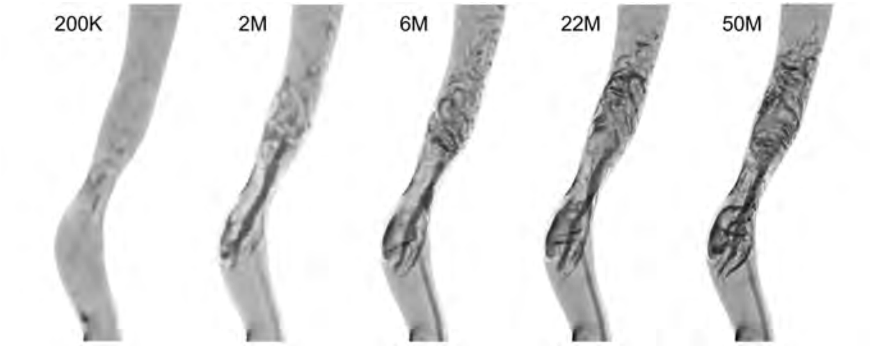

Figure 4.5: Q-criterion representation for the 5 meshes: the vortical structures in the ICA for the 200K mesh are almost entirely missing, the 2M and 6M meshes already show some turbulent-like flow features, but it is only on the 22M and 50M that these vortical structures are clearly distinct.

To further assess the results of the spatial refinement study, we considered the time-averaged *tke* obtained by Reynolds decomposition of the velocity across two perpendicular lines on each of the four slices A – D, previously shown in 4.1c. The left panel of Figure 4.6 depicts the *tke* values along the vertical (top to bottom) and horizontal (left to right) lines for each slice. In all lines, both upstream and downstream of the stenosis, we observed that while the 200K-element simulation was not alike any other simulation, the 2M and 6M ones were similar, but relatively different from the 22M and 50M simulations. Of note is also that even though the spatial resolution of 200k element simulation was too coarse to capture any vortex structures in Figure 4.5, the flow is still turbulent-like with high-frequent fluctuations, as evident in 4.6a.

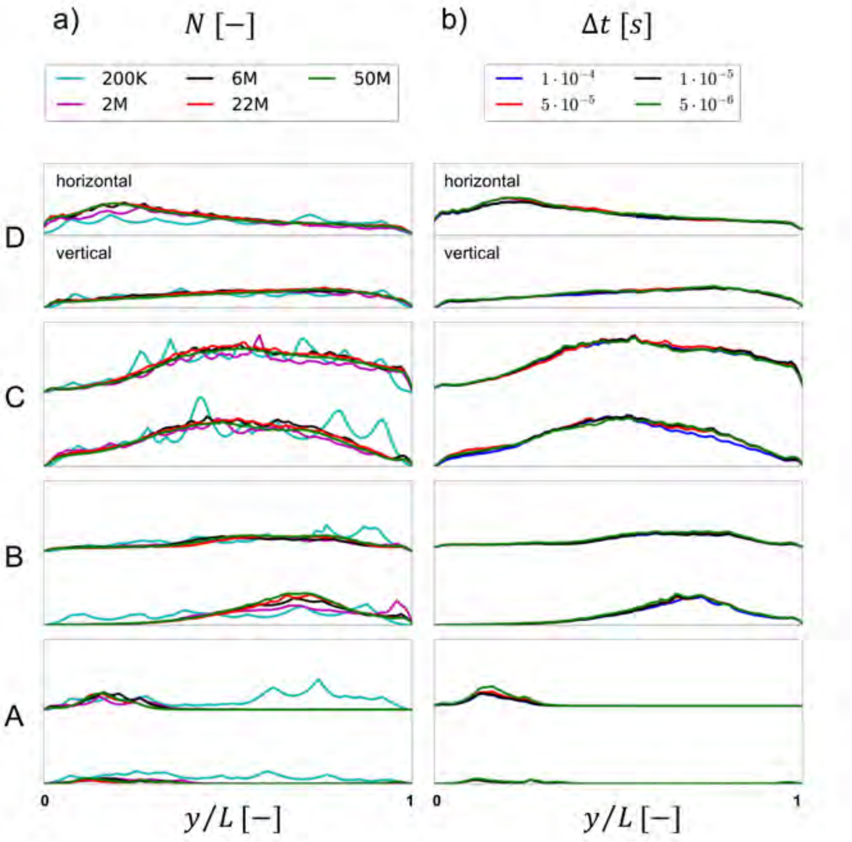

Figure 4.6: Time-averaged *tke* over vertical and horizontal lines on slices A to D for the five meshes in a) and for the four time steps in b).

We also investigated the power spectral density (PSD) of the magnitude of the fluctuating velocity (|**u'**(**x**,t)|) at point **P**. In Figure 4.7a, it is possible to observe again that the 200K, 2M, and 6M simulations differed from the two finest simulations, which for all practical purposes were indistinguishable. To further support these results, we also show the tke for all available meshes in slices A – D (Figure 4.12) in Appendix 4.6 and the PSD of the fluctuating velocity, **u'**(**x**,t), in five additional points along the ICA. Based on these observations, the 22M simulation was considered to be the best tradeoff between computational cost and accuracy. The temporal refinement study was hence performed on the 22M mesh.

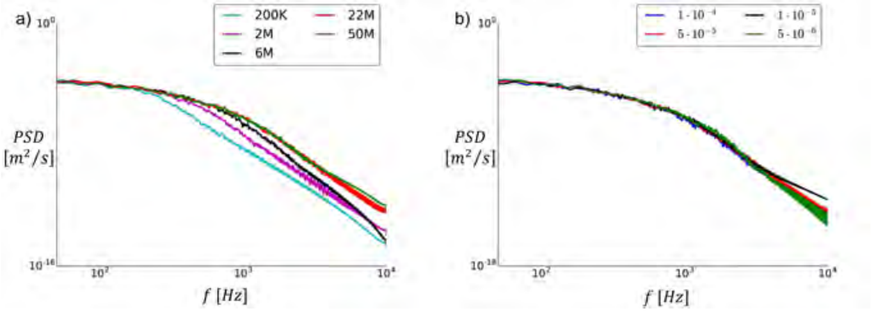

Figure 4.7: Power Spectral Density of the several meshes (a) and time steps (b) evaluated at point **P**.

4.3.2.2 *Temporal Refinement Study*

The temporal refinement simulations were evaluated similarly to the spatial refinement study. In all lines, the tke with Δt equal to $5 \cdot 10^{-5}$, $1 \cdot 10^{-5}$ and $5 \cdot 10^{-6}$ seconds (Figure 4.6b) were close to indistinguishable. In contrast, the $1 \cdot 10^{-4}$ seconds simulation differed slightly in the lines on slices A, B, and C. The contours for the available time steps are shown as well in the Appendix 4.6, with consistent results. Furthermore, the PSD of the fluctuating velocity component shown in Figure 4.7b confirms that the impact of temporal refinement is small, however the plots in Figures 4.19, 4.20, 4.21, 4.22, 4.23 of the Appendix 4.7 show a slight difference between $\Delta t = 1 \cdot 10^{-4}$ seconds and the rest.

Based on the results from the spatial and temporal refinement study the 22M mesh ($\Delta x = 1.92 \cdot 10^{-4}$ m) and time step of $\Delta t = 5 \cdot 10^{-5}$ seconds offered the best tradeoff between computational cost and accuracy, and is now referred to as the *reference solution*.

4.3.3 Large Eddy Simulations

4.3.3.1 *Constant Flow Simulations*

For the constant flow rate LES simulations we first focused on the added viscosity from the SGS models (ν_{SGS}), and tke in slice C, as shown in Figure

4.8. Although the order of magnitude of ν_{SGS} is the same for all models, the tke of the Smagorinsky model was phenotypically different showing an improper near-wall behavior. Due to the shortcomings of the Smagorinsky SGS model, it was not included in the pulsatile flow simulation discussed further below. The added viscosity of the Dynamic Smagorinsky model was overall lower compared to the Sigma model, but leading to a comparable tke. Both models show a similar swirly pattern, and flow instabilities are clearly recognizable. However, the peak values in the bottom-center area of the slices highlighted that the location of the highest tke intensities are shifted compared to the tke of the reference simulation, showing that the LES flow simulations did not perfectly recreate the reference solution. For completeness, the ν_{SGS} and tke in slices A – D are shown in Appendix 4.6, Figure 4.14a and 4.15a, respectively.

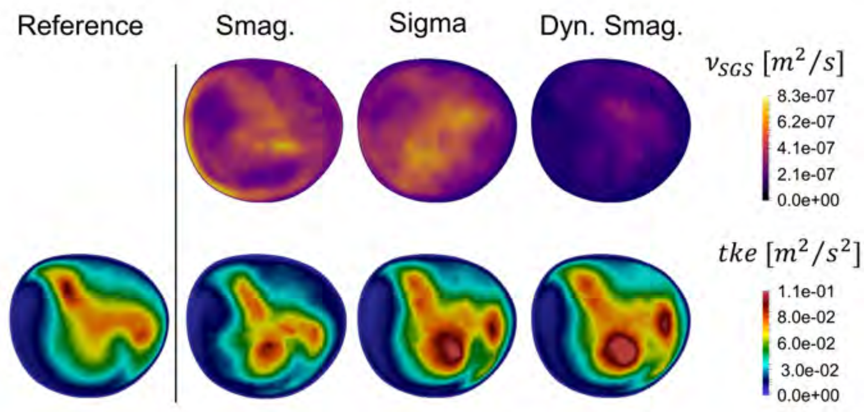

Figure 4.8: Time-averaged SGS viscosity ν_{SGS} (upper panel) and resulting turbulent kinetic energy (bottom panel) for the tested SGS models and compared with the reference solution at slice C. The Smagorinsky model is phenotypically different, both in tke pattern and magnitude. Although more similar, the Sigma and Dynamic Smagorinsky did not produce the same tke patterns.

For a further comparison of the SGS models with the reference solution, the tke values along the horizontal and vertical lines on the A – D slices were reported in Figure 4.9. The Smagorinsky model did not produce a comparable tke on any line. The Sigma and Dynamic Smagorinsky were able to replicate the reference solution on plane A and D but not on B and C, which are the ones more affected by the presence of a stenosis and hence the most relevant for the study of high-frequency flow instabilities. In the near-wall region of plane B, particularly, it is possible to appreciate the different properties of the SGS models. The tke obtained with both Smagorinsky models is importantly affected by the ν_{SGS}. The Sigma model is, on the other hand, far more dissipative, since the D_m of the model proposed by Nicoud et al. (2011) [119] would vanish in case of two-dimensional or two-components flow, and in case of pure rotation or pure shear, and would behave cubicly in the near-wall region.

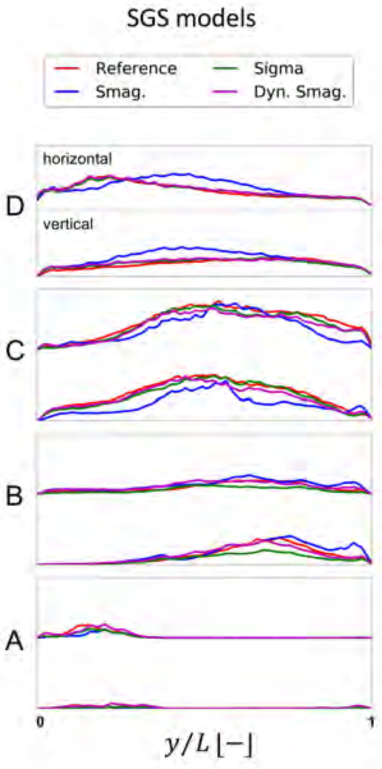

Figure 4.9: Time-averaged *tke* over vertical and horizontal lines on slices A to D for the reference solution and the three SGS models (Smagorinsky, Sigma, Dynamic Smagorinsky).

A visual inspection of the Q criterion (Figure 4.10) confirmed that the post-stenotic jet did not break down as rapidly as the reference solution for any of the tested SGS models.

We also compared the computational cost (CPU hours) of the SGS models, the reference solution, and the 6M simulation without SGS models (Table 4.4). The reference solution (22M – $None$) was 4.60 times more computationally expensive compared to the 6M mesh simulation without any SGS model (6M – $None$), while the Dynamic Smagorinsky and the Sigma models were more expensive than the 6M – $None$. The comparison in computational cost between the Dynamic Smagorinsky and Sigma model is consistent with previous studies [117], [123].

Figure 4.10: Vortexes in the ICA region were identified by means of the Q-criterion. The breakdown location of the jet and the intensity of flow instabilities of all LES simulations differed from the reference solution.

Mesh name	**SGS model**	**CPU h/$6M - None$ CPU h**	**s/timestep**
$22M$	None	4.60	2.43
$6M$	None	1.00	1.58
$6M$	Sigma	1.77	2.80
$6M$	Dynamic Smagorinsky	2.66	4.20

Table 4.4: CPU hours of the reference solution ($22M - None$) and of the most relevant SGS models compared to the $6M - None$ for constant flow rate. There is a marked difference between the $22M$ and the SGS models. The amount of time required to perform each time step Δt highlights remarkable differences between Dynamic Smagorinsky SGS model and $6M - None$.

4.3.3.2 Pulsatile Flow Simulations

The evaluation of the SGS models applied to a pulsatile inflow was performed with Sigma and Dynamic Smagorinsky models. The time-averaged SGS viscosity ν_{SGS} (Figure 4.11 – upper row) was globally higher for the Sigma compared to the Dynamic Smagorinsky model, consistent with the constant peak systolic flow rate simulations.

In the middle row of Figure 4.11 we show tke of the pulsatile simulations, where **u'**(**x**,t) was computed with a constant $\overline{u}$, in slice C for the reference solution, the $6M$ with Sigma model, and $6M$ with Dynamic Smagorinsky model, left to right respectively. Visually, there was a large similarity between the tke fields.

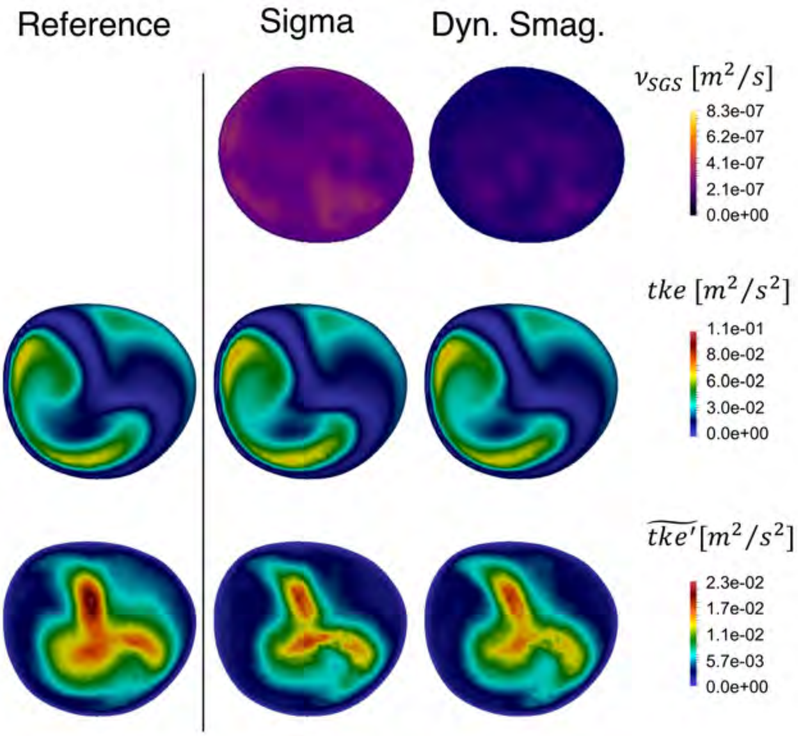

Figure 4.11: Time-averaged added SGS viscosity ν_{SGS} (upper panel), resulting time-averaged tke (middle panel) and its high frequency counterpart tke' (bottom panel) for the tested SGS models and compared with the pulsatile reference solution on slice C. Both tke and tke' are alike for the LES simulations and the reference solution.

The bottom row of Figure 4.11 shows that the tke computed by using high-pass filtered fluctuating velocity components, **u'**(**x**,t), now referred to as tke', is highly comparable. It is hence clear that the LES simulations harbor the same turbulent kinetic energy as the reference solution. The power spectral densities in Appendix 4.7 Figures 4.19, 4.20, 4.21, 4.22 and 4.23, showing no difference in between the LES models and the reference solution, also backed up these results. Of note are also the large differences between the two measures of tke in the pulsatile simulation. The bottom row represents the regions with turbulent kinetic energy with a higher frequency fluctuation than those introduced from the flow waveform at the inlet. In the context of this study, we emphasize these more as the high frequency content of the simulated flow is our quantity of interest. For completeness, the ν_{SGS}, the tke and the tke' in slices A – D are shown in 4.6, Figure 4.14b, 4.15b and 4.16, respectively.

Table 4.5 shows CPU hours computed for the two SGS models, the reference solution, and the 6M mesh without any SGS model applied ($6M - None$) for pulsatile flow simulations. Similar to the constant flow rate simulations, the reference solution ($22M - None$) was more computationally expensive than any other $6M$ simulation, and the LES simulation run with the Dynamic Smagorinsky model was again more expensive than the $6M - None$ and $6M - Sigma$ simulations. Since the computational results of the two SGS models were comparable to the reference solution, the reduction in computational cost favored the Sigma model.

4.4 DISCUSSION

The aim of this study on post-stenotic flow instabilities in a patient-specific model of a stenosed carotid artery, was two-fold: 1) find an adequate underresolved DNS solution from a spatial and temporal refinement study with respect to the turbulent scales, and from a pragmatic biomedical engineering point of view, and 2) assess whether three commonly used SGS models are able to replicate the results from our reference solution for both constant and pulsatile flow rates on a coarser mesh.

Focusing firstly on the spatial and temporal refinement studies, we found a grid spacing of $\Delta x = 1.92 \cdot 10^{-4}$ m and time step size of $\Delta t = 5 \cdot 10^{-5}$ s to be the best tradeoff between computational cost and accuracy from a pragmatic biomedical engineering point of view.

Relative to others, Lancellotti et al. (2017) [124] reported using $\Delta t = 6.25 \cdot 10^{-4}$ s and an "effective" mesh size of $\Delta x = 6.5 \cdot 10^{-5}$ s as a reference solution, i.e., a time step one order of magnitude larger, and a cell size almost three times smaller. Even, with a different working fluid, their Reynolds number was only 25 % smaller at the stenosis. Lee et al (2008), which was the first to perform true DNS in a patient-specific geometry, is not directly comparable with respect to mesh size since they used spectral finite elements, but they

Mesh	**SGS model**	**CPU h/$6M - None$ CPU h**	**s/timestep**
$22M$	None	4.18	3.65
$6M$	None	1.00	2.62
$6M$	Sigma	1.49	3.90
$6M$	Dynamic Smagorinsky	2.53	6.64

Table 4.5: CPU hours of the reference solution ($22M - None$) and of the most relevant SGS models compared to the 6M-None for pulsatile flow rate.

reported a time step of $\Delta t = 1 \cdot 10^{-5}$ seconds, although argued from a numerical stability point of view [9].

Furthermore, we found that simulations on a coarser mesh with SGS models were not able to capture the high-frequency flow features for a constant flow rate equivalent to the peak systolic flow rate ($Re = 1380$). If pulsatile flow was applied ($Re_{average} = 980$, $Re_{max} = 1380$) the SGS models were able to replicate the flow features of the reference solution. The SGS models are thus applicable for investigating the turbulent-like flow in multiple patients or configurations, and ultimately, with fluid structure interaction (FSI), how the flow fluctuations can present as skin vibrations on the neck of affected patients. The discrepancies between constant and pulsatile flow simulations can be attributed to the differences in flow rate, which for the constant flow rate simulation, was higher than the average flow rate for the pulsatile flow rate simulations, although with the same peak flow.

The SGS viscosity of the Sigma model was overall higher than the one resulting from the application of the Dynamic Smagorinsky model, which is the opposite of what Baya Toda et al. (2014) [125] found in their study of an internal combustion engine. In their IC chamber, the viscosity of the Dynamic Smagorinsky model increased when the flow jet impinged a wall, as a consequence of the increase of the strain-rate tensor. On the contrary, the Sigma model did not produce an increased SGS viscosity in that region, as its D_m is not affected by the magnitude of the strain-rate tensor. The different dissipation provided by the two models was, therefore, a direct consequence of the physics of an impinging jet, which are not comparable to the physics of a free jet such as the one considered in this manuscript. We therefore recommend a careful evaluation of the choice of SGS model with respect to the physical problem, keeping in mind that there is a sensitivity which can affect the results.

In our temporal refinement study the most accurate simulation had a time step size one order of magnitude smaller than our reference solution, and we can therefore, with great confidence, say that it was temporally well resolved. However, for the spatial refinement the averaged cell lengths in the finest mesh was only 33 % smaller compared to our reference solution, see 4.1. To further investigate whether the finest mesh could be considered a valid point of reference for the spatial sensitivity study, we used Richardson's extrapolation method [126] defined as in equation 4.5, where $f_{\Delta x_j}$ is the quantity of interest, here a temporal and spatial average of $\mathbf{u}(\mathbf{x},t)$, Δx_j is a measure of grid spacing, c is a constant value obtained from the evaluation of equation 4.5 $f_{\Delta x_j}$ at the two finest meshes ($22M$ and $50M$), p is the measured order of convergence for $f_{\Delta x_j}$, and subscript j is mesh number in the refinement.

$$f_{extrapol.} = f_{\Delta x_j} + c \cdot \Delta x_j^p \tag{4.5}$$

In order to nullify the impact of difference in inlet size, we normalized $\overline{u}$ by the inlet cross sectional area A_j of each mesh (which is different due to different accuracy with which the boundary of the inlet can be replicated). The results of the Richardson's extrapolation are summarized in Table 4.6. The solution was monotonically converging across the three finest grids with an obtained order of convergence $p = 1.34$. Furthermore, the uncertainties on the finest grid and on the second finest grid were not greater than 10 % even with a security factor of 1.5 [127], and could therefore be considered converged with respect to the mean flow features.

Number of Elements	$\overline{\mathbf{u}}(m/s)$	$A(m^2)$	$f(m^3/3)$	**% Error**
$6M$	$2.2265 \cdot 10^{-1}$	$1.8289 \cdot 10^{-4}$	$4.1426 \cdot 10^{-4}$	8.19
$22M$	$2.3295 \cdot 10^{-1}$	$1.7165 \cdot 10^{-4}$	$3.9989 \cdot 10^{-4}$	4.44
$50M$	$2.3636 \cdot 10^{-1}$	$1.6691 \cdot 10^{-4}$	$3.9453 \cdot 10^{-4}$	3.04
Richardson extrpolation	-	-	$3.8290 \cdot 10^{-4}$	0.00

Table 4.6: Space and cycle-averaged velocity compared and extrapolated with Richardson's extrapolation method for different grid sizes.

Although the mean flow was converged, the question remains if the flow was well resolved at the smallest scales. We previously discussed this in Mancini et al. (2017) [128], where we computed the Kolmogorov length scale (μ) [129]. We computed the ratio of the local cell length, Δx, and the Kolmogorov length scale, (μ), in each cell, and reported the temporal and spatial global maximum. The ratio on the two finest meshes were below 10, typically sufficient to capture > 95 % of the dissipation [82]. However, considering the temporal averaged ratio in the post-stenotic region, we obtained a mean/max of 0.347/1.11, and 0.463/1.755 for the $22M$ and $50M$ simulation, respectively, showing that the flow is well-resolved. We also obtained equal results from computing l^+, a surrogate measure for the Kolmogorov length scale compared to the local cell length [130], with $l^+_{max} = 6.2$ located along the wall in the stenosis. Performing a true DNS simulation would require building a mesh with cell lengths of roughly seven times smaller than the finest mesh, yielding mesh consisting of roughly 21 billion cells and thus requiring an enormous amount of computational resources while, from a pragmatic biomedical engineering point of view, having no added value. That being said, using an adaptive mesh strategy would yield a DNS simulation with a smaller mesh, however our local refinement approach is simple to adapt, and the local refinement is consistent between spatial refinement levels. It is also noteworthy that the homogeneous isotropic assumption of the Kolmogorov hypothesis was not met in our simulations. The Kolmogorov hypothesis therefore underestimates the smallest scales, and the simulation might therefore be even more well resolved than the Kolmogorov length scale indicates. Please refer to Figure 4.17 in Appendix 4.6 for a visual comparison of the $l+$ for the 2M, 6M, 22M, 6M Sigma and 6M Dynamic Smagorinsky simulations.

Based on our numerical investigations, we have a high level of confidence in our numerical results, but how do the results compare to flow in-vivo?

Firstly, we assumed a Newtonian fluid with properties mimicking water. With realistic flow rates, the Reynolds number was hence 3.3 times larger compared to in-vivo blood flow, since blood has a higher kinematic viscosity compared to water. As a result, the intensity of the post-stenotic turbulent-like flow is higher in our numerical experiments than what can be expected in-vivo. The spatial and temporal resolutions of this study still hold for physiological realistic situations, in terms of being well-resolved. On the other hand, the use of water also allows for valuable comparison with *in-vitro* experiments, in which water is often used instead of glycerin-based blood-mimicking fluids. Moreover, the relative effect of assuming a non-Newtonian fluid has shown to be small in the carotid bifurcation since, due to the high shear rates in the carotid bifurcation, the non-Newtonian models work in a regime where the viscosity is close to a constant value [131]. Furthermore, compared to other uncertainties like modeling choices and segmentation, the assumption of a Newtonian fluid is marginal. Moreover, from a physical point of view, blood is more complex than just being a non-Newtonian fluid, it is also multiphase flow. The presence of small particles, to mimic red blood cells, has been found to dampen flow instabilities [132], but should not phenotypically change the flow.

Secondly, we modeled the walls as rigid, but they are naturally compliant. Modeling the stenosis with compliant models might dampen some of the unstable flow features. However, determining the material properties of the stenosed region are therefore challenging, since it consists of both plaque and lipid pools. The former is stiffer than a healthy vessel wall, while the latter is more compliant. Therefore, anticipating how this might affect the results is challenging. Moreover, the soft tissue embedding the carotid arteries would further dampen the instabilities that would present on the skin surface, generally with a lower amplitude relative to the fluctuations induced by the turbulent-like post-stenotic flow [133].

In total, the simulation results cannot directly be translated into an in-vivo situation, but is an important first step towards a trustworthy patient-specific flow simulation for investigating the high-frequency flow fluctuations. Future efforts will be directed towards validating the flow with *in-vitro* experiments, and using an FSI approach, i.e., incorporating the effect of compliant walls, which is well-known to better mimic physiological conditions [134].
To ease comparison with other solvers, increase reproducibility, and promote openness in science, we also provide an additional repository [135] with our problem file for the Oasis solver, the used meshes, and averaged results from the reference solution with constant flow rate. The results from this study can therefore easily be compared to other solvers, and potentially ease the amount of work needed to show that a given solution strategy is adequate for investigating turbulent-like flow features for a post-stenotic flow.

In our line of research we are interested in the high-frequency flow features, however a plurality of studies using CFD to investigate flow in the carotid bifurcation are interested in (time-averaged) wall share stress (WSS), or other WSS-derived quantities [102], [109], [110]. We have not investigated whether a coarser mesh would be sufficient for investigating WSS, and furthermore, how LES models would affect the results. For comparison, Valen-Sendstad et al. (2014) found that time-averaged wall shear stress (WSS) was relatively insensitive to the applied computational solution strategy, whereas the OSI, more sensitive to flow fluctuations, changed significantly [110]. We therefore caution readers about extrapolating our results to studies investigating WSS-derived quantities.

Lancellotti et al. (2017) [124] investigated the applicability of LES models in pulsatile simulations of a stenosed patient-specific carotid bifurcation. They, like us, found a static Sigma model to perform best. Although we agree with most of their conclusions, there are some caveats of the study, i.e., they used a streamline upwind/Petrov-Galerkin pressure stabilized Petrov-Galerkin formulation for the reference solution, known to add numerical diffusion [136], which would not be equal between the two meshes. Furthermore, their high Reynolds number at the stenosis is $Re_{stenosis} = 6687$ (computed from values reported in the paper), which is significantly much higher than the $Re_{stenosis} = 2528$ in this study, and might not be relevant in a clinical setting. Despite these limitations, we can conclude that both Lancellotti et al. (2017) [124] and the current study could be used as points of reference for LES modeling and spatial and temporal refinement when investigating flow in the carotid bifurcation: in particular, Lancellotti et al (2017) [124] for WSS and the current study for the high frequent flow features.

We can thus state that future studies investigating the high-frequency features of post-stenotic flow can use an equivalent spatial and temporal resolution reported here, with a Sigma SGS model. Of note is that if a higher Reynolds number is applied, like in the constant flow rate simulations presented here, the turbulence models were not applicable at reported spatial resolution. More specifically, we will use these results to investigate the possibility to diagnose carotid stenosis based on the amplitude of the unstable flow's frequency content by measuring the neck skin vibrations.

4.5 CONCLUSIONS

The numerical methodology applied in this study allowed us to properly resolve the flow field of a stenosed patient-specific carotid bifurcation and hence detect instabilities induced by the stenosis. When compared to the *reference solution*, only Sigma and Dynamic Smagorinsky were able to replicate the averaged mean flow features from the constant flow rate simulation, and the turbulent flow features in the pulsatile flow rate simulations. The computational cost was lower for the Sigma model, and therefore the best choice balancing accuracy with computational cost for studying high frequency flow instabilities. However, for higher Reynolds numbers, similar to the constant flow rate simulation, the LES models were not sufficient. Future efforts on this subject should be conducted with the abovementioned SGS model, while taking advantage of a robust high-order numerical solver such as the one used in this study.

4.6 APPENDIX A

In this section, the time-average of the most relevant parameters, i.e. turbulent kinetic energy (tke), subgrid-scale viscosity (ν_{SGS}) and high-pass filtered tke (tke') if applicable, are depicted for each simulation on the slices of interest (A to D). Specifically, tke is reported for the mesh and temporal sensitivity analysis in Figure 4.12 and 4.13, respectively, while ν_{SGS}, tke and tke' are shown in Figures 4.14, 4.15 and 4.16 for the LES simulations. The dimensionless $l+$ is reported in Figure 4.17.

4.6.1 Mesh sensitivity analysis

Time-averaged turbulent kinetic energy (tke) contours for the available meshes (see Figure 4.12). The contours were not produced for the finest mesh because the expected redundancy did not justify the extremely high investment in computational resources. These simulations were run with a time step of $\Delta t = 5 \cdot 10^{-5} s$, without any SGS model.

4.6.2 Time step sensitivity analysis

Time-averaged tke contours for simulated time steps on the $22M$ mesh (see Figure 4.13). The contours for the finest time step ($\Delta t = 5 \cdot 10^{-6}$ s) were not produced because the expected redundancy did not compensate the investment of the several CPU hours required.

4.6.3 Sub grid scale models

Time-averaged sub grid scale viscosity (ν_{SGS}) for the three tested SGS models with constant and pulsatile flow (see Figure 4.14). These simulations were run on the $6M$ mesh and $\Delta t = 5 \cdot 10^{-5}$ seconds. The resulting time-averaged tke fields for constant, pulsatile flow rates and pulsatile flow rates are reported in Figure 4.15. The resulting time-averaged turbulent kinetic energy fields for constant, pulsatile flow rates and pulsatile flow rates with high pass filter applied tke' are reported in Figure 4.16.

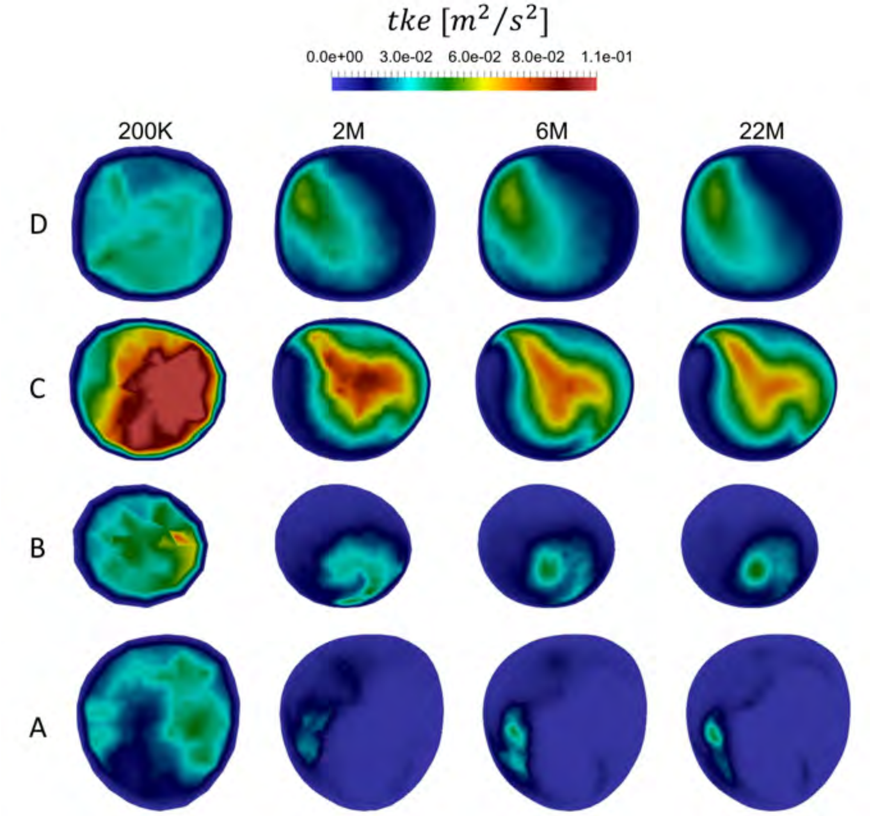

Figure 4.12: Comparison of several mesh densities, based on qualitative analysis of the time-averaged turbulent kinetic energy distribution over several slices (A, B, C, D) along the ICA.

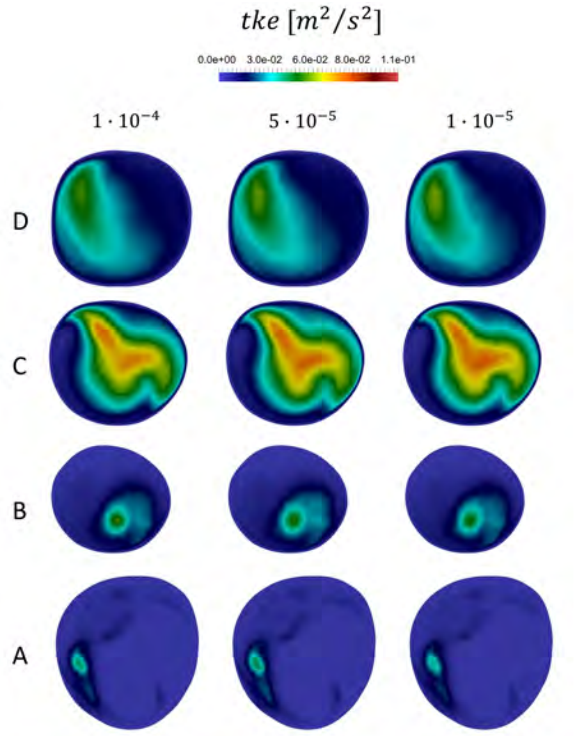

Figure 4.13: Comparison of the time-averaged turbulent kinetic energy field on the depicted slices for several temporal resolutions used in this study.

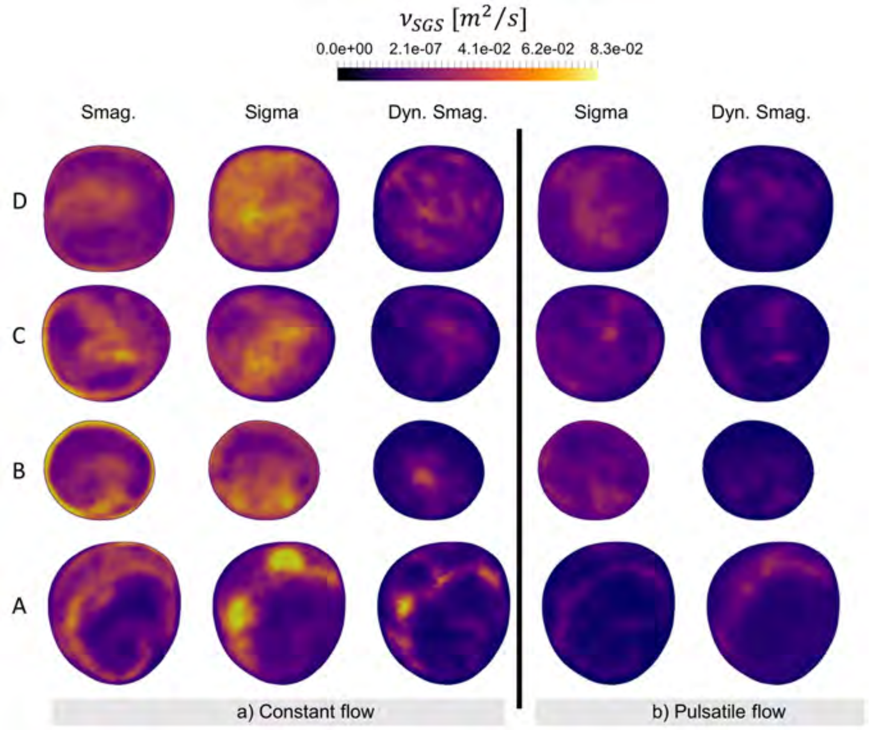

Figure 4.14: Comparison of sub-grid scale viscosity for the LES simulations used in this study on the 6M mesh with $\Delta t = 5 \cdot 10^{-5}$ seconds, with constant flow rate (Re = 1380) on the left hand side (a) and pulsatile flow rate ($Re_{average}$ = 980, Re_{max} = 1380) on the right hand side (b).

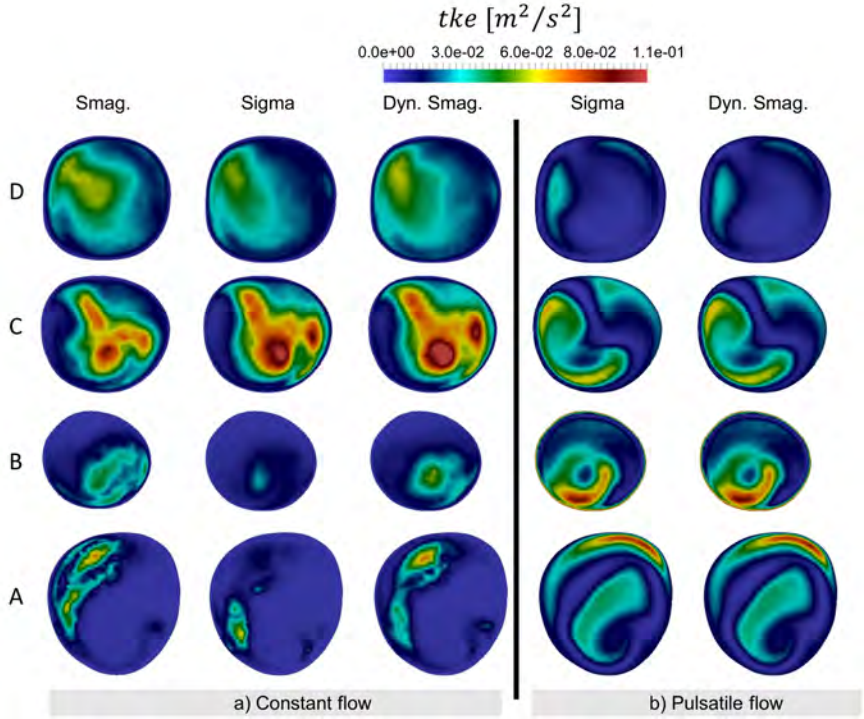

Figure 4.15: Comparison of the time-averaged turbulent kinetic energy field resulted from applying the sub-grid scale models in the LES simulations, for constant (a) and pulsatile (b) flow rate.

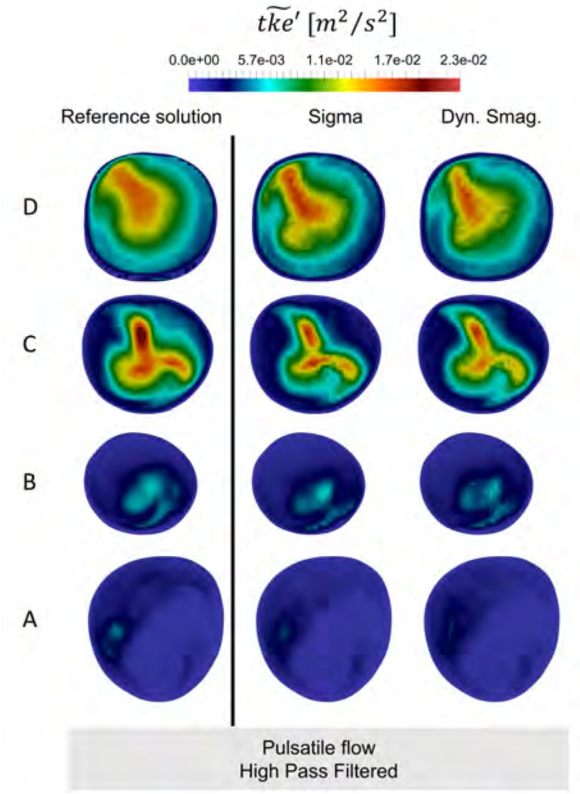

Figure 4.16: Comparison of the time-averaged high-pass filtered turbulent kinetic energy field for pulsatile simulations. The tke' for the reference solution simulation (22$MNone$) is reported on the left hand side, while the tke' for the most relevant LES simulations (Sigma model and Dynamic Smagorinsky model) are depicted in the right hand side.

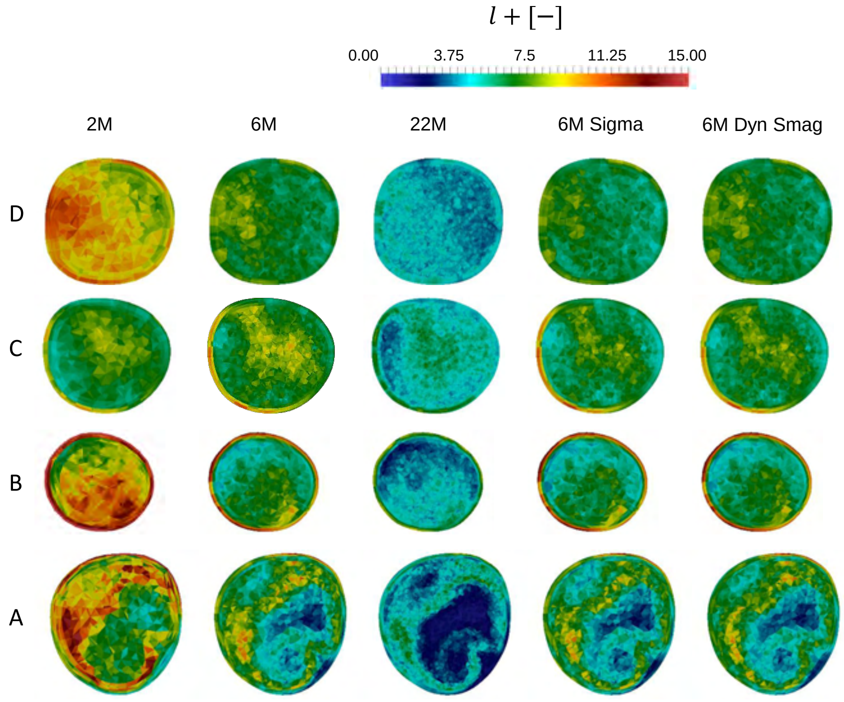

Figure 4.17: Comparison of several mesh densities and SGS models, based on qualitative analysis of the dimensioneless cell size $l+$ over several slices (A, B, C, D) along the ICA for constant flow rate simulations.

4.7 Appendix B

In this section, the power spectral densities (PSD) at several centerline points in our model (see Figure 4.18) are depicted in Figures 4.19, 4.20, 4.21, 4.22 and 4.23 for spatial (a) and temporal refinement studies (b), for LES simulations with constant (c) and pulsatile (d) flow rate.

Figure 4.18: Centerline locations where the PSD of the velocity traces was computed and whose plots are reported in the following paragraphs of this Appendix.

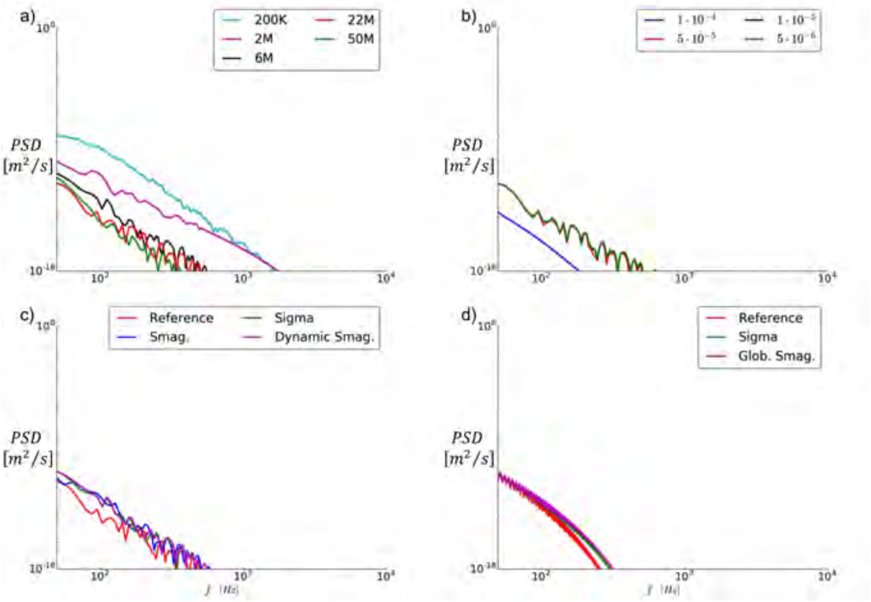

Figure 4.19: PSD of the velocity obtained by probing on a point located 3.6 diameters upstream of the stenosis on the centerline of the model, showing that the flow is laminar before the carotid bifurcation.

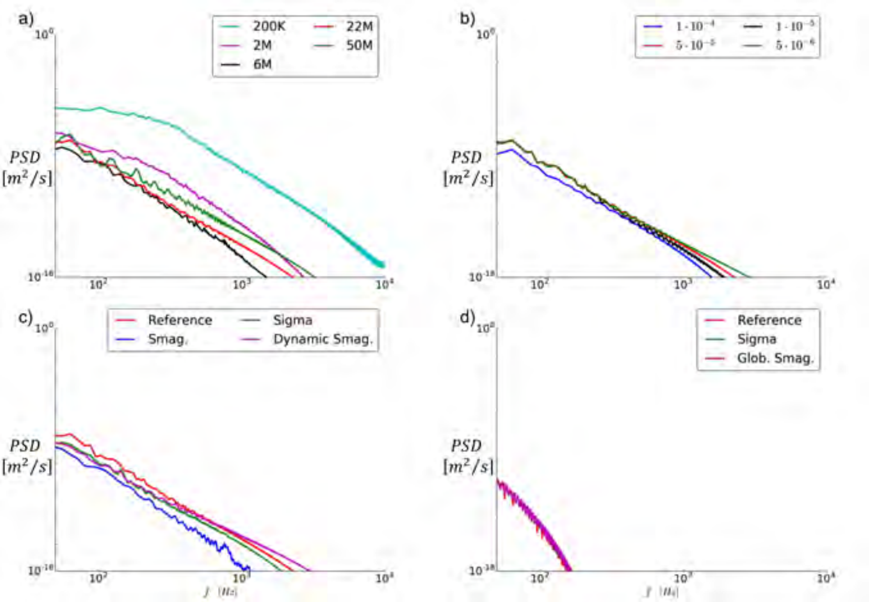

Figure 4.20: PSD of the velocity obtained by probing on a point located 1.4 diameters upstream of the stenosis on the centerline of the model, after the carotid bifurcation, but before the stenosis, showing that for the constant flow rate simulations the flow instabilities have grown.

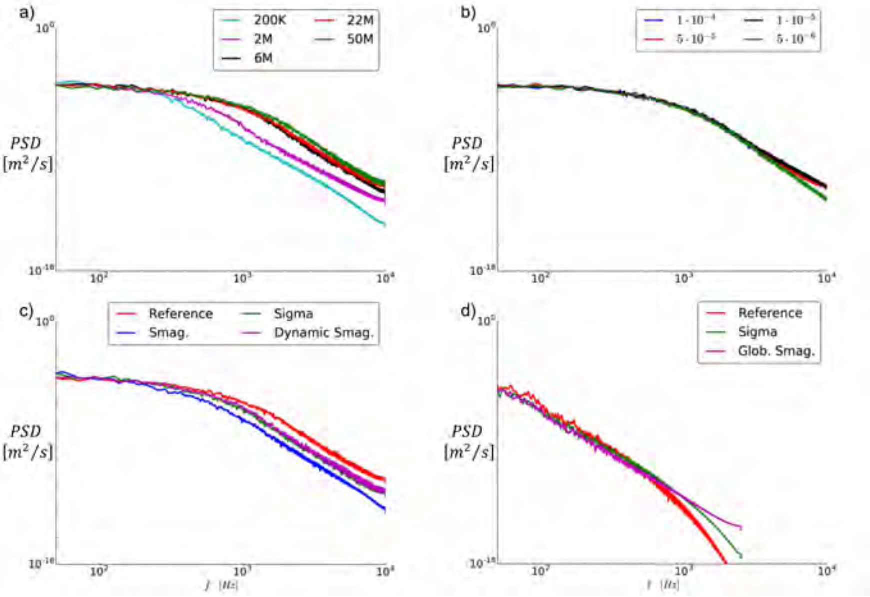

Figure 4.21: PSD of the velocity obtained by probing on a point located 0.6 diameters downstream of the stenosis on the centerline of the model, showing that the flow is highly unstable and that the jet has already broken down.

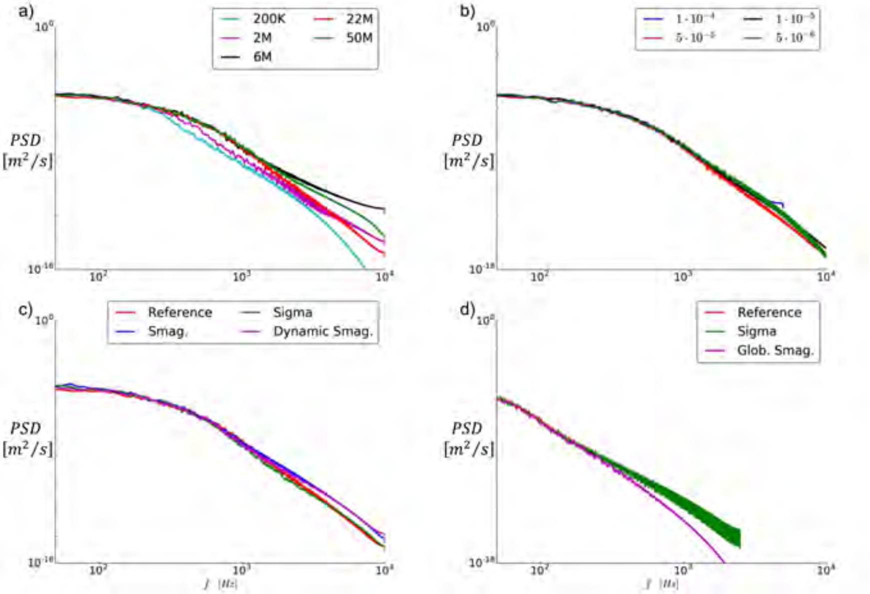

Figure 4.22: PSD of the velocity obtained by probing on a point located 2.6 diameters downstream of the stenosis on the centerline of the model, showing that the energy has decreased in the high-frequency region of the flow, and that the flow is starting to relaminarize.

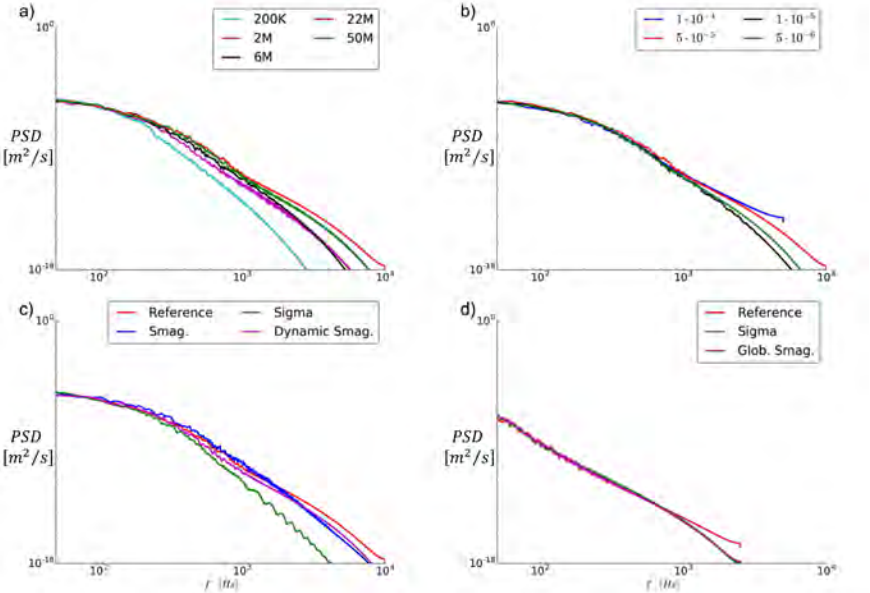

Figure 4.23: PSD of the velocity obtained by probing on a point located 4.6 diameters downstream of the stenosis on the centerline of the model.

CHAPTER 5

LASER DOPPLER VIBROMETRY: A FEASIBILITY IN-VITRO STUDY

This chapter introduces an experimental methodology concerned with proving the ability of laser Doppler vibrometry to measure intra-arterial flow features and, by extent, the stenosis-induced flow instabilities. Specifically, this chapter focuses on assessing the frequency-based sensitivity of the device to changes in physiologically varying flow rates. It is based on the paper "Detecting Carotid Stenosis from Skin Vibrations using Laser Doppler Vibrometry – an *in-vitro* proof-of-concept.", *PLoS ONE*, vol. 14, no. 6, pp. 1-17, 2019 [103].

5.1 INTRODUCTION

Stroke, a cardiovascular disease (CVD), is the second most common single cause of death in Europe [137]. There are many underlying causes of stroke, but one of the most prominent is carotid stenosis [2], as the atherosclerotic plaque causing the narrowing might rupture and the thrombi would obstruct the blood flow in downstream vessels. Unfortunately, few patients with carotid stenosis present symptoms in the early stages of the disease. Moderate and severe asymptomatic stenosis affect 12.5 % and 3.1 % of the over 70 population, respectively [106], [138]. However, asymptomatic stenosis is not commonly diagnosed unless associated with other CVDs [4] such as coronary stenosis and hypertension, or risk factors such as diabetes [5], [6].

Thus, the possibility of assessing and stratifying the risk of future stroke in asymptomatic patients with carotid stenosis is limited [3].

The presence of turbulence in stenosed carotid arteries has been established in numerous studies, see for example the results reported by Beach et al. [10] using ultrasonic duplex Doppler velocimetry in-vivo, by Giddens et al. [11] *in-vitro*, and by Lee et al. [9] and by Varghese et al. [12] by means of a computational fluid dynamics (CFD) approach. This turbulence may produce audible bruits induced by flow instabilities distal to the stenosis and carotid auscultation is currently used in clinical practice to detect carotid bruits. Although this is usually considered as an adequate screening test [3], it has a low-sensitivity [7], it is operator-dependent, and it is a subjective measurement that may be confounded by background noise [108]. Furthermore, carotid ultrasound, which is routinely used for stenosis diagnosis in hospitals, is too expensive and complex for use in first line screening.

Laser Doppler Vibrometry (LDV) has been shown to be particularly suitable for detecting physiological signals from skin level movements, for measurement of pulse wave velocity [16], breathing [17], or heart rate [18]. Within the context of an H2020 funded project (CARDIS), we have developed a compact multi-beam array prototype LDV system [19] based on optical chip technology [20] and suitable for use in a clinical setting for, among other things, measurement of arterial stiffness. Hypothesizing that post stenotic flow instabilities impart energy to the arterial wall, giving rise to mechanical waves which propagate through the soft tissues up to the skin, there is a potential use of LDV for the detection of stenosis in superficial arteries. The intended use for such device would be first line cardiovascular screening, identifying individuals at risk so that they can be referred to specialized centers for further follow-up using dedicated and established diagnostic techniques such as ultrasound or Magnetic Resonance Imaging.

The objective of the current work was therefore to provide a proof of principle concerning the ability of LDV to infer the presence of carotid stenosis. Specifically, we aimed to determine whether the presence of a stenosis leads to high frequency fluctuations in the recorded LDV signals and, if so, to assess the frequency range where such fluctuations would have to be sought. To do this, we performed hydraulic bench tests on a model of a patient-specific carotid bifurcation manufactured in two materials having different stiffness (referred to as compliant and stiff). The main purpose of the compliant model was to provide a physiologically plausible hemodynamic environment, allowing us to make a meaningful comparison between our findings and in-vivo data. The compliant and stiff models were subjected to pulsatile flow over a wide range of velocities. A catheter-tipped manometer was used as a reference for the LDV recordings. A frequency domain analysis of the signals was then performed to assess the impact of material stiffness and measurement location on the distribution of the energy content in the useful frequency range and multivariate linear regression analysis was used to determine the relative contribution of these factors to the relationship between volume flow rate and signal strength.

5.2 MATERIALS AND METHODS

5.2.1 Model reconstruction

Images of the common carotid bifurcation with severe internal carotid artery (ICA) stenosis of a 75 year old man were obtained by computed tomographic angiography, the patient having provided informed consent for the processing and further use of the data. The images were segmented by means of 3D Slicer [115], to obtain an accurate model of the vasculature (Figure 5.1A). The degree of stenosis of the carotid model was 76 % as calculated by the *North American Symptomatic Carotid Endarterectomy Trial* method [139], where $A_{stenosis} = 5.57mm^2$ and the ICA area downstream of the stenosis was $A_{downstream} = 23.14mm^2$.

A compliant model of the carotid bifurcation was created in silicone rubber, as follows. A brittle inner mold of the bifurcation was 3D printed in VisiJet-pXL and sprayed with a finishing ColorBond (3D System, SUA) bonding layer (TRIAXIS, Belgium) in order to smooth the inner surface of the model. In our laboratory, liquid silicone (Xiameter rtv-481, De Gouden Pluim, Belgium) was poured around the mold and allowed to dry for 24 hours. The pouring was repeated until the model was thick enough to be handled; three layers being found sufficient. The inner mold was crushed and the bonding layer allowed an easier extraction of the crumbled pieces. Tensile tests were performed on samples the thickness of which was comparable with that of the carotid model (1.5 mm), and they revealed a Young modulus (E) of 300±2kPa. The silicone model was then mounted in an open-topped Perspex box and surrounded by an aqueous hydrogel (Aquasonic 100, Parker Labs, USA) to mimic the neck's soft tissues (see 5.1B). A skin-like layer (polyurethane foil, Platilon, Epurex Films, Germany) was then applied over the gel surface. To ensure adequate reflection of the laser light [20], small patches of retro-reflective tape (3M Scotchlite High Gain Reflective Sheeting 7610, USA) were attached to the skin layer.

A second model with the same arterial lumen geometry was then 3D printed in a stiff transparent and water-resistant material (TuskXC2700T, Materialise, Belgium; E = 2700 MPa (manufacturer data)), Figure 5.1C. The stiff model was used to provide data for a computational fluid dynamical model, described in [101], in which the presence of the gel was not taken into account. The small patches of retro-reflective tape were attached directly to the outer surface, omitting the use of the gel.

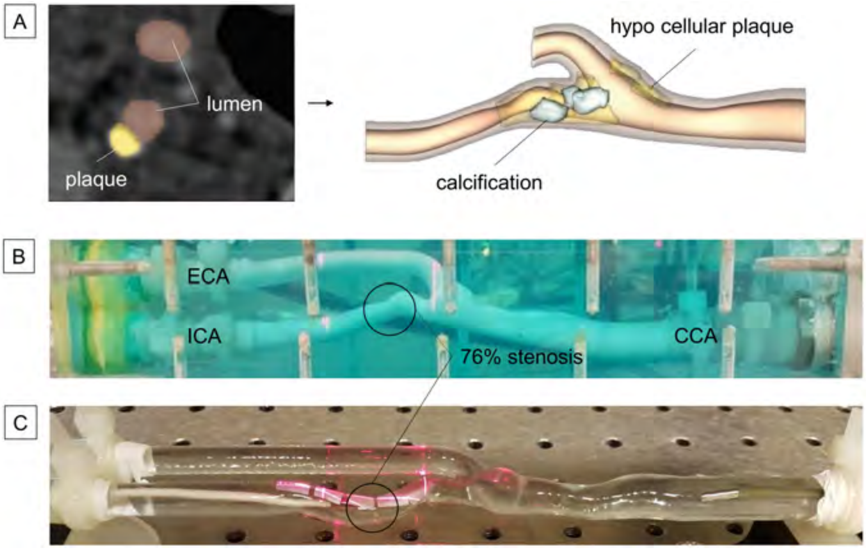

Figure 5.1: (A) Computed Tomography Angiography images of the carotid bifurcation from a 75 year old male were processed by Iannaccone et al. [115] in order to obtain a patient-specific model of the plaque-free stenosed vessel. The compliant (B) and stiff (C) models used for the hydraulic tests replicate the geometry of the patient-specific common carotid artery (CCA), external carotid artery (ECA), and internal carotid artery (ICA) where the 76 % area stenosis (circled) is located.

5.2.2 Experimental set-up

A prototype multi-beam LDV [21] was used for all recordings. The device was designed with two parallel beam rows spaced 2.5, 3.5 or 5 cm, configurable during assembly. Each row consisted of six beam points, spaced 5 mm from each other. The laser wavelength was measured to be 1550 ± 2 nm. The temporal resolution was 10 µs at a sample rate of 100 kHz. The maximum measurable velocity was higher than 50 m/s and the displacement resolution was less than 10 nm. A calibration measurement between DC and 1 kHz showed that the frequency response of the LDV was flat in this frequency range. In the recordings described here, only two beams were used. The LDV was mounted on a tripod and the models were mounted on a stabilized optical table and connected to a perfusion loop as shown in Figure 5.2A.
A schematic representation of the hydraulic setup is shown in Figure 5.2B. The loop was composed of a continuous flow pump (P1) and a pulsatile counterpart (P2), a Windkessel chamber (W), and two reservoirs (R1, R2). P1, a rotary pump (Gear Pump Head V108.05R Ryton Gears, Verder NV, Belgium), provided continuous flow, whose magnitude was controlled by varying the supply voltage, while P2, a custom-built programmable piston pump (HT Denyer, Consulting Engineer, UK), provided pulsatile flow. The speed and

stroke of the piston and the opening and closing time of "mitral" and "aortic" valves were set by means of in-house software (HPUMP Controller v0.4b). The pumps could be controlled independently and could therefore run simultaneously or individually. Both pumps supplied flow to the Windkessel chamber which, in the case of pulsatile flow, would then deliver a dampened flow waveform to the common carotid artery (CCA) of the mounted model. A cannulating ultrasonic flow probe (ME 5PXN, Transonic Systems Inc., USA) was installed between W and the model. A catheter tip manometer (D.CTC/6F-1, Gaeltec Devices Ltd, UK) was passed into the CCA with the tip located 6.5 cm upstream of the center of the stenosis. A second, smaller, manometer (12-CTC/4F-1, Gaeltec Devices Ltd, UK) was passed into the ICA and positioned at one of four locations downstream from the center of the stenosis. The first location was one CCA diameter (0.8 cm) downstream and each of the following locations was an additional CCA diameter downstream of its predecessor. The four locations are, from here on, referred to as 1D, 2D, 3D and 4D. The downstream beam of the LDV was moved horizontally together with the small manometer to record, respectively, skin displacement and intra-arterial pressure at the same horizontal location. The upstream LDV beam recorded vibrations 3.5cm upstream of the small pressure probe. The flow rate through the ICA and external carotid artery (ECA) branches was controlled by increasing or decreasing the resistances in the lines connecting each of the branches to the downstream reservoir R1, the purpose of which was to provide a constant back-pressure to the model. A second ultrasound-based flow probe (ME 4PXN , Transonic Systems Inc., USA) was installed downstream of the model, in the line connecting the ECA to R1. The water was then collected in the further downstream reservoir R2, which then supplied fluid for both pumps P1 and P2. The pipes connecting the elements of the loop were of compliant material (silicone rubber SL601).

5.2.3 Flow conditions

P1 and P2 could be combined and their output adjusted to match physiological conditions [140], [141]. We aimed for a physiological mean flow rate of 337 ml/min and four other flow rates corresponding to the mean value plus and minus one and two standard deviations (SD), as derived from the data in [140], giving values of 433, 241 (± 1 SD) and 529 and 145 (± 2 SD) ml/min. The flow split was set to mimic physiological conditions as well [118], where we aimed for default values of 55 % to the ECA and 45 % to the ICA. We then varied the ICA flow split within the range 0.45 ± 0.13. The flow split values were set when Q_{CCA} = 337 ml/min, but they did not change greatly when the Q_{CCA} changed. This standard setting resulted in a pulse pressure (PP) of about 19 mmHg for a heart rate of 60 beats/minute. Additional experiments were then performed to enforce a PP_{CCA} of 40 mmHg, which could only be

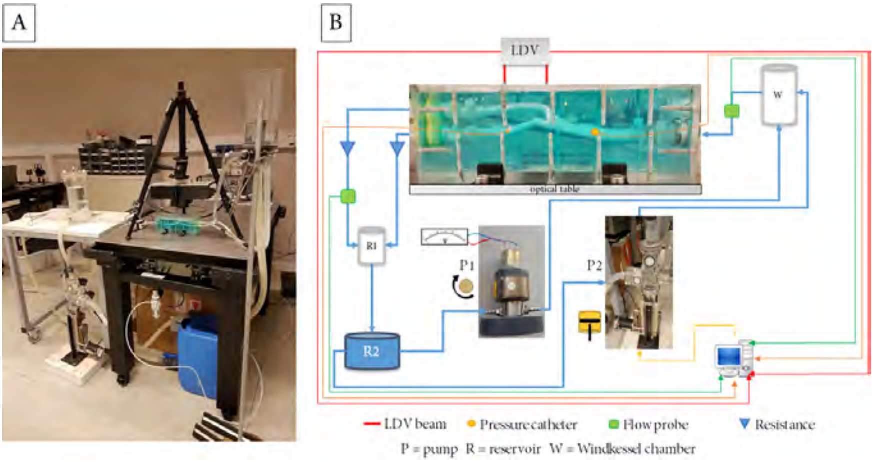

Figure 5.2: (A) The model was secured to an optical table in order to minimize the influence of external movements. (B) In this layout of the test rig, the flow is depicted as a blue line where the arrow represents the direction of the flow. The thinner red, orange and green lines represent the signal acquisition wires of the LDV, pressure probes and flow probes, respectively. This set-up was used for both the compliant and stiff models.

achieved with supra-physiological flow levels (around 650 ml/min). As the stiff model was able to sustain higher pressures, we tested flow rates up to 1465 ml/min for that model. In all, the test conditions span a wide range of flow levels, encompassing the physiological range, both below and above levels expected to trigger flow instabilities. Additionally, the pressure catheters were, from time to time, removed from the main loop in order to test the impact of their presence on the flow.

The signals, recorded by the six probes (two LDV beams, two pressure probes and two flow probes), were acquired by means of Powerlab-16/35 (AD Instruments, Oxford, UK) at a sampling frequency of 20 kHz. Once the system provided stable fluid dynamic conditions, data were recorded for at least 10 seconds and saved via dedicated software (LabChart Pro-v8). Some representative signals are shown in Figure 5.3. The left panel of Figure 5.3 depicts the waveforms of Q_{CCA}, pressure at the ICA (P_{ICA}) and LDV at the same horizontal location as the tip of the manometer (LDV_{ICA}) for physiological mean flow rate and flow split settings, (i.e. Q_{ICA}/Q_{CCA} = 45 %), for both the compliant (upper left) and stiff (lower left) models. While the shape of the flow waveforms differs only in the presence or absence of the dicrotic notch, the shapes of the pressure and LDV signals in the two models differ drastically. Note the small amplitude of the LDV signal when compared to that measured in the compliant model. The same considerations can be applied to the waveforms obtained by setting Q_{CCA} > 700 ml/min, as shown in the upper right and bottom right panel of Figure 5.3 for the compliant and stiff models, respectively. When increasing the flow rate, however, the waveform shapes differ as well. Moreover, the high-frequency content of the pressure signal P_{ICA} is more evident.

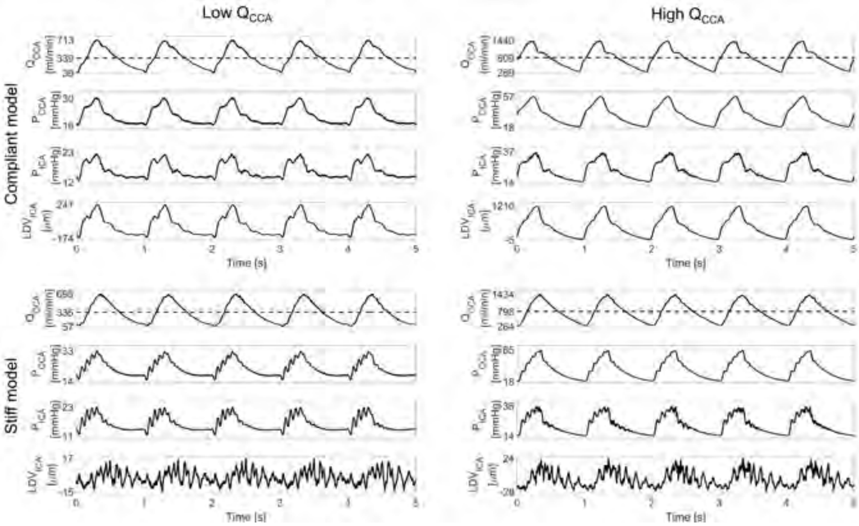

Figure 5.3: Recorded time traces for the compliant (upper panels) and stiff (bottom panels) models obtained at 1D with low (left panels) and high (right panels) Q_{CCA}. The horizontal dashed line shows the mean Q_{CCA}.

5.2.4 Signal Processing

5.2.4.1 *Power Spectral Density*

Frequency spectra of the recorded data, obtained by the fast Fourier transform (FFT), were computed using LabChart Pro-v8. 8K points were used for the FFT with 50 % overlap and Hann windowing [142]. The spectrograms were calculated by means of the same software with 1K points, Hann windowing with 93 % overlap. The Power Spectral Density (PSD) represents the amount of energy present in the analyzed signals at each point in the frequency domain [121]. We calculated the PSDs with reference to an attenuation value of 0.001 units for all measurements, and it is hence expressed in decibels (dB). The spectra were then imported to Excel (Microsoft, 2016) for further processing. Figure 5.4 shows the processing steps for the P_{ICA} signal shown in the upper left corner of Figure 5.3 (mean Q_{ICA} = 154 ml/min). The spectrum of the P_{ICA} (Figure 5.4A, upper panel) is shown against that of the no-flow condition in the available frequency range (hence 10 kHz, based on a sampling frequency of 20 kHz). The intense 3500 Hz and 7500 Hz peaks were present in the spectra of both the no-flow and the Q_{ICA} = 154 ml/min signals. The subtraction of no-flow spectra made it possible to reduce the noise component of the Q_{ICA} = 154 ml/min pressure spectrum, as shown in the bottom of panel A. The absolute value of the normalized Q_{ICA} = 154 ml/min spectra was shifted by the value of the no-flow one, from an average of -30 dB to 0 dB. All the signals were processed with this method, hence the shifting was applied to all the spectra. To quantify the energy within defined frequency bands, we calculated the integral of the normalized spectra in the 0-500 Hz range by means of the trapezoidal method. The I_n integrals were grouped in $\Delta f = 50Hz$ swide frequency intervals and their sum was calculated as in 5.1.

$$S_{n:n+\Delta f} = \Sigma_{f=n}^{n+\Delta f} I_f \tag{5.1}$$

The integral calculation of the normalized Q_{ICA} = 154 ml/min and Q_{ICA} = 394 ml/min (matching with signal P_{ICA} of Figure 5.3 upper right) spectra is shown in Figure 5.4B. The same workflow was applied to all available recordings, for both pressure and LDV in the ICA.

5.2.5 Statistical analysis

To assess the ability of LDV to recognize different flow levels with different materials, pump settings and probe locations, and hence to assess the frequency band where the spectra are most sensitive to the change in flow rate, further statistical analysis was necessary. We therefore constructed a univariate linear model in IBM SPSS Statistics 25, with the integrals of the 50 Hz wide normalized spectra intervals, with downstream P_{ICA} and LDV_{ICA} signals, as dependent variables. Q_{ICA} was used as a covariate and the frequency range as a fixed factor (0 = 0-50 Hz, 1 = 50-100 Hz, ..., 9 = 450-500 Hz). Additionally, location (1D = 1, 2D = 2, 3D = 3 or 4D = 4), material (compliant = 1 or stiff = 0) and the impact of the presence of the intra-arterial pressure probe on the flow field (present = 1, not present = 0) were used as fixed factors. As we wished to study the extent to which an increase in flow increases the power within a certain frequency band, we also added the interaction term, $Freq \cdot Q_{ICA}$, to the model. The resulting univariate model to evaluate the area under the curve (AUC) is expressed in equation 5.2.

$$\begin{aligned} AUC = constant + A \cdot Freq + B \cdot Location + C \cdot Material + \\ + D \cdot Probes + E \cdot Q_{ICA} + F \cdot Freq \cdot Q_{ICA} \end{aligned} \tag{5.2}$$

The estimated F coefficient was used as measure of sensitivity, since it reflects the slope of the regression equation for predicting the dependent variable from the independent one. P-values $p < 0.01$ were considered

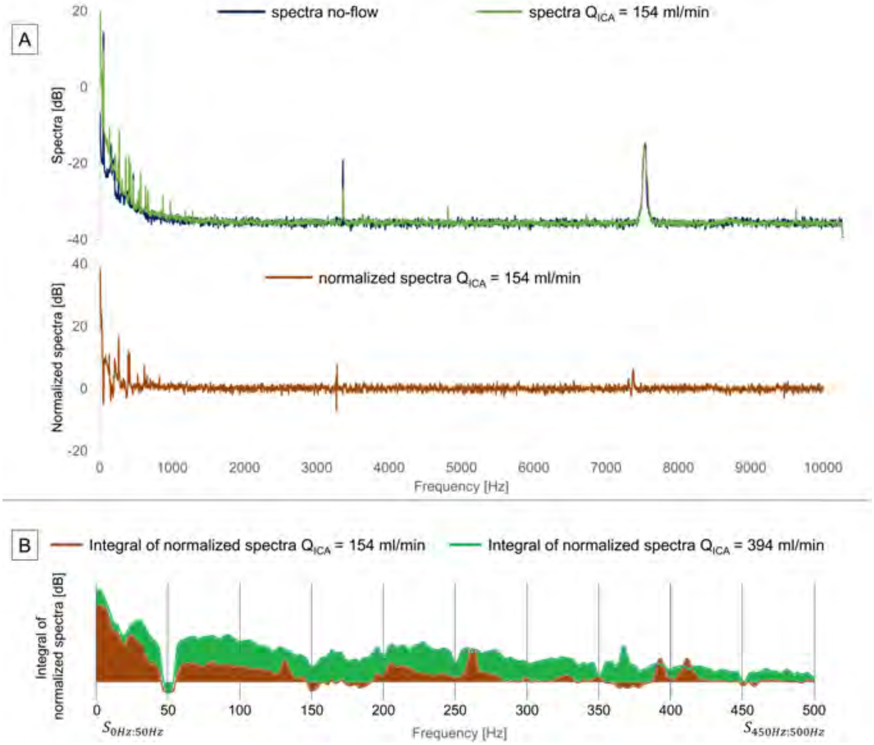

Figure 5.4: (A) The spectrum of the no-flow pressure signals was subtracted from the spectrum of each flow recording to obtain the normalized spectrum, (B) its integral was obtained applying the trapezoidal method at 50 Hz-wide frequency ranges. The same post processing was applied to all available recordings.

significant.

Additionally, the Estimated Marginal Means (EMMs) were computed for both P_{ICA} and LDV_{ICA} in the 0-500 Hz range. The EMMs are the variable's means adjusted for the other variables of the group, they hence take into account statistically, the influence of the other variables on the calculation of the adjusted mean. The Bonferroni adjustment, used here [143], is one of several methods used to counteract the problem of multiple comparisons.

5.3 RESULTS

In total, 564 data sets were recorded, with about 50 % of the experiments performed under physiological flow conditions. An overview of how many experiments have been conducted under which condition is provided in Table 5.1. We provide the raw data in a public repository [135]. The resulting Reynolds number (Re) of the ICA, based on the flow through it (Q_{ICA}), its cross sectional area $A_{ICA} = 8.74\ mm^2$ at the bifurcation and on the kinematic viscosity of water of $\nu = 1 \cdot 10^{-6}\ m^2/s$, ranged from 198 to 5774.

	Model	**N**	PP_{CCA} **(mmHg)**	Q_{ICA} **ml/min**
Physiol. Q	Compliant	55	16.07 ± 6.62	149.74 ± 77.97
	Stiff	197	20.02 ± 8.07	121.88 ± 84.61
Physiol. PP	Compliant	40	39.92 ± 3.35	348.3 ± 59.91
	Stiff	146	42.78 ± 4.23	302.41 ± 69.19
Extreme	Stiff	125	98.39 ± 25.43	585.81 ± 138.17

Table 5.1: Overview of test conditions with the number of recordings (N), mean CCA pulse pressure (PP_{CCA}) and flow rate (Q_{ICA}) in the internal carotid artery.

5.3.1 Spectrograms

The spectrograms of the P_{ICA} and LDV_{ICA} signals previously shown in Figure 5.3, are presented in Figure 5.5 in the 0-500 Hz range. The cardiac pulsation is evident in both the pressure and LDV signals. In the left panels (low flow rate), the highest intensity is around 50 Hz extending up to approximately 250 Hz (more prominent in the pressure signal) when the pressure and LDV reached their peak in the time domain and during the following deceleration phase. For the higher flow rates (right panels) the high-intensity and medium-intensity regions (red and yellow shading) move towards higher frequency values. However, little energy content was present above 500 Hz. The maximum intensity of the LDV signal spectra are, as expected, lower for the stiff model than for its more compliant counterpart (bottom panels).

5.3.2 Normalized Spectra

The normalized spectra of downstream pressure and downstream LDV signals, at location 1D for the compliant model, are depicted in Figure 5.6 in the left and right panels, respectively.

The spectra of the pressure signal showed a marked tendency to increasing energy content when moving towards higher flows. One aberrant finding is the drop-out near 50Hz of the pressure signal. This may be explained by the presence of appreciable electrical noise in the pressure recordings, especially under no-flow conditions, thus reducing the amplitude when normalizing the pressure spectra by subtracting the zero flow spectrum.

The spectra of the LDV signal showed, as well, a marked tendency to increasing energy content while moving towards higher flows. A notable finding

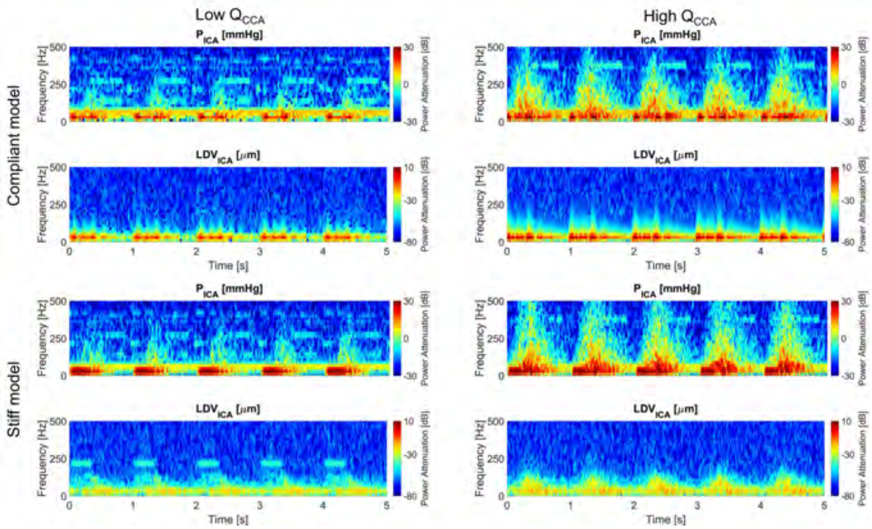

Figure 5.5: Spectrograms of the pressure and LDV at the ICA for the compliant (upper panels) and stiff (bottom panels) models obtained at 1D with low (left panels) and high (right panels) Q_{CCA}.

was that the LDV was not affected by the 50 Hz electrical noise. The spectra followed a similar trend for all flows, except for a 78 Hz peak which was present for $Q_{ICA} < 250$ ml/min while it broadened in the 100 - 150 Hz range for higher flow levels. The amplitude of the LDV spectra dropped for all flows around 150 Hz, and no meaningful signals could be detected above this frequency. The LDV signals showed the same pattern of increasing energy with increasing Q_{ICA} as those of the intra-arterial pressure.

5.3.3 Sensitivity Analysis

The statistical analysis performed for downstream pressure (P_{ICA}) and downstream LDV (LDV_{ICA}) signals yielded the F coefficient of the $Freq \cdot Q_{ICA}$ term, which revealed a similar trend for both signals with a peak in the 50 - 150 Hz range (Figure 5.7), where the sensitivity of the LDV was higher than that of the pressure catheter.

To compare LDV and pressure measurements, the EMMs (as a measure of the effect of the other variables on the calculation of the adjusted means) were evaluated when the pressure probe was inserted in the model, meaning evaluating equation 5.2 for condition probes = 1.

5.3.3.1 Compliant vs. Stiff models

The EMMs were evaluated regardless of the location in order to assess the impact of the model's material. The total number of samples for each frequency range was N = 357 and N = 49, for the stiff and compliant model, respectively.

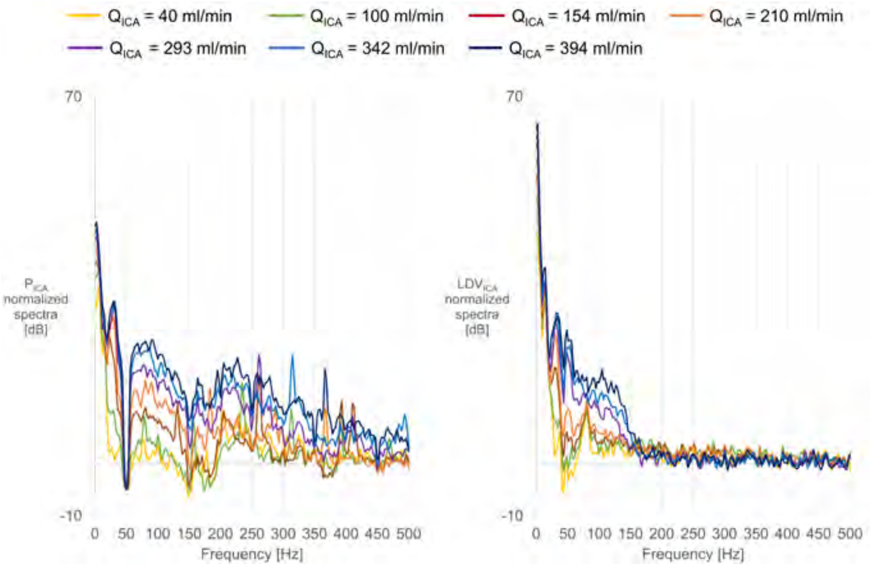

Figure 5.6: Normalized spectra of pressure (left panel) and LDV (right panel) signals, for multiple Q_{ICA} in the 0 - 500 Hz range.

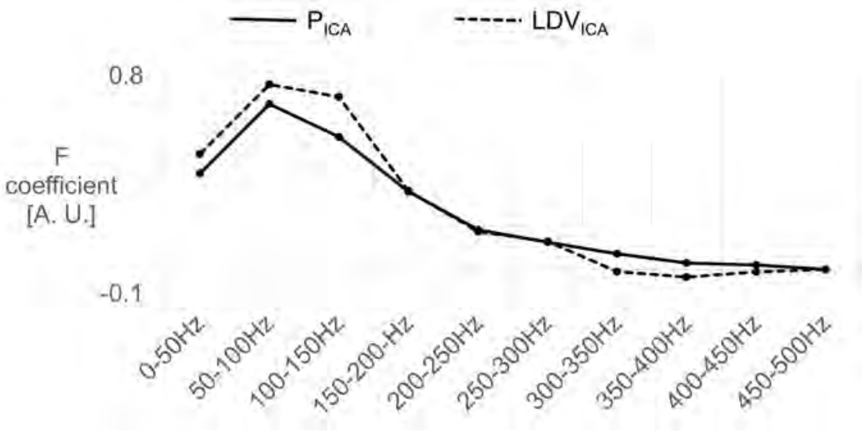

Figure 5.7: The F coefficient of $Freq \cdot Q_{ICA}$, resulting from the regression analysis of all available signals, showed that the sensitivity of LDV and pressure have a similar trend and that their sensitivity is the highest in the 50 - 150 Hz range.

The Q_{ICA} was 288.31 ± 201.35 ml/min. The model material had an effect on the overall dependency of the relation between PSD and frequency and the flow level, but this effect was similar for the pressure and the LDV measurements ($p < 1.0E-06$, $p < 1.0E-06$), as shown in Figure 5.8, left and right upper panels, respectively. The EMMs of the stiff model were higher than those of the compliant model for both signals, and the difference between them was more marked in the LDV.

5.3.3.2 *Measurement location*

To evaluate the impact of the measurement location on the LDV and pressure signals, we conducted an analysis for the compliant model only because of its greater clinical relevance. The resulting Q_{ICA} was 230.34 ± 119.89 ml/min, with N = 14, 13, 10 and 12 for each 50 Hz-wide frequency band, for measurement locations 1D, 2D, 3D and 4D, respectively. The EMMs of pressure decreased as the distance from the center of the stenosis increased ($p < 1.0E-06$), for all frequency bands (Figure 5.8 – left bottom). The strongest signal was found at 1D downstream from the stenosis. The gap between the 0 - 50 Hz range and the higher frequency bands is noteworthy. The maximum was in the 0 - 50 Hz range for the LDV as well (Figure 5.8, right bottom). For the LDV, however, the EMM value at 4D was found to be higher than at 1D. Therefore, for the LDV data, measurement location was not significant ($p > 0.01$).

However, it is relevant to note that, despite their small size (6F and 4F), the presence of pressure probes in the models was found to be a statistically significant factor ($p < 0.01$). The impact of the measurement location in the compliant model for the LDV was found to be significant ($p < 0.01$) but only when the manometers were not present, i.e. probes = 0.

5.4 DISCUSSION

In this hydraulic bench model study of a carotid artery, we have shown that post-stenotic flow instabilities induce vibrations that can be detected from surface measurements by means of laser Doppler vibrometry. Frequency domain analysis revealed that the relevant frequency band is 0 - 200 Hz, as little useful information was found at frequencies above 200 Hz. The sensitivity of the LDV measurement to changes in trans-stenotic flow level was found to be comparable to what can be achieved using an intra-arterial manometer. We consider the results of our study a proof-of-concept of the technique for carotid stenosis diagnosis by detecting neck skin vibrations.

The main purpose of these tests was to establish whether the LDV was able to distinguish different trans-stenotic flow regimes (and presumed different levels of flow instabilities) and to determine the relevant frequency range to

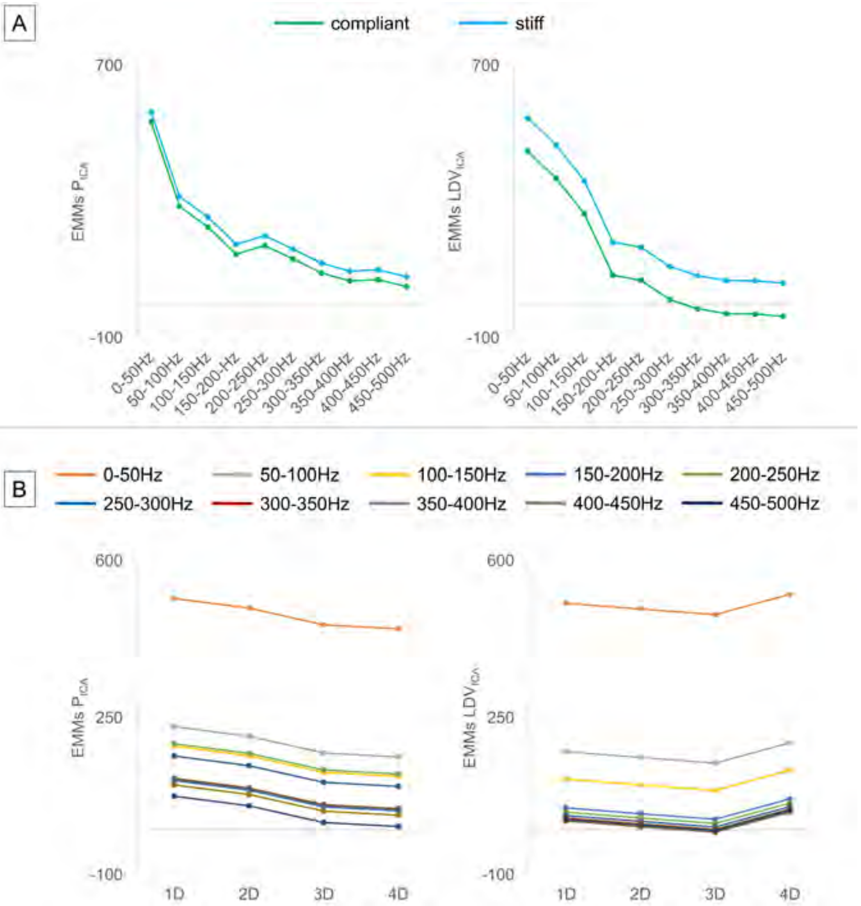

Figure 5.8: (A) The stiff model lead to higher EMMs for both the integrals of normalized spectra of pressure and LDV in the ICA (P_{ICA} and LDV_{ICA}, respectively). (B) The EMMs decreased while moving further downstream from the stenosis for the pressure, and this trend was not as marked for the LDV where the 4D signal was above the 1D level.

investigate. To quantitatively address these questions, a statistical analysis of the energy content of the LDV and reference pressure signals was conducted by applying a univariate linear model to the PSD integrals.
The statistical analysis showed that the LDV was able to distinguish different flow levels in the envisioned range, as could the pressure probe, with a comparable sensitivity (Figure 5.7). We found that there seems to be very little energy in the signals beyond 200 Hz, as displayed in Figure 5.8, where the EMMs rapidly decline in magnitude with increasing frequency.
Furthermore, our data suggest that the 0 - 200 Hz range covers the frequency band within which to seek the footprint of the stenosis. As the instabilities are generated in the diverging region distal to the stenosis, one might expect that the highest sensitivity of the technique would be distal to the stenosis. Table 5.2 shows that this is confirmed by the statistical analysis. While the effect of increasing flow on the area under the PSD curve is significant for frequencies up to 200 Hz for P_{ICA} and up to 150 Hz for LDV_{ICA}, the difference between zero flow and flow in P_{CCA} was no longer significant at 100 Hz and for the LDV with a beam directed at the skin over the bifurcation, was significant only up to 50 Hz. Therefore, a 100 Hz threshold seems to make it possible to discern unstable post-stenotic flow from the more laminar flow of the CCA. This encouraging finding suggests that a frequency analysis of the LDV signals would allow us to discriminate between patients and healthy subjects, as a healthy carotid bifurcation is not subjected to stenosis-induced flow instabilities. Furthermore, based on our data, a 2 ms temporal resolution would suffice to infer the presence of stenosis-induced flow instabilities. The currently used LDV default resolution (10 µs) would hence not be necessary for this application. These findings would reduce drastically the amount of data storage required for in-vivo measurements, making the recordings faster to analyze hence allowing real-time processing in daily clinical practice.

Measurement location, evaluated at several sites distal to the stenosis, came out as a significant factor in the statistical model, as reflected in the EMM values shown in Figure 5.8B. For P_{ICA}, there is a clear decrease in the magnitude of the EMM as one moves further downstream from the stenosis, and thus away from the zone where flow disturbances are generated. The effect of measuring location on the PSD of the LDV was largely similar, except for one location (4D). We speculate that this is due to the complex wave propagation mechanics through the arterial walls and the gel. Location 4D was also closer to the distal wall of the Perspex box so probably more affected by reflections due to its stiff walls. Another effect that may also have played a role is the presence of the catheters, which was found to be significant. We speculate that the presence of the catheters, despite their modest dimensions, promoted the induction of flow instabilities through their obstructive effect (the downstream catheter had a nominal diameter of

Freq. Range	P_{ICA}	LDV_{ICA}	P_{CCA}	$LDV_{bif.}$
0-50 Hz	**2.79E-10**	**1.59E-08**	**1.59E-17**	**1.65E-05**
50-100 Hz	**3.07E-09**	**2.56E-07**	**6.55E-03**	2.26E-01
100-150 Hz	**2.80E-07**	**2.12E-03**	2.20E-01	5.82E-01
150-200 Hz	**1.26E-03**	5.84E-01	1.75E-01	3.68E-01
200-250 Hz	1.84E-01	9.90E-01	4.58E-04	2.94E-01
250-300 Hz	4.42E-01	9.52E-01	1.85E-02	3.60E-01
300-350 Hz	3.80E-01	9.89E-01	9.76E-01	2.71E-01
350-400 Hz	2.41E-01	9.26E-01	2.82E-03	6.64E-01
400-450 Hz	6.89E-01	9.73E-01	1.34E-01	9.63E-01

Table 5.2: Statistical significance (bold text, $p < 0.01$), the interaction term in eq. 5.2, confirms a dependence of the area under the PSD curve within the specified frequency range on the level of flow. This indicates the frequency bands containing relevant information for stenosis detection. Data are given for pressure measurements up- (CCA) and downstream (ICA) of the stenosis, and for LDV measurements up- (bifurcation) and downstream (ICA). Data shown are for the compliant model; all measurements with pressure catheter present.

1.5 mm and the cross-sectional area ratio hence ranged from 7.6 % (based on $A_{downstream}$) to 31.7 % (based on $A_{stenosis}$). Furthermore, the motion of the catheters, further amplifying the vibrations, might have played a role as well. As it was the purpose of this study to assess the congruence between LDV and pressure signals, considered as the gold-standard, there was no other option but to insert pressure catheters in the arterial lumen. The impact of the location on the displacement signals when the flow was not disturbed by the presence of the intra-arterial pressure probes (probes = 0) was found to be significant.

We performed experiments in both a compliant and a stiff model, with the stiff model measurements mainly performed as a basis for comparison with an ongoing CFD study that is beyond the scope of this experimental report. As is clear from Figure 5.3, signals were very different in both model settings, which translates into significantly different EMMs for the stiff and the compliant model. In particular, the stiff model was much more susceptible to wave reflections, visible in much stronger oscillations in pressure and LDV data that particularly increased the energy content of the signals in the 0-50 Hz band. As expected, the amplitude of measured displacements was much lower in the stiff model than in the compliant model. The direct relevance of the stiff model experiments may be limited within the specific context of the assessment of LDV as a tool to screen for vibrations on the skin surface. Nevertheless, measurements do show a similar dependency of the PSD integral on the imposed flow level to that of the measurements in the compliant model, and were therefore included in the analysis. Including all available data led to an imbalance in the amount of data obtained from the compliant and stiff models in the statistical analysis. We verified, however, that all conclusions and relations between the two models are maintained when only considering data generated under physiological flow conditions and excluding all other data (Table 5.1, top 2 rows).

The values of Reynolds number used in this study spanned a wide range, with extreme values clearly beyond the physiological range in the carotid arteries [140]. This was done intentionally, as it was our specific aim to provoke flow instabilities and to run the model over a wide range of Reynolds numbers, encompassing laminar and highly turbulent flow conditions. The resulting average Reynolds number of all recordings was found to be Re = 1848. Using laser Doppler anemometry to investigate a 75 % axisymmetric stenosis, it has been previously shown that, for a similar value of Re, turbulent flow was detected [144]. Note also that flow instabilities in the normal carotid arteries have been shown to arise at Reynolds number well below 1500, the lower limit of the commonly assumed threshold for transitional flows [74]. Secondly, water was used as test fluid for the experiments. This suited the purpose of the proof-of-concept study and is not expected to have an impact on the threshold value of Reynolds number for the onset of flow instabilities in the experimental setting. However, flow instabilities will only occur for in-vivo trans-stenotic flow levels that are 3 to 4 times higher than in this study. The impact of fluid viscosity on the intensity of flow instabilities and their onset is currently being investigated by means of a computational analysis, which will be reported in due course.

In this well controlled hydraulic bench study, the luxury of having a no-flow reference allowed us to improve the signal to noise ratio of the data and normalize PSD spectra to the no-flow condition. Measuring no-flow conditions was considered important as the recordings were not performed in an isolated noise-free laboratory, therefore the flow related features could have been missed among the background noise. Furthermore, showing the normalized PSD spectra of both LDV and pressure signals gave us to the chance to visually compare them with respect to their frequency-based behavior only. The comparison between the normalized and un-normalized data (namely the raw FFT data), however, showed no major differences in the predicted EMM trends for both P_{ICA} and LDV_{ICA}. Besides the absolute value, the outcome of the statistical analysis for the un-normalized data, for the various locations examined on the compliant model with manometers present, does not differ substantially from the one of the normalized data.

The lack of a no-flow reference would hence not be likely to have a major impact on the outcome of the analysis in-vivo.

An important limitation of this study is the fact that only one stenosed carotid geometry was tested (albeit extensively, covering a wide range of flow conditions and in a compliant and stiff material). While testing additional models with other degrees of stenosis (as well as those with no stenosis) and using different tissue-mimicking materials is certainly valuable, experimental testing using a variety of patient-specific carotid models, with different degrees of stenosis, differing geometries and different flow regimes, is time consuming and cumbersome to perform. For this reason we are presently carrying out a detailed high resolution computational analysis of the problem which can simulate a wide variety of patient-specific stenoses and with which it will be possible to estimate the sensitivity and specificity of this approach to the detection of occlusive carotid artery disease. The results of this study will be reported in due course. For now, we speculate that the critical parameters will be the degree of stenosis and its 3D geometry [145], [146], combined with the level of trans-stenotic flow [11].

Overall, we conclude from this proof-of-concept study that the LDV is, in principal, able to recognize the presence of a stenosis – given that it produces flow instabilities. Note, however, that this study does not allow us to draw any conclusion regarding the critical level of stenosis that would be detectable with the methodology. Besides additional computational analysis, in-vivo measurements are currently in progress to assess the sensitivity and specificity of the envisioned technique.

5.5 ACKNOWLEDGEMENTS

The study was done within the context of the Early stage CARdio Vascular Disease Detection with Integrated Silicon Photonics (CARDIS) project, funded by an EU H2020 644798 grant. We gratefully acknowledge the contribution of the entire consortium and the teams behind the development and construction of the multi-beam LDV prototype.

CHAPTER 6

FLOW INSTABILITIES: A BIOMARKER FOR STENOSIS DETECTION?

This chapter concerns the evaluation of the possibility of using flow instabilities as marker for the presence of carotid stenosis. This study was conducted by steps. Firstly, we focused on the validation of the computational methodology, by comparing the intensity of flow instabilities recorded throughout the experimental study and the ones computed using the *in-silico* methodology on the same patient-specific geometry. The two data sets were found in good agreement, allowing us to claim that the computational model provides plausible results and could, therefore, be used to investigate a larger set of parameters. Secondly, we used the validated *in-silico* model to evaluate the impact of flow rate, flow split and stenosis severity on the intensity of post-stenotic flow instabilities. Finally, we evaluated sensitivity, specificity, and accuracy of using the intensity of flow instabilities as a marker for stenoses detection.

The chapter is based on the paper Computed Post-Stenotic Flow Instabilities Correlate Phenotypically with Vibrations Measured Using Laser Doppler Vibrometry: Perspectives for a Promising In-Vivo Device for Early Detection of Moderate ad Severe Carotid Stenosis., *Journal of Biomechanical Engineering*, vol. 142, no. 9, pp. 091007 1-13, 2020 [104].

6.1 INTRODUCTION

More than three million people died worldwide due to an ischemic stroke in 2017 [147], where the underlying disease was carotid stenosis in one of ten stroke patients [2]. Early detection could decrease mortality [53] and impact elective therapy [47]. However, the majority of carotid stenoses are asymptomatic and rarely detected. The most common clinical screening method for asymptomatic carotid stenosis is auscultation of the post-stenotic turbulence-induced carotid bruit [7]–[9]. Carotid auscultation's specificity is approximately 80 %, but sensitivity is operator-dependent and varies from 50 % to 70 % [13], [14].

Post-stenotic pressure fluctuations induce vibrations in the arterial wall, which propagate as mechanical waves to the skin, and manifest as vibrations or sound waves [148]. Extensive studies have been performed on the analysis of the downstream-stenosis turbulence [149], [150]. Furthermore, the post-stenotic flow instabilities are well known to be affected by stenosis degree, the volumetric flow rate in the common carotid artery and the flow split between the internal carotid artery and external carotid artery [76], [83]. However, to the best of our knowledge, no study systematically analyzed a complete combination of these factors potentially affecting the intensity of flow instabilities, varying over the pathophysiological range, or addressed the correlation between (the intensity of) stenosis-induced flow instabilities and skin vibrations.

Laser Doppler Vibrometer (LDV) is a promising method for inferring carotid stenoses as a result of its high spatiotemporal resolution (10 nm, 10 μs) [21]. We recently performed an in-vitro experiment [103] using a novel multi-beam LDV [21] to measure the displacement of the surface of the gel embedding a compliant replicate of a patient-specific carotid bifurcation stenotic model. We found a significant correlation between flow rate and the wall displacement in the 0-200 Hz range. The experiment, intended as a proof-of-concept for showing that the LDV could be used for inferring presence of asymptomatic carotid stenosis, was limited to only one degree of stenosis. Computational fluid dynamics (CFD), on the other hand, has established itself as a key methodology to cheaply assess relevant fluid dynamical quantities [151], allowing for parametric studies that, in contrast, would be experimentally labor-intensive. Furthermore, we recently conducted a study to identify the sufficiently accurate numerical methodology to simulate downstream-stenosis flow instabilities [101].

The aim of this study was threefold:

1. to assess the validity of using CFD to mimic the physics of the phenomenon whereby flow instabilities induce high-frequency pressure

oscillations that propagate to skin level;

2. to analyze the parameter space of pathological and healthy models, in order to provide a correlation between flow rate, flow split and stenosis severity and the intensity of post-stenotic instabilities;
3. to investigate the receiver operating characteristics (ROC) derived sensitivity, specificity and accuracy of using LDV to infer the presence of a stenosis, by populating the correlation previously found in (ii) with a resolution and variability reflective of a population, therefore obtaining a fictitious clinical study.

As such, the presented study does not aim to provide a comprehensive understanding of the post-stenotic flow field, but rather a proof-of-concept of the ability of the LDV to detect stenosis with physiologically plausible flow conditions in this specific carotid bifurcation geometry.

6.2 MATERIALS AND METHODS

6.2.1 Computational Fluid Dynamical Model

We took advantage of the patient-specific geometry presented in Iannaccone et al. [115], which was a segmentation of a carotid bifurcation of a 75 y/o man with a 76 % stenosis in the internal carotid artery (ICA). With a focus on assessing the impact of stenosis severity, we used the plausible pre-lesion lumen, segmented by Iannaccone et al. [115], as a healthy control. Furthermore, we obtained four additional degrees of stenosis, varying from moderate to extremely severe (56 %, 66 %, 86 %, 96 %), by adapting the open-source tool morphMan [152] on the segmented 76 % stenotic geometry (see Figure 6.1A). Specifically, the cross-sectional area of the original model within the region of interest (6.1B) was multiplied by a factor (6.1C). Finally, the centerlines and the Voronoi diagram of the surfaces were used to obtain the four geometries. Please refer to Kjeldsberg et al. [152] for a more thorough description of the methodology.

The healthy and the five additional models, each with a different degree of stenosis, were meshed using VMTK [132] with four boundary layers and a local refinement in the stenosis area or, for the healthy geometry, where the stenosis developed. The spatial resolution, measured as averaged cell length (Δx_{mean}), was set to $\Delta x_{mean} = 1.92 \cdot 10^{-4} m$ (error < 5 % with respect to Richardson extrapolated solution [126]) accordingly to the spatial refinement study that was recently performed with a focus on the turbulent-like flow features on the same model [101], resulting in 32 tetrahedral cells across the stenosis area in the original 76 % geometry. Furthermore, we varied the

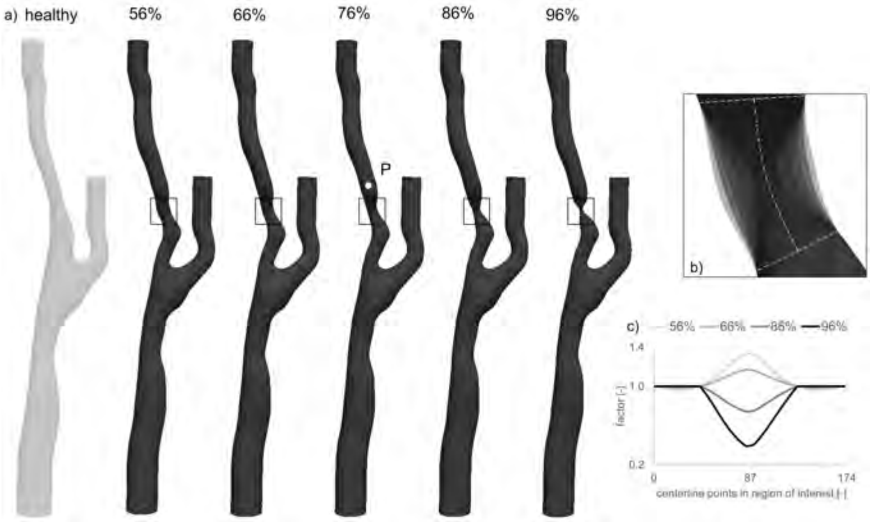

Figure 6.1: A) The healthy and 76 % stenosis were obtained from Computer Tomography Angiography images [115]. The remaining four degrees of stenosis were obtained by multiplying the cross-sectional area of the original stenotic geometry [152] within the region marked by the dashed lines reported in B) with the factor reported in C). Furthermore, in B) the details of the stenosed geometries are shown as overlapped, and the centerline of the models is reported as a dotted-dashed line. The pressure field was probed at point **P** located 1D downstream of the stenosis on the centerline of the ICA.

volumetric flow rate (Q) imposed at the common carotid artery (CCA) and the flow split between ICA and external carotid artery based on the in-vivo variability reported in three clinical studies [33], [118], [140]. A combination of all possible permutations between stenosis degree, Q_{CCA} and Q_{ICA}/Q_{CCA} leads to 150 simulations, as a result of setting the mean ± one and two standard deviations (SDs) for Q_{CCA} and Q_{ICA}/Q_{CCA} for each of the six degrees of stenosis. Only a subgroup of the possible scenarios was run, in order to efficiently cover a wide range of physiological conditions. The simulations were organized into five categories. The first category consists of six simulations carried out on several degrees of stenosis with boundary conditions matching mean physiological values reported on a population level [118], [140]. In the second and third category, we used the 76 % stenosis model and changed the CCA flow rate and the ICA flow split, separately with ± one and two SDs. The flow split of the healthy model was changed as minus one and two SDs in the fourth category. In the fifth category, we simultaneously varied a combination of multiple parameters, in order to populate the parameter space with permutations matching a Reynolds number between 300 and 380, in which we observed a phenotypical change in the flow field of intermediate results, resulting in five simulations. In total, encompassing all categories, we ran 21 simulations with Q_{CCA} varying from 145 to 529 ml/min and Q_{ICA}/Q_{CCA} from 11.9 to 70.8 % (see Table 6.1), reflecting the physiological range [153]. To contain the influence of the numerical setting on the solution, the flow split was imposed by setting its complementary value at the outlet of the external carotid artery, while a zero pressure boundary condition was set at the ICA outlet.

The walls of the model were assumed as rigid, as commonly used for the biomechanical analysis of healthy and stenotic carotid arteries [154]. Blood was modeled as a Newtonian fluid [111], [155] with kinematic viscosity $\nu = 3.3 \cdot 10^{-6}$ m^2/s, and we simulated three cardiac cycles using the 2^{nd} order finite-element Navier-Stokes solver Oasis [95]. The waveform was taken from Hoi et al. [33], but scaled to match the average inlet flow rate, and set as Womersley flow with 20 modes. The time step was set to $\Delta t = 5 \cdot 10^{-5}$ seconds, i.e. five times smaller than the time step size at which we noticed effects of time resolution on the flow field, based on a spatio-temporal refinement study focused on turbulent-like flow [101]. The chosen time step size matched the sampling frequency of the LDV in the experimental studies (20 kHz) [103].

6.2.2 Post Processing of Computational Data

The post-processing workflow is depicted in Figure 6.2 and can be described by the following steps:

1. We extracted the pressure during the two last cardiac cycles at a point **P**, located on the centerline of the ICA, 8 mm downstream of the stenosis (see Figure 6.1), as it was find to be the most relevant measuring location among the ones tested in-vitro;

2. The power of the pressure trace (P) was then computed in LabChart Pro v8. The fast Fourier transform was calculated from 1000 points with Hann windowing with 50 % overlap;

3. The integral of P was computed in Excel (Microsoft, 2016) using the trapezoidal rule within the frequency range of interest $[f_{min}, f_{max}]$. Unless otherwise reported in the contextual section, the default f_{min} value was set to 20 Hz to exclude the pulsatility of the inlet waveform only, and f_{max} was set to 10 kHz to encompass the entire available frequency range;

4. Finally, we computed the logarithm of the integral, equivalent to a metric of the intensity of flow instabilities ($IFI_{[f_{min}, f_{max}]}$), that can be mathematically expressed as in equation 6.1.

Stenosis Degree (%)	Q_{CCA} (ml/min)	Q_{ICA}/Q_{CCA} (-)	**Category** (-)
None	389	65.5	degree of stenosis
56	337	58.8	
66	337	57.8	
76	337	45.0	
86	337	28.0	
96	152	11.9	
76	145	45.0	flow rate
76	241	45.0	
76	433	45.0	
76	529	45.0	
76	337	18.0	flow split
76	337	32.0	
76	337	58.0	
76	337	72.0	
None	315	54.5	healthy flow split
None	315	65.5	
56	241	70.80	combination
66	337	44.4	
76	279	45.0	
86	337	28.8	
86	433	28.0	

Table 6.1: List of inflow and flow split set for each CFD simulation with several degrees of stenosis. Note that the average flow rate and flow split changes with degree of stenosis, and is therefore not constant in the "degree of stenosis" category.

Stenosis Degree	**AUC based on** $IFI_{[0Hz,40Hz]}$	**AUC based on** $IFI_{[80Hz,200Hz]}$
Moderate (56%,66%,76%)	0.559	**0.843**
Severe (86%,96%)	**0.972**	0.162
All (56% – 96%)	0.726	0.569

Table 6.2: The accuracy of the intensity of flow instabilities IFI in the 0 - 40 Hz range shows that it is a good predictor for severe stenoses, while it is poorly accurate for moderate stenoses detection. In the 80 - 200 Hz range, on the other hand, the IFI can infer the presence of moderate stenoses and, with lower accuracy, of the severe stenoses too.

$$IFI_{[f_{min},f_{max}]} = \log_{10} [\int_{f_{min}}^{f_{max}} P] \qquad (6.1)$$

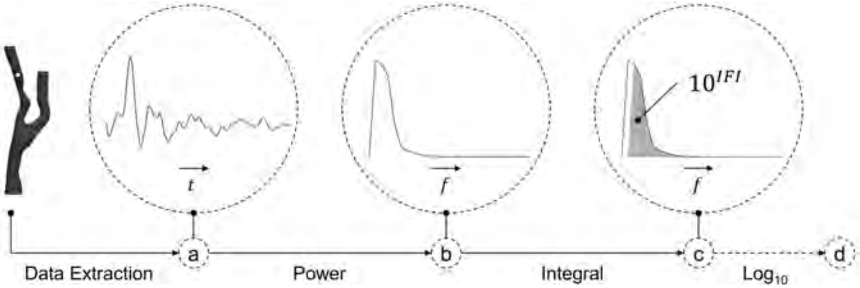

Figure 6.2: Post-processing workflow applied to both computational and experimental data.

Furthermore, for visualization purposes only, we performed a high-pass filter on the pressure trace with cut-off frequency at 20 Hz, in order to provide a qualitative representation of the pressure fluctuations. The method was previously explained in [101] and based on the study reported by [122].
For volumetric visualization, we also computed the Q-criterion, which identifies spatial regions in the velocity field where the Euclidean norm of the vorticity tensor ($\overrightarrow{\Omega}$) dominates the strain rate tensor ($\overrightarrow{S}$) [120], as defined in equation 6.2.

$$Q - criterion = \frac{1}{2}(|\overrightarrow{\Omega}|^2 - |\overrightarrow{S}|^2) > 0 \qquad (6.2)$$

6.2.3 Validation against Computational Data

A brief overview of the experimental methodology is reported to allow a better understanding of the validation strategy; details are found in Mancini et al. [103]. The in-vitro set-up consisted of a compliant replica of a 76 % stenosed patient-specific carotid bifurcation, the same geometry used in this study, embedded in a soft-tissue mimicking gel and a skin-mimicking polyurethane foil on top of it. LDV measurements were acquired at several locations upstream and downstream of the stenosis. The displacement recorded using LDV in the in-vitro experiments is, from now on, referred to as EXP. The LDV was found to be most sensitive to flow rate changes at a location corresponding to point **P**, which was therefore deemed the most relevant. For comparison with the CFD data, we chose a sub-set of the in-vitro experiments where the CCA flow rate was within mean ± 2 SD of clinically observed flow rates [140] and mean ICA flow split [118] (see Table 6.3) in order to compare them with the simulations in the "flow rate" category. Note that the CCA flow rate of the two datasets is in the same range, but not exactly matching because of the difficulty of controlling the flow rates during the in-vitro experiments. It is worth noticing that the two datasets are not directly comparable, as the experimental displacement was measured at the surface of a deformable and gel-surrounded model, whilst the intra-arterial pressure traces are obtained in a rigid model by a CFD solver. Therefore, a measure of the power of the two signals, i.e. IFI [20Hz-10kHz], was computed for the experimental data as well, with the same post-processing process applied to the CFD data (summarized in equation 1). We assessed the similarity of the skin-mimicking foil displacement and intra-arterial computational pressure by computing the correlation of IFI [20Hz-10kHz] at point **P** in the two datasets and, therefore, obtaining a concordance correlation coefficient.

6.2.4 Metrics Correlating with Flow Instabilities

To assess which metric best correlates with the level of flow instabilities, we performed six linear regression analyses between $IFI_{[20Hz,10kHz]}$ of the stenosed geometries ($IFI^{stenotic}_{20Hz-10kHz}$) and a total of six parameters, specifically the three imposed parameters (Q_{CCA}, Q_{ICA}/Q_{CCA} and $Area_{stenosis}$, the area of the stenosis) and three derived quantities, i.e. Q_{ICA}, the velocity and Reynolds number at the throat of the stenosis ($Velocity_{stenosis}$ and $Re_{stenosis}$, respectively). The derived quantities were chosen based on their relevance in a fluid dynamical context. The quantity that was found to best correlate with the presence of flow instabilities is now referred to as metric. The regression analysis between the six quantities and $IFI^{healthy}_{20Hz-10kHz}$ was also computed for the healthy geometry, allowing us to identify the key indicators to distinguish a normal carotid from a stenotic.

Stenosis Degree (%)	Q_{CCA} (ml/min)	Q_{ICA}/Q_{CCA} (-)	**Category** (-)
76	107	36.4	EXP
76	225	44.8	
76	334	47.1	
76	448	48.1	
76	601	48.7	

Table 6.3: List of inflow and flow split set during the in-vitro experiments to allow validation of the CFD approach by comparing the simulations in the “flow rate” and the “degree of stenosis” categories, for the 76 % stenosis only. In the experiments, the ICA flow split was kept as close as possible to the mean physiological value, while the CCA flow rate was varied as within the physiological range by setting it at mean, ± 1 SD and ± 2 SD ml/min

6.2.5 Proof-of-concept for Sensitivity, Specificity and Accuracy of an LDV Device for Stenosis Detection

Sensitivity, specificity and accuracy are commonly used to assess the predictive performance of a device or a method based on data of patients enrolled in a clinical trial. Clinical measurements, however, are subject to many disturbing co-founders, which is something that simulated data is immune to. Therefore, we took advantage of the computational data to provide a proof-of-concept on the feasibility of LDV to differentiate a stenosis from the normal setting in the tested geometry using power spectral features. Specifically, we used the IFI metrics within the frequency range identified by the in-vitro experiments (0-200 Hz). Preliminary analysis of CFD results demonstrated that the IFI of a stenosis was low (absence of flow instabilities) either because of the geometry that was insufficiently stenosed, or because of how limiting severe stenosis act on the flow rate. We, therefore, choose to investigate two sets of frequency ranges, specifically the 0 - 40 Hz and the 80 - 200 Hz ranges, where the former would allow us to assess the flow rate level, and the latter the intensity of flow instabilities. The choice of the frequency ranges is properly addressed in the Results section under "Frequency-based stenosis indicators". Furthermore, to enable a sensitivity and specificity analysis, additional data is required beyond the data obtained from the 21 CFD simulations. Therefore, we used the data from the 21 simulations to create a regression model that allowed us to create a fictitious population of 50,000 subjects, varying the parameters (CCA flow rate and ICA flow split) with five equally large subgroups for each degree of stenosis, and an additional 10,000 fictitious subjects without any ICA stenosis. For each fictitious subject, we drew a random point with coordinates (x,y) from a multivariate distribution, with covariate matrix equal to identity matrix and null mean, and assigned a CCA flow rate and an ICA flow split as $Q_{CCA} = Q_{CCA} - mean + x \cdot Q_{CCA} - SD$ and $Q_{ICA}/Q_{CCA} = Q_{ICA}/Q_{CCA} - mean + y{\cdot}(Q_{ICA}/Q_{CCA}){-}SD$, respectively. The distribution coordinates x and y vary between -2 and +2 units in order to represent a population varying between ±2 SD. The mean and standard deviation values are dependent on the degree of stenosis, following [33], [118], [140], and reported in Table 6.1 – category "degree of stenosis". Physiologically non-plausible conditions (i.e. Q_{CCA}<0 and Q_{ICA}/Q_{CCA}<0) were omitted, giving a final fictitious population of 45756 patients and 9116 controls with $Q_{CCA} = 298 \pm 107$ ml/min and $Q_{ICA}/Q_{CCA} = 0.40 \pm 0.21$ across all degrees of stenosis, and Q_{CCA}=388 ± 65 ml/min and $Q_{ICA}/Q_{CCA} = 0.655 \pm 0.1$ for the healthy model.

Based on the geometrical and flow rate information of each fictitious subject, we could compute all the potential metrics for the entire fictitious population. We then correlated the metric with $IFI_{[f_{min},f_{max}]}$ to obtain the regression coefficients for each frequency range, and therefore computed an approximation of $IFI_{[f_{min},f_{max}]}$ ($IFI'_{[f_{min},f_{max}]}$) for each fictitious subject without running a full CFD simulation. Of note is that the regression coefficients were computed separately for the 18 stenotic models and for the three healthy ones, for each relevant frequency range.

Finally, we performed a receiver operator characteristic (ROC) analysis [156] to evaluate the ability of $IFI'_{[f_{min},f_{max}]}$, evaluated at both frequency ranges, to infer the presence of a carotid artery stenosis. We varied the cut-off value from min to max of each $IFI'_{[f_{min},f_{max}]}$ and computed the rate of true positives (TP_{rate}, and the rate of false positives (FP_{rate}), equivalent to sensitivity (Sn) and 1 – specificity (Sp), respectively. The accuracy of the test was calculated as the area under the curve (AUC) of the ROC curve by means of the trapezoidal rule. We chose the optimal cut-off value based on the Youden Index [157], defined as J = max_c(Sn(c)+ Sp(c)-1).

6.3 Results

6.3.1 Computational Findings

An overview of the velocity field of the "flow rate" category is shown in Figure 6.3 to allow for a qualitative analysis of the well-resolved physics of our computational methodology.

The velocity traces in point **P** (Figure 6.3a) and the volumetric rendering of the instantaneous velocity magnitude field at t = T/4 (Figure 6.3b) are reported for increasing Q_{CCA} (Figure 6.3c). The pressure fluctuations in the ICA increase proportionally to the CCA flow rate, as highlighted by the high velocity jet emerging from the throat of the stenosis. The increased velocity leads to the formation of flow instabilities in the more distal ICA. The combined effect of increased velocity magnitude and its subsequent effect on the intensity of flow instabilities are clearly noticeable in the velocity traces of Figure 6.3a.

6.3.2 Validation against in-vitro Experiments

The traces of normalized computational pressure data and normalized experimental displacement obtained using LDV recordings are compared in Figure 6.4a where we can observe an increase in pressure drop and displacement magnitude with increasing flow rates. As expected, the raw data of the two datasets are not directly comparable one to the other.

The instabilities in the LDV signal are masked by its high amplitude. We, therefore, report the high-pass filtered signals in Figure 6.4b for a visual proof of the presence of flow instabilities. From the high-pass filtered pressure signals, we observe that for the two lowest flow rates there are little to

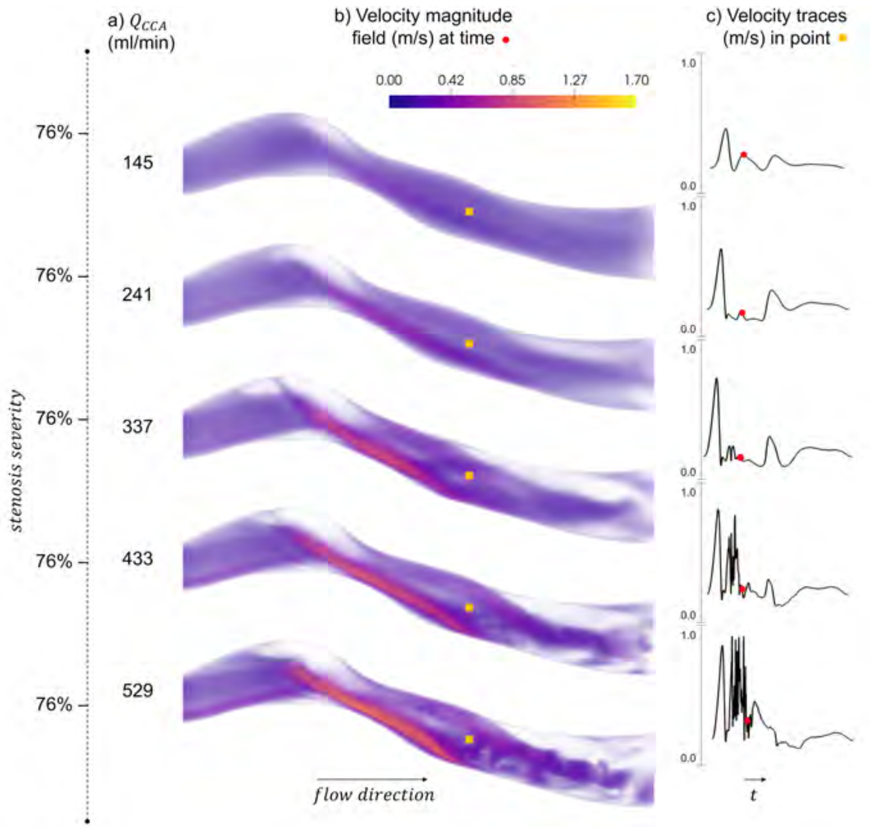

Figure 6.3: An increase in Q_{CCA} (a) leads to noticeable increase of velocity magnitude (b) and of flow instabilities (c) for the 76 % stenosis. The velocity traces in (c) were sampled in point **P** (yellow square), and the volumetric velocity magnitude in (b) was sampled at one fourth of the cardiac cycle (red dot). Higher Q_{CCA} implies higher velocity values at the stenosis throat, which trigger vortexes in the downstream region.

no high-frequency instabilities. In contrast, the high-pass filtered displacement traces for the three higher flow rates contain an increasing level of fluctuations. However, for both datasets, the fluctuations are present and increase with the flow rate, and the same applies to their power, shown in Figure 6.4c. Furthermore, the logarithm of their integral in the 20 Hz-10 kHz range, shown in Figure 4d, displays a similar linear trend, increasing with Q_{ICA}, suggesting that the intensity of the pressure fluctuations, as obtained from the CFD simulations, can be used as a proxy for the intensity of wall vibrations as measured with LDV. It is worth noticing that the data points in Figure 6.4d are plotted on separate y-axes, since we are comparing two different physical quantities. The two datasets were found to be in good agreement, with a concordance correlation coefficient of 0.9819. We can, therefore, conclude that our computational methodology provides plausible results for the patient-specific 76 % stenotic model. We could hence use CFD simulations to investigate a larger set of parameters.

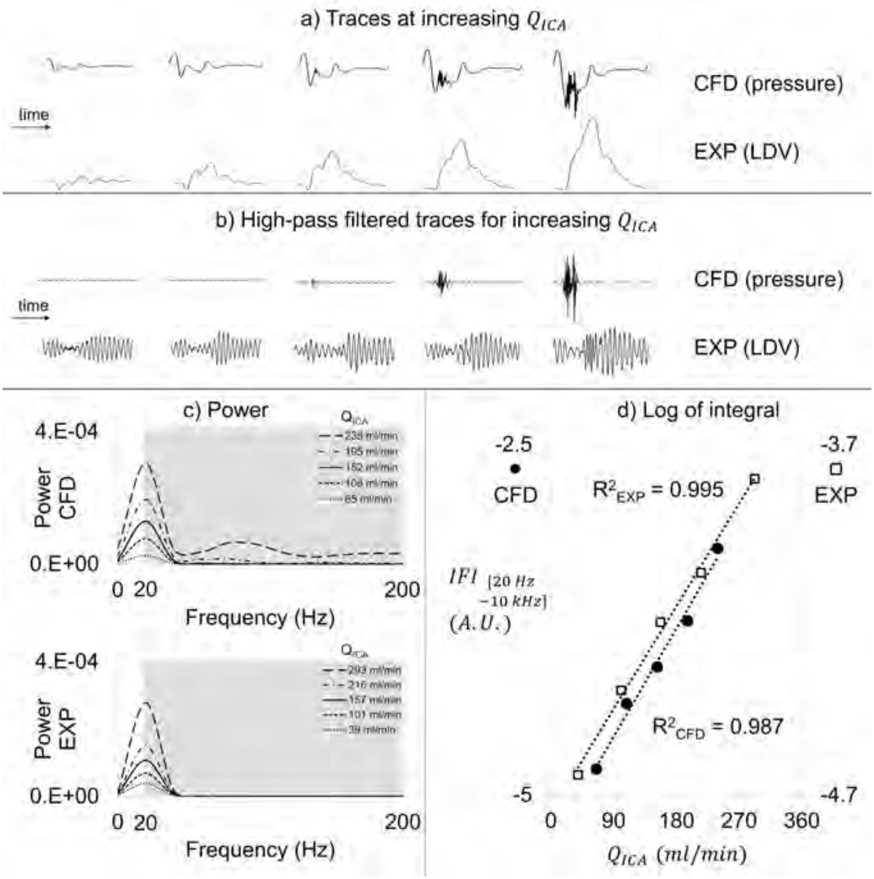

Figure 6.4: (a) The pressure obtained from the computational simulations is compared to the LDV displacement obtained from experimental tests at increasing Q_{ICA} (whose values are reported in the legends of panel c). The displacement increased in amplitude as the flow rate in the stenosed vessel increased, which lead as well to an increase of instabilities in the pressure field. The increase of instabilities with ICA flow rate is highlighted by the high-pass filtered time traces (b) and their power (c) of both the CFD and EXP data. Similarly, the scatter plot (d) shows that $IFI_{[20Hz,10kHz]}$ from both CFD and EXP data tend to increase together with Q_{ICA}. The grey box in (c) highlights the frequency range (20 Hz to 10 kHz) in which the IFI shown in (d) is calculated.

6.3.3 Metrics Correlating with Flow Instabilities in Stenosed and Healthy Models

In this section, we report the results of the correlation between the $IFI_{[20Hz,10kHz]}$ and six parameters describing the flow and stenosis geometry.

Specifically, Figure 6.5a to 6.5c shows the correlation of the three imposed parameters (Q_{CCA}, Q_{ICA}/Q_{CCA} and $Area_{stenosis}$) with $IFI_{[20Hz,10kHz]}$. Figure 6.5d to 6.5f shows the correlation of $IFI_{[20Hz,10kHz]}$ with the three obtained parameters (Q_{ICA}, $Velocity_{stenosis}$ and $Re_{stenosis}$).

The stenotic and the healthy models are analyzed separately to ease comparison between them. An increase in any of these parameters generally leads to an increase of the intensity of flow instabilities. Focusing first on the stenotic models, the stenosis area was the only factor where the slope of the regression line was not significantly different from zero with p-value > 0.05, and was a poor metric for IFI, accounting for only 15 % of the variation in the data. The correlation improved for Q_{CCA}, $Velocity_{stenosis}$ and Q_{ICA}/Q_{CCA}, with $R^2 = 0.39$, 0.56 and 0.54, respectively; but only Q_{ICA} and $Re_{stenosis}$ have an R^2 value of 0.90 (p-value < 0.05). For the sake of conciseness, we here report the results of the following analysis performed only for Q_{ICA} as metric, as Q_{ICA} is more relatable to measurements in existing literature and clinical practice. The Q_{ICA} was also found to be the best metric for the increase of IFI for the healthy models as well, comparable to $Velocity_{stenosis}$ and $Re_{stenosis}$. It is worth noticing that the linear correlation between most of the considered flow metrics and the IFI, computed as the logarithm of the energy integral, suggests that the parameters actually correlate exponentially with the intensity of flow instabilities.

A qualitative evaluation of the intensity of flow instabilities is provided using the high-pass filtered pressure signals, shown with the corresponding Q_{ICA} value in Figure 6.6. The simulations are depicted for increasing Q_{ICA} values. Of note is that the 96 % stenosis does not harbor flow instabilities, because of our physiology-based boundary conditions. The 86 % stenosis harbors weak instabilities only if the flow rate is above average, while the fluctuations harbored with average Q_{CCA} are negligible. The 76 % stenosis simulations exhibit a phenotypically different behavior depending on the flow split and inlet flow rate. More specifically, a high flow split or inlet flow rate (average + 2SDs) produced the most unstable flows, while the simulations with a reduction below the average of these parameters did not harbor high-frequency pressure fluctuations. The 66 % and 56 % are slightly unstable through the entire range of physiological CCA flow rate or flow split used in this study. The high-pass filtered pressure traces of the healthy model simulations are highlighted with a grey box. The healthy model does not show any flow instabilities, even though the Q_{ICA} would have been high enough to trigger flow instabilities in any of the stenotic models ($Q_{ICA} = 257$ ml/min).

Similar considerations can be drawn when evaluating the high-pass filtered pressure traces (a) and the Q-criterion (b) in the healthy model

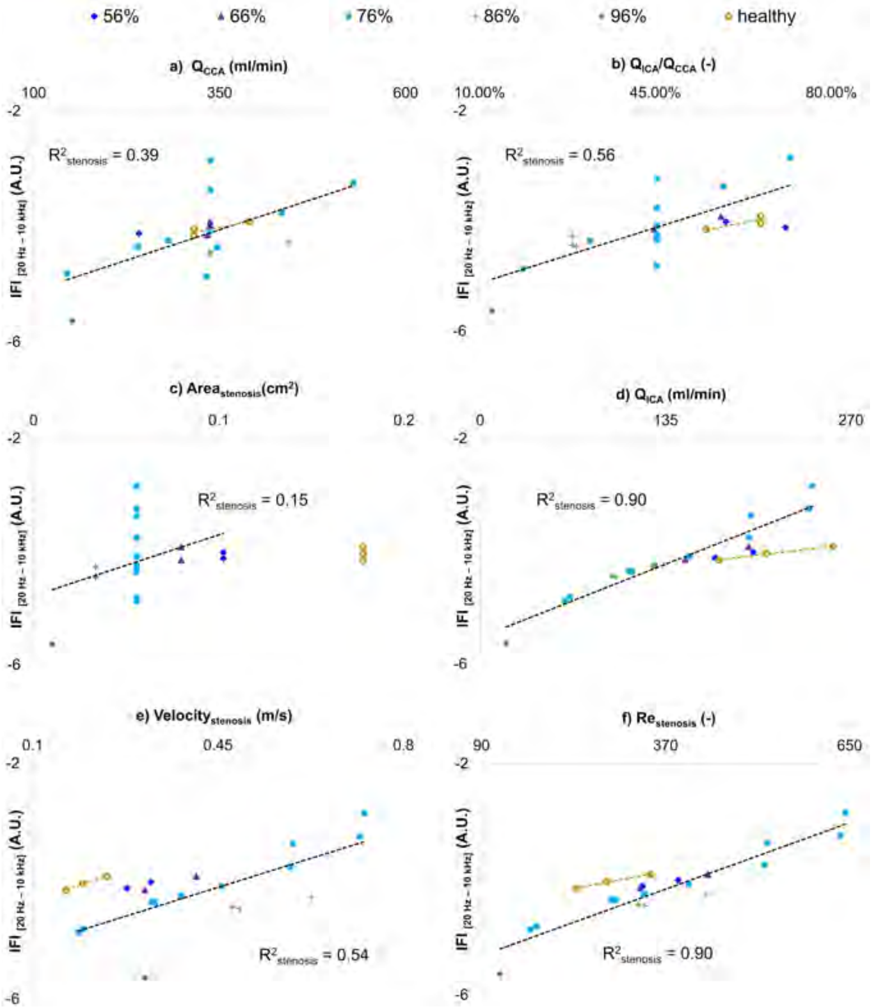

Figure 6.5: The impact of the physiologically relevant factors (Q_{CCA}, Q_{ICA}/Q_{CCA}, $Area_{stenosis}$, Q_{ICA}, $Velocity_{stenosis}$ and $Re_{stenosis}$) on the intensity of flow instabilities is depicted in separated plots. The regression analysis was performed for the stenotic and the healthy models separately. All factors are positively related with $IFI_{[20Hz,10kHz]}$ but their correlation varies between a minimum of 0.15 for $Area_{stenosis}$ and a maximum of 0.90 for Q_{ICA} and $Re_{stenosis}$.

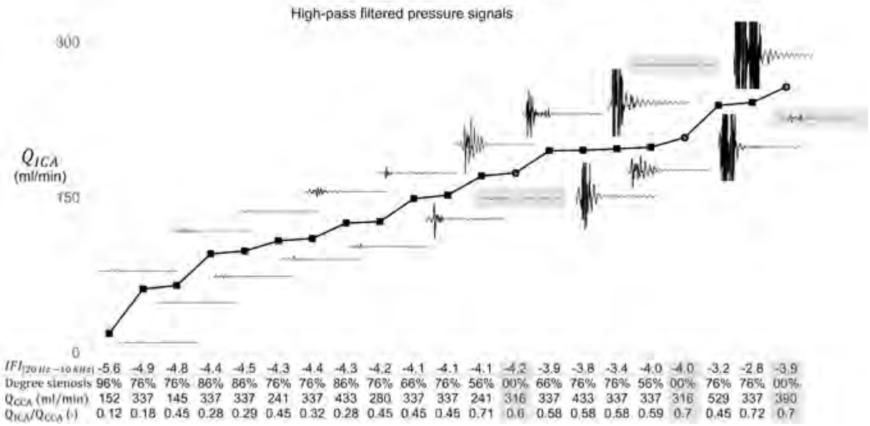

Figure 6.6: The incremental plot of Q_{ICA} highlights the positive relationship between the Q_{ICA} and the high-pass filtered pressure signals which, on the other hand, are largely insensitive to other expectedly relevant parameters such as stenosis severity, inlet flow rate and flow split. The $IFI_{[20Hz,10kHz]}$ is reported to show the difference between stenotic and healthy models' values. The high-pass filtered pressure signals obtained using the healthy model are highlighted with a gray box, showing that no flow instabilities arise even if their Q_{ICA} is in the range in which the stenotic models harbor intense instabilities.

simulation, together with Q_{ICA} (c) for each stenosis degree in Figure 6.7. Shifting our attention to the 56 % to 76 % stenosis models, it is possible to see flow vortexes both upstream, at, and downstream of the stenosis throat. The differences with the healthy model in both high-frequency pressure traces and vortexes are clearly noticeable. We find the lowest Q_{ICA} in the most severe stenoses (86 % and 96 %), where weak or no instabilities are present. The Q_{ICA} is hence a good metric for the presence of flow instabilities if a stenosis is present; otherwise, the geometrical factors have a predominant impact.

6.3.3.1 *Frequency-Based Stenosis Indicators*

Figures 6.6 and 6.7 suggest that the high-frequent flow instabilities can be used as indicator for the presence of the moderate stenoses (56 % to 76%), but not for severe stenosis as a result of the reduced flow, which was too low to induce instabilities. Analysis of the high-frequency contents of the signal in itself, therefore, would be insufficient to infer the presence of stenosis. Additional information may be found in a metric that would indicate the flow level in itself, which will be markedly lower in case of severe stenosis (86 % and 96 %). Therefore, the power spectrum in the lower frequency range may provide this information. The left side of Figure 6.8a illustrates that the majority of the energy related to the bulk flow is mostly present in the 0 – 40 Hz range,

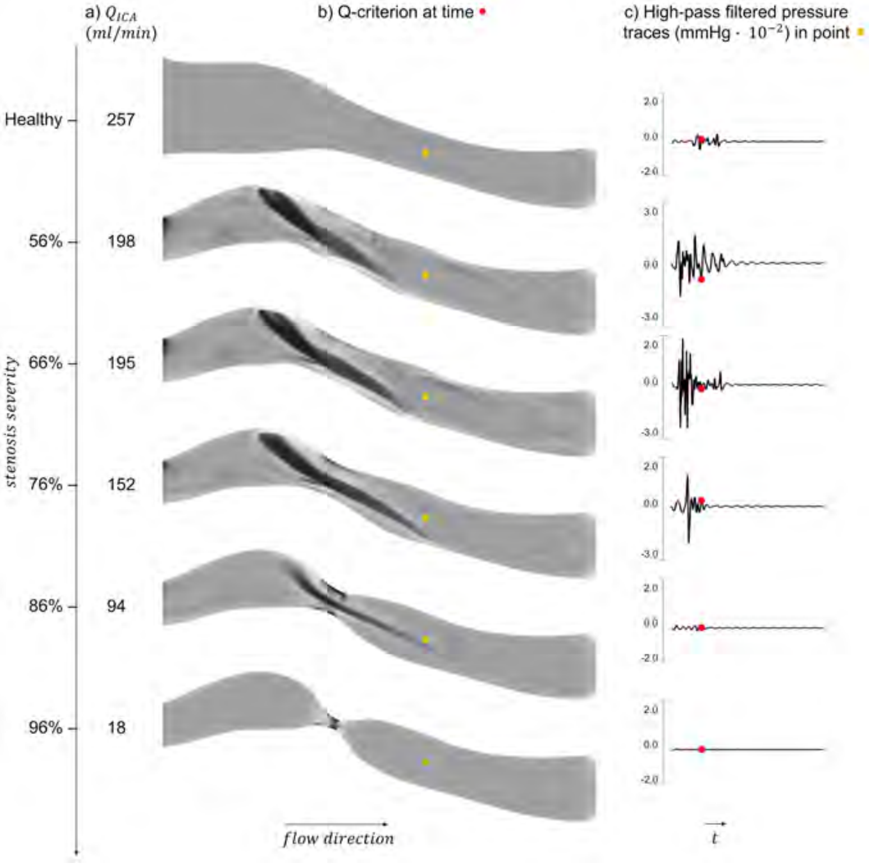

Figure 6.7: The used Q_{ICA} is reported (a) in correspondence of the vortexes in the ICA region, identified using the Q-criterion (b), of each model (category "degree of stenosis"). The volumetric rendering of the Q-criterion was obtained at a fourth of the simulated cycle, highlighted by the red dot on the high-pass pressure traces displaced in panel c), which were obtained at point **P** (yellow square). As expected, the jet of the flow does not break down when entering the stenosis in the healthy geometry, while numerous vortexes arise in the 56 %, 66 % and 76 % stenoses. The flow in the 86 % stenosis is also unstable but less than the 56-76 % stenoses. In the 96 % geometry, on the other hand, the weak instabilities dissipate closely downstream of the narrowing.

which was therefore chosen as the relevant frequency range for discerning severe stenoses from healthy carotid arteries. Furthermore, we observe that the power of the healthy and the severe stenoses reaches approximately zero at 80 Hz, while the energy content of the moderate stenoses is non-negligible until 200 Hz . Therefore, the $IFI_{[80Hz,200Hz]}$ could be used as indicator for the presence of moderate stenoses. The sensitivity and specificity of $IFI_{[0Hz,40Hz]}$ and $IFI_{[80Hz,200Hz]}$ for the detection of severe and moderate stenoses, respectively, was investigated in the following chapters.

6.3.3.2 *LDV for Stenosis Detection: Proof-of-concept*

Based on these preliminary findings, we performed a total of four linear regression analyses between Q_{ICA} and the CFD-based IFIs, for stenotic and healthy models separately, with $IFIs$ evaluated at both frequency ranges. The correlation was found to be high for all cases, with $R^2 > 0.89$, as reported in Table 6.4. The regression coefficients (Table 6.4) were used to obtain $IFI'_{[0Hz,40Hz]}$ and $IFI'_{[80Hz,200Hz]}$ from Q_{ICA} of the fictitious population. The probability density functions of the fictitious population were evaluated for both frequency ranges and reported in Figure 6.8b. The probability density functions represent the distribution of the diseased and healthy groups, therefore, providing insights on the forecast probability of each classifier, i.e. $IFI'_{[0Hz,40Hz]}$ and $IFI'_{[80Hz,200Hz]}$. On the left side, the distribution of the healthy fictitious population overlaps only partially on the 86 % stenosis, and not at all on the 96 %, showing promising possibilities for the $IFI'_{[0Hz,40Hz]}$ as indicator for severe stenoses, but less so for moderate stenoses. On the other hand, the distribution of the healthy population obtained for $IFI'_{[80Hz,200Hz]}$ (Figure 6.8b, right side) overlaps only marginally with the moderate stenoses but almost completely the severe stenoses, showing that $IFI'_{[80Hz,200Hz]}$ could be used to identify moderate stenoses but not severe ones. Therefore, the probability density functions suggest that it could be possible to infer the presence of moderate and severe stenoses by using the $IFIs'$ evaluated at high and low frequency ranges, respectively, as classifiers. We, therefore, based our ROC analysis by evaluating IFI' in the 80 - 200 Hz and 0 - 40 Hz range, see Figure 6.8c, left and right panel, respectively. The reference probability line is added to both plots, showing that the accuracy of the $IFIs'$ is higher than a predictor which makes random guesses (AUC = 0.50). As expected from the probability density functions plots, the ROC analysis shows that $IFI'_{[0Hz,40Hz]}$ infers the presence of severe stenoses with AUC = 0.97, while $IFI'_{[80Hz,200Hz]}$ infers the presence of moderate stenosis with AUC = 0.84. The AUC of each curve is reported in Table 6.2. From Youden Index we have that the optimal cut-off value is $IFI'_{[0Hz,40Hz]}$ = -3.96 with Sp = 92 % and Sn = 99 %, and $IFI'_{[80Hz,200Hz]}$ = -6.91 with Sp = 73 % and Sn = 96 %.

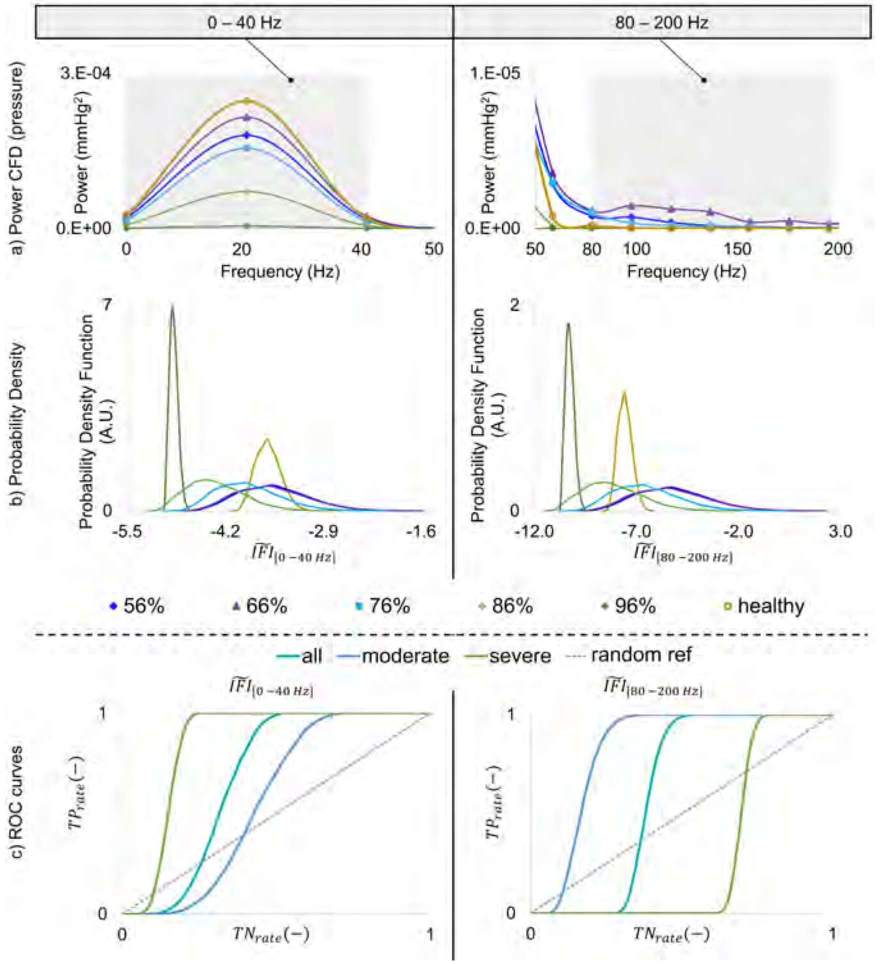

Figure 6.8: The CFD data evaluated in the 0 – 40 Hz and in the 80 – 200 Hz ranges is reported on the left and right side, respectively. (a) The power of the pressure fluctuations obtained from the six CFD simulations in category "degree of stenosis" (mean Q_{CCA} and Q_{ICA}/Q_{CCA}) is plotted in two frequency ranges (identified by the gray boxes), highlighting a difference in the energy content of the moderate (56 %,66 % and 76 %) and severe (86 % and 96 %) stenoses. (b) The probability density distributions, obtained from the extended population by means of regression analyses in each range, show that by evaluating IFI in two separate frequency ranges, it is possible to distinguish the moderate and severe stenoses from the healthy model. (c) The ROC curves show that the accuracy of severe and moderate stenosis prediction using IFI'_{0-40Hz} and $IFI'_{80-200Hz}$, respectively, is higher than the one of a random predictor with 50% chance of detection.

Frequency Range	**Model**	R^2	$\mathbf{a \cdot 100}$	**b**
f_{min} = 0 Hz	Stenotic	0.89	0.739	-5.016
f_{max} = 40 Hz	Healthy	0.99	0.286	-4.361
f_{min} = 80 Hz	Stenotic	0.89	2.803	-10.770
f_{max} = 200 Hz	Healthy	0.96	0.602	-9.905

Table 6.4: The correlation between Q_{ICA} and $IFI_{[f_{min},f_{max}]}$ evaluated at the two frequency ranges was found to be extremely high (R^2 at least 0.89). The regression coefficients (a, b) were used to obtain the IFI' values in both frequency ranges and for each subject of the fictitious population using the expression $IFI'_{[f_{min},f_{max}]} = a \cdot Q_{ICA} + \mathrm{b}$.

6.4 DISCUSSION

6.4.1 Validation Strategy

The results in this paper were based on using the computed pressure traces as proxy for wall vibrations, which we validated against in-vitro data. The correlation between the two datasets is 0.9819.

Interestingly, the IFI was found to be unaffected by which physical quantity it was calculated from. The experimental data referred to displacement recorded using LDV on the surface of a soft-tissue-mimicking gel, which embedded a compliant replica of the carotid arteries. The computational data, on the other hand, consisted of pressure fluctuations. During the experiments, in-vitro intra-arterial pressure was also measured. However, the presence of pressure catheters significantly affected the flow field and thereby made any comparison with the simulated flow field not relevant.

Our findings also suggest that the material properties of the compliant experimental model and the rigid-walls computational model did not affect the turbulent flow field, as similar flow fields were obtained from the two datasets. Note also that, despite the mentioned differences, the characteristic frequencies for the turbulent-like flow are in the $<$ 200 Hz region for both the numerical and experimental data [103].

6.4.2 Computational Model

Using our computational resources, we were able to evaluate the flow field of several stenosis severities throughout 21 CFD simulations, specifically 18 for the stenosed models and 3 for the healthy one.

There have been multiple CFD studies performed on a cohort of patients affected by carotid stenosis [158], [159]. However, they mainly focused on wall shear stress and disease progression. To the best of our knowledge, this is the first study focusing on how the intensity of turbulent-like post-stenotic flow varies with flow rate, flow split, and degree of stenosis. The current study was limited to a Newtonian formulation of the blood, but the effect of using a non-Newtonian fluid on the flow field of the carotid bifurcation was found to be negligible, due to the high shear rates that force the models to work in a quasi-constant viscosity regime [131]. Furthermore, Khan et al. [111], [155] observed that assuming viscosity as a constant value has a negligible practical impact on the turbulent flow field.

6.4.3 Healthy Model

Another important aspect of this paper was the comparison between the healthy and diseased models. The healthy model did not harbor flow instabilities despite the relatively high Q_{ICA}, showing how strongly the presence of a stenosis affects the flow field. Of note is that the flow field in the healthy model was different already upstream of the area where the stenosis would occur, as due to the growth of the atherosclerotic plaques. The Computer Tomography Angiography images [115] showed the presence of hypo-cellular and calcified plaques spread along the ICA since its attachment to the carotid bifurcation, highlighting that what we consider a stenosis is actually the location with the most extreme narrowing. It is well known that the arteries of patients affected by atherosclerosis are overall narrower than the same artery prior to the growth of the plaque. Consequently, the differences in fluid dynamics among a healthy and a stenotic patient are even more marked, explaining the absolute absence of vortexes in the healthy model despite the comparable Q_{ICA}.

6.4.4 Reynolds Number

As expected, the linear regression analysis between Q_{ICA} and $IFI_{[f_{min},f_{max}]}$ in the 20 Hz - 10 kHz range showed that the Reynolds number is an equally good correlation metric for the presence of flow instabilities as Q_{ICA}. Despite its limited use in the clinical practice, the $Re_{stenosis}$ is still relevant from an engineering point of view. We therefore performed the ROC analysis using $Re_{stenosis}$ as metric for IFI evaluated at same frequency ranges as Q_{ICA}. We found that there was little to no impact on sensitivity and specificity, as the results were in agreement with those obtained with Q_{ICA}, with AUC = 0.82 and 0.85 for moderate and severe stenoses, respectively. Thus, as expected, confirming the strong correlation between $Re_{stenosis}$ and the intensity of flow instabilities at any stenosis degree.

6.4.5 Fictitious Population

Using the linear regressions, we could create a fictitious population and perform ROC analyses. We did this considering two frequency bands: $IFI'_{[0Hz,40Hz]}$ and $IFI'_{[80Hz,200Hz]}$. Of note is that nine additional frequency bands were considered, ranging within the entire simulated frequency domain (0 - 10 kHz), but our data indicates that the 0 - 40 Hz range best reveals information on the flow rate, while the higher 80 - 200 Hz frequency band finely reveals the presence of flow instabilities. In our analysis, both were needed to discriminate a stenosed from a non-stenosed vessel because of the flow limiting character of severe stenosis. Indeed, when using $IFI'_{[80Hz,200Hz]}$, the curve for severe stenoses is consistently below the 50 % probability reference line.

We found low sensitivity when detecting extremely severe stenoses using flow instabilities, which agrees with several clinical studies. For instance, the sensitivity for auscultation of asymptomatic carotid stenosis was found to be 29 % by Johannson et al. (2008) [160]. McColgan et al (2012) also noticed that the likelihood of carotid bruit does not increase with stenosis degree [14]. These findings suggest that evaluations based on carotid bruits, i.e. flow instabilities, are not sufficient to exclude the presence of extremely severe carotid stenosis.

However, it is worth noticing that by combining the $IFI'_{[80Hz,200Hz]}$ and the $IFI'_{[0Hz,40Hz]}$ data, and using a simple linear classifier, we were able to achieve a perfect classification of our fictitious population, i.e., AUC = 1.0 and a specificity and sensitivity of 100 %.

6.4.6 Future Work

Verification and validation of computer models have been a subject of struggle for the modeling and simulations community since the 1960s [161]. If applicable, comparisons should be made using well-known benchmarks or well-understood techniques in order to accurately quantify the uncertainties [97]. The U.S. Food and Drug Administration (FDA) designed a nozzle benchmark for the validation of CFD models applied to generic medical devices,[162] and asked the CFD community to perform validation simulations in 2008-2009. However, a large inter-laboratory disagreement was found in the predicted breakdown location of turbulent jet for transitional flow regimes. Several studies argued that the discrepancy was due to the lack of measured boundary conditions, which prevented numerical reproducibility [163], as the experimental noise could have triggered the onset of turbulence whereas the idealized boundary conditions would not [102]. It is indeed well established that the environment in which validation experiments are conducted, as being the quantification of the ability of a computer model to replicate the physics of the investigated problem their primary purpose, should be carefully controlled and measured in order to guarantee inter-laboratory repeatability [40]. In this context, our validation strategy lacked on the numerical reproducibility as much as the FDA benchmark did, as the computational boundary conditions set in our models are based on idealized values as well. Our primary purpose, however, was restricted to the validation of a single computer model whose specific purpose was to obtain a set of intensity of flow instabilities large enough to allow a statistically significant analysis of the ability of an LDV device to detect stenosis. As such, we were not interested in the absolute value of IFI, but rather in the correlation to geometric and flow rate parameters, i.e. Q_{ICA} or $Re_{stenosis}$. In order to encourage further discussion on the subject and promote openness in science, we point out the availability of the experimental dataset in an online repository [164].

The pressure traces show that flow instabilities are particularly intense after the systolic peak, and almost never present in the diastolic phase of the cardiac cycle. Future work may also consider performing a temporal analysis of the traces, focusing on specific moments during the cardiac cycle, to look for frequency-dependent features. In this context, it is relevant to mention the study of Palmen et al. [165] which found significant secondary flow field and an unstable shear layer behavior during systolic deceleration and in the initial phase of diastole, and a quasi-static situation at end-diastole.

We obtained the fictitious population on which the ROC analysis was performed by using the correlation coefficients of the Q_{ICA} of 21 CFD simulations (18 stenotic, three healthy) and the IFI. Obviously, the number of CFD simulations included in this study had an immediate impact on the accuracy of the correlation. The number of simulations was kept as small as possible due to the surge of CPU hours demanded by each additional one. It is practically unfeasible to run enough simulations to cover all combinations of CCA flow rate, ICA flow split and stenosis degree. A larger set of simulations run on a broader population could allow for a more accurate estimate of the correlation coefficients. We made sure to run at least two simulations per stenosis degree, in order to improve the reliability of our regression model as predictor for the presence of carotid stenosis. Exceptionally, we included only one simulation run on the 96 % stenosis model because no difference in IFI was noticeable when increasing the Q_{CCA} to 2 SD (i.e. Q_{ICA} = 27 ml/min), suggesting that the extremely severe stenosis could not harbor flow instabilities in physiologically varying ICA flow rates. Furthermore, we run only three simulations with the healthy model as a consequence of the choice to investigate only the flow rate levels appropriate for stenotic models. It is worth noticing, however, that small flow instabilities were found in the healthy model for ICA flow rates on the high side of its physiological range Q_{ICA} = 351.8, corresponding to + 2 SD.

The sensitivity and specificity measured in our fictitious feasibility studies outperform clinical studies using auscultation. The association between carotid bruit, related to the presence of flow instabilities, and carotid stenosis was found to have an average Sn = 53 % and Sp = 83 % over 26 clinical studies [14]. Although our results are more encouraging than previous in-vivo studies, we have to point out that our study excludes all the variation from patient-specific geometry and neck skin properties. The findings in this study are based on only one set of patient-specific clinical images, with its unique tortuosity and plaque morphology. Patient-specific anatomical aspects such as curvature, non-planarity and tortuosity of carotid arteries, and the distance of the ICA stenosis from the carotid bifurcation, might have an impact on the onset of flow instabilities, and on the identified frequency bands and metrics. Caution is therefore warranted in interpreting the findings and a further extension of the study with additional patient-specific data would strengthen the theoretical basis. At the same time, the proof-of-concept character of the work should be kept in mind, where we wanted to explore the discriminative power of a frequency-domain analysis of features induced by post-stenosis flow instabilities in an experimental and CFD model. The effective sensitivity and specificity of the technique will always have to be based on an in-vivo study, irrespective of any computational study.

In this study, we assess the inter-patient variability of IFI values. However, when performing in-vivo measurements, it might be more relevant to quantify the intra-patient variability of IFI values by comparing the measurement obtained from both carotid arteries. From a mathematical point of view, this would be a 'patient-specific' normalization of the data, which hopefully would reduce the impact of geometry and neck skin properties.

Finally, caution is warranted when interpreting our results from the collection of fictitious subjects. Our approach is only intended as a rough estimate of the sensitivity and specificity for each degree of stenosis. One cannot draw any direct clinical conclusions from these results, but could help guiding future exploratory clinical trials. Furthermore, given the intrinsic limitations of in-silico and in-vitro studies, the effective potential of this theoretically validated technique should be followed up and validated by clinical studies. If our feasibility results would be found to be applicable in-vivo, the use of such device in the clinical practice could improve early carotid stenosis detection.

6.5 CONCLUSIONS

We have performed CFD simulations in a patient-specific carotid bifurcation geometry in order to evaluate the feasibility of LDV to infer carotid stenosis. Specifically, we evaluated the flow field obtained by different degrees of stenosis in the internal carotid artery, subjected to boundary conditions spanning the physiological range. We introduced the IFI as a measure to quantify the intensity of downstream fluctuations. We have demonstrated that the flow rate in the stenosed artery is a major determinant of downstream flow instabilities, which arise quite intensely in moderate stenoses (56 % to 76 %). Interestingly, bulk flow could also be used to identify the most stenotic carotid arteries. The accuracy of moderate and severe stenoses detection by means of an LDV device was found to be encouraging. Noticeably, the pressure-based CFD analysis parallels the analysis of experimental data in the same geometrical model embedded in a gel, where the relation between trans-stenotic flow and intensity of vibrations at the gel surface was studied. These results support the feasibility of the use of LDV to infer asymptomatic carotid stenosis, pending validation via clinical trials.

6.6 Acknowledgements

The study was done within the context of the H2020 European funded 644798 CARDIS project. We greatly acknowledge the contribution of the entire consortium and the teams behind the development and construction of the multi-array prototype.

This work was also carried out as a part of the Centre for Cardiological Innovation, and SIMMIS, project number 262827, funded by the Research Council of Norway. Computations were performed on the Abel Cluster, owned by the University of Oslo and the Norwegian metacenter for High Performance Computing (NOTUR), and operated by the Department for Research Computing at USIT, the University of Oslo IT-department, grant number nn9316k.

We also acknowledge the important contribution from late professor Jan Vierendeels.

CONCLUSIONS

The objective of the current work was to provide a proof of principle concerning the ability of a Laser Doppler Vibrometer device to infer the presence of carotid stenosis. We explored it by integrating computational techniques with an experimental methodology.

RESEARCH GOALS

Goal 1 *- Implementation of an efficient numerical model able to reliably replicate the flow field in a stenosed carotid artery*

Computational Fluid Dynamics is an extremely powerful investigation technique, as it allows to obtain a complete description of pressure and velocity fields in the entire fluid domain [86]. However, the efficacy of CFD relies on the robustness of the numerical methods, especially for transitional flows [102]. The choice of the correct numerical methodology is hence crucial for reliable simulations.

Direct Numerical Simulations with rigid walls are widely used for biomedical applications with complex or transitional flow fields [74], [102], [111]–[114]. Therefore, we firstly focused on finding an adequate DNS solution from a spatial and temporal refinement study with respect to the smallest scales, and from a pragmatic biomedical engineering point of view. The numerical methodology applied in this study allowed us to properly resolve the flow field of a stenosed patient-specific carotid bifurcation and hence detect instabilities induced by the stenosis.

However, directly calculating the smallest scales of the turbulent-like flow requires large computational resources. Therefore, sub-grid scale models are often used to model the smallest scales. The resulting LES simulation leads to a lower computational cost. However, LES simulations depend on the properties of the SGS model. In the chapter 4, we have shown that, when compared to the reference DNS solution, only Sigma and Dynamic Smagorinsky models were able to replicate the averaged mean flow features from the constant flow rate simulation, and the turbulent flow features in the pulsatile flow rate simulations. The computational cost was lower for the Sigma model, and therefore the best choice balancing accuracy with computational cost for studying high frequency flow instabilities. However, for higher Reynolds numbers, similar to the constant flow rate simulation, the LES models were not sufficient.

Future efforts on this subject should be conducted with the above mentioned SGS model, while taking advantage of a robust high-order numerical solver such as the one used in this study.

Goal 2 - *Development of an experimental stenosed carotid artery model to obtain LDV traces*

Our aim was to evaluate the ability of the LDV prototype, developed within the CARDIS project, to detect a stenosis. Specifically, we aimed to determine whether the presence of a stenosis leads to high frequency fluctuations in the recorded LDV signals and, if so, to assess the frequency range where such fluctuations would have to be sought.

In the hydraulic bench model study of a carotid artery reported in chapter 5, we have shown that post-stenotic flow instabilities induce vibrations that can be detected from surface measurements using laser Doppler vibrometry. The statistical analysis showed that the LDV was able to distinguish different flow levels in the envisioned range, as could the pressure probe, with a comparable sensitivity. We found that there seems to be very little energy in the signals beyond 200 Hz. Furthermore, our data suggest that the 0 - 200 Hz range covers the frequency band within which to seek the footprint of the stenosis.

Goal 3 - *Validation of the numerical model against the collected experimental measurements*

We aimed to validate the numerical methodology, in order to determine whether it was able to replicate the physics of the real world. In order to do so, we compared the experimental LDV signals with the computed pressure traces for the patient-specific 76 % stenotic model.

For both datasets, the fluctuations were present and increased with the flow rate, and the same applied to their power. Furthermore, the logarithm of their integral in the 20 Hz - 10 kHz range displayed a similar linear trend, increasing with ICA flow rate, suggesting that the intensity of the pressure fluctuations, as obtained from the CFD simulations, can be used as a proxy for the intensity of wall vibrations as measured with LDV. The two datasets were found to be in good agreement, with a concordance correlation coefficient higher than 0.98.

We could, therefore, conclude that our computational methodology provides plausible results, and we could hence use CFD simulations to investigate a larger set of parameters.

Goal 4 *- Conduction of a parametric study on the intensity of downstream-stenosis flow instabilities*

We aimed to assess which metric best correlates with the level of flow instabilities. Using our computational resources, we were able to evaluate the flow field of several stenosis severities throughout 21 CFD simulations, specifically 18 for the stenosed models and 3 for the healthy one.

We performed regression analyses between the intensity of flow instabilities in the most relevant frequency interval (as found from the experimental study) and CCA flow rate, ICA flow rate, ICA flow split, stenosis area, flow velocity and Reynolds number at the stenosis throat. The ICA flow rate was found to be the strongest correlator with the intensity of downstream stenosis flow instabilities, with a R^2 of 0.90. The model of the healthy artery (reconstructed based on clinical images), on the other hand, did not harbor flow instabilities despite the relatively high ICA flow rate, showing how strongly the presence of a stenosis affects the flow field.

Goal 5 *- Obtaining a quantitative prediction of the feasibility of stenosis detection using LDV*

We have demonstrated that the flow rate in the stenosed artery is a major determinant of downstream flow instabilities, which arise quite intensely in moderate stenoses (56 % to 76 %) in the high frequency range (80 - 200 Hz). We found low sensitivity when detecting extremely severe stenoses using flow instabilities, which agrees with several clinical studies. However, bulk flow (low frequency range: 0 - 40 Hz) could also be used to identify the most stenotic carotid arteries. The accuracy of moderate and severe stenoses detection using an LDV device was found to be encouraging.

These results support the feasibility of the use of LDV to infer asymptomatic carotid stenosis, pending validation via clinical trials.

WHAT ABOUT THE CLINICAL PRACTICE?

As not unusual in the computational field, the translation of models to the clinical setting is rather complex, due to the intrinsic idealization of the physiological problems.

Specifically, the findings in this study are based on only one set of patient-specific clinical images, with its unique tortuosity and plaque morphology. Patient-specific anatomical aspects such as curvature, non-planarity and tortuosity of carotid arteries, and the distance of the ICA stenosis from the carotid bifurcation, might have an impact on the onset of flow instabilities, and on the identified frequency bands and metrics.

In this respect, we performed the current study as a proof of concept of the feasibility of using LDV to detect stenosis, and it was not our intention to translate this to the clinic. Nevertheless, we were able to provide physics-based guidelines on the importance of investigating two different frequency ranges for the detection of different degrees of stenosis. However, the direct applicability of our methodology to the data recorded on patients is, as a reviewer correctly pointed out, to be demonstrated, despite our efforts to simulate as many physiologically plausible conditions as allowed by the computational resources. We nonetheless believe that the main results of the current study will be relevant for follow-up research and provide guidance for signal processing strategies that will, most likely, be complemented with artificial intelligence and machine learning methods.

TAKE-HOME MESSAGE

The accuracy of moderate and severe stenoses detection using an LDV device was found to be encouraging. If our feasibility results would be found to be applicable in-vivo, the use of such device in the clinical practice could improve early carotid stenosis detection.

BIBLIOGRAPHY

[1] 'World Health Statistics 2018 - Monitoring Health for the SDGs', Tech. Rep., 2018, p. 100.

[2] M. L. Flaherty, B. Kissela, J. C. Khoury, K. Alwell, C. J. Moomaw, D. Woo, P. Khatri, S. Ferioli, O. Adeoye, J. P. Broderick and D. Kleindorfer, 'Carotid Artery Stenosis as a Cause of a Stroke', *Neuroepidemiology*, vol. 40, no. 1, pp. 36–41, 2013.

[3] G. Raman, G. D. Kitsios, D. Moorthy, N. Hadar, I. J. Dahabreh, T. F. O'Donnell, D. E. Thaler, E. Feldmann and M. Joseph Lau, 'Management of Asymptomatic Carotid Stenosis', *AHRQ Technol. Assessments*, vol. 1, no. 1, pp. 1–69, 2012.

[4] E. Touzé, C. P. Warlow and P. M. Rothwell, 'Risk of coronary and other nonstroke vascular death in relation to the presence and extent of atherosclerotic disease at the carotid bifurcation', *Stroke*, vol. 37, no. 12, pp. 2904–2909, 2006.

[5] M. P. Colgan, G. R. Strode, J. D. Sommer, J. L. Gibbs and D. S. Sumner, 'Prevalence of asymptomatic carotid disease: results of duplex scanning in 348 unselected volunteers', *J Vasc. Surg*, vol. 8, no. 6, pp. 674–678, 1988.

[6] P. Prati, D. Vanuzzo, M. Casaroli, A. Di Chiara, F. D. Biasi, G. A. Feruglio and P.-J. Touboul, 'Atherosclerosis in a General Population', *Stroke*, vol. 23, no. 12, pp. 1705–1711, 1992.

[7] G. Lanzino, A. A. Rabinstein and R. D. Brown Jr, 'Treatment of Carotid Artery Stenosis: Medical Therapy, Surgery, or Stenting?', *Mayo Clin. Proc.*, vol. 84, no. 4, pp. 362–368, 2009.

[8] S. A. Ahmed and D. P. Giddens, 'Flow Disturbance Measurements Constricted Tube at Moderate Numbers', *J. Biomech.*, vol. 16, no. 12, pp. 955–963, 1983.

[9] S.-W. Lee, L. Antiga, J. D. Spence and D. A. Steinman, 'Geometry of the carotid bifurcation predicts its exposure to disturbed flow', *Stroke*, vol. 39, no. 8, pp. 2341–2347, 2008.

[10] K. W. Beach, R. O. Bergelin, D. F. Leotta, J. F. Primozich, P. M. Sevareid, E. T. Stutzman and R. E. Zierler, 'Standardized ultrasound evaluation of carotid stenosis for clinical trials: University of Washington Ultrasound Reading Center', *Cardiovasc. Ultrasound*, vol. 8, no. 39, pp. 1–15, 2010.

[11] S. A. Ahmed and D. P. Giddens, 'Velocity Measurements in Steady Flow Through Axisymmetric Stenoses at Moderate Reynolds Number', *J. Biomech.*, vol. 16, pp. 505–516, 1983.

[12] S. S. Varghese, S. H. Frankel and P. F. Fischer, 'Direct numerical simulation of stenotic flows. Part 2. Pulsatile flow', *J. Fluid Mech.*, vol. 582, p. 281, 2007.

[13] M. Naghavi, A. Abajobir and C. Abbafati, 'Global, regional, and national age-sex specifc mortality for 264 causes of death, 1980-2016: A systematic analysis for the Global Burden of Disease Study 2016', *Lancet*, vol. 390, no. 10100, pp. 1151–1210, 2017.

[14] P. McColgan, P. Bentley, M. McCarron and P. Sharma, 'Evaluation of the clinical utility of a carotid bruit', *QJM*, vol. 105, no. 12, pp. 1171–1177, 2012.

[15] J. S. Sauve, K. E. Thorpe, D. L. Sackett, W. Taylor, H. J. Barnett, R. B. Haynes and A. J. Fox, 'Can bruits distinguish high-grade from moderate symptomatic carotid stenosis? The North American Symptomatic Carotid Endarterectomy Trial.' *Ann. Intern. Med.*, vol. 120, no. 8, pp. 633–637, 1994.

[16] M. De Melis, U. Morbiducci, L. Scalise, E. P. Tomasini, D. Delbeke, R. Baets, L. M. Van Bortel and P. Segers, 'A Noncontact Approach For The Evaluation of Large Artery Stiffness: A Preliminary Study', *Am. J. Hypertens.*, vol. 21, no. 12, pp. 1280–1283, 2008.

[17] L. Scalise, M. De Melis, U. Morbiducci, P. Segers and E. P. Tomasini, 'From Cardiac to Respiratory Rate, from Cardiac Sounds to Pulse Velocity: a Noncontact Unified Approach for the Monitoring of Vital Signs By Means of Optical Vibrocardiography', in *Proc. Soc. PHOTO-OPTICAL Instrum. Eng.*, vol. 7098, 2008, pp. 1–1.

[18] U. Morbiducci, L. Scalise, M. De Melis and M. Grigioni, 'Optical Vibrocardiography: A Novel Tool for the Optical Monitoring of Cardiac Activity', *Ann. Biomed. Eng.*, vol. 35, no. 1, pp. 45–58, 2007.

[19] Y. Li, 'Miniaturized Laser Doppler Vibrometer Integrated on a Silicon Photonics Platform', PhD thesis, 2013.

[20] Y. Li, P. Segers, J. Dirckx and R. Baets, 'On-chip laser Doppler vibrometer for arterial pulse wave velocity measurement', *Biomed. Opt. Express*, vol. 4, no. 7, p. 1229, 2013.

[21] Y. Li, J. Zhu, M. Duperron, P. O'Brien, R. Schüler, S. Aasmul, M. de Melis, M. Kersemans and R. Baets, 'Six-beam homodyne laser Doppler vibrometry based on silicon photonics technology', *Opt. Express*, vol. 26, no. 3, p. 3638, 2018.

[22] D. Tommasin, A. Caenen, B. Verhegghe, S. E. Greenwald and P. Segers, 'Physics of Within-Tissue Wave Propagation Generated by Pulse Propagation in the Carotid Artery', *Appl. Sci.*, vol. 9, no. 2878, pp. 1–19, 2019.

[23] H2020, 'Early stage cardiovascular disease detection with integrated silicon photonics', in *https://cordis.europa.eu/project/id/644798*.

[24] E. N. Marieb and K. Hoehn, 'Human anatomy and Physiology 9th Edition', 9th. Pearson, 2012, pp. 692–698.

[25] R. E. Klabunde, 'Cardiovascular Physiology Concepts - second edition', 9. 2012, vol. 53, pp. 1–243.

[26] S. Standring, 'Gray's Anatomy - The Anatomical Basis of Clinical Practice - 39th Edition', October. 2006, vol. 78, pp. 329–335.

[27] M. J. Nawrocki, B. Perek, P. Sujka-Kordowska, A. Konwerska, S. Kałużna, P. Zawierucha, M. Bruska, M. Zabel, M. Jemielity, M. Nowicki, B. Kempisty and A. Malińska, 'Differences in expression of genes involved in bone development and morphogenesis in the walls of internal thoracic artery and saphenous vein conduits may provide markers useful for evaluation graft patency', *Int. J. Mol. Sci.*, vol. 20, no. 19, 2019.

[28] J. R. Cameron, J. G. Skofronick and R. M. Grant, 'Physics of the Body', Second Edi. Medical Physics Publishing, 1999, pp. 1–394.

[29] D. J. Eder, L. S. Kaminsky and Bertramm John W., 'Laboratory Atlas of Anatomy and Physiology, 4th Edition'. 2003, pp. 1–192.

[30] P. Lacolley, V. Regnault, P. Segers and S. Laurent, 'Vascular smooth muscle cells and arterial stiffening: Relevance in development, aging, and disease', *Physiol. Rev.*, vol. 97, no. 4, pp. 1555–1617, 2017.

[31] K. Cieślicki, J. Gielecki and T. Wilczak, 'Redundancy of the main cerebral arteries in morphological variations of the Willis circle', *Neurol. Neurochir. Pol.*, vol. 31, no. 3, pp. 463–474, 1997.

[32] H. Gray, 'Anatomy of the Human Body'. 1918, pp. 1–7563.

[33] Y. Hoi, B. A. Wasserman, Y. J. Xie, S. S. Najjar, L. Ferruci, E. G. Lakatta, G. Gerstenblith and D. A. Steinman, 'Characterization of volumetric flow rate waveforms at the carotid bifurcations of older adults', *Physiol. Meas.*, vol. 31, no. 3, pp. 291–302, 2010.

[34] J. N. Cohn, 'Arterial compliance to stratify cardiovascular risk: More precision in therapeutic decision making', *Am. J. Hypertens.*, vol. 14, no. 8 II, pp. 258–263, 2001.

[35] S. P. Glasser, D. K. Arnett, G. E. McVeigh, S. M. Finkelstein, A. J. Bank, D. J. Morgan and J. N. Cohn, 'Vascular compliance and cardiovascular disease: A risk factor or a marker?', *Am. J. Hypertens.*, vol. 10, no. 10 I, pp. 1175–1189, 1997.

[36] E. Blum, 'Die Querschl : ittsbeziehungen zwischen Stature und Asten im Arteriensystem .' *Pflüger's Arch. für die gesamte Physiol. des Menschen und der Tiere*, vol. 175, pp. 1–19, 1919.

[37] P. Foex and J. W. Sear, 'Hypertension: pathophysiology and treatment', *Contin. Educ. Anaesth. Crit. Care Pain*, no. December 2015, 2004.

[38] S. P. Sutera and R. Skalak, 'The History of Poiseuille's Law', *Annu. Rev. Fluid Mech.*, vol. 25, pp. 1–20, 1993.

[39] W. J. Manning, 'Asymptomatic aortic stenosis in the elderly: A clinical review', *JAMA - J. Am. Med. Assoc.*, vol. 310, no. 14, pp. 1490–1497, 2013.

[40] J. A. Ambrose, S. L. Winters, A. Stern, A. Eng, L. E. Teichholz, R. Gorlin and V. Fuster, 'Angiographie morphology and the pathogenesis of unstable angina pectoris', *J. Am. Coll. Cardiol.*, vol. 5, no. 3, pp. 609–616, 1985.

[41] B. F. Waller, C. M. Orr, J. D. Slack, C. A. Pinkerton, J. Van Tassel and T. Peters, 'Anatomy, histology, and pathology of coronary arteries: A review relevant to new interventional and imaging techniques—Part II', *Clin. Cardiol.*, vol. 15, no. 7, pp. 535–540, 1992.

[42] J. L. Su, S. J. Grainger, C. A. Greiner, S. P. Madden, S. T. Sum, J. E. Muller and R. D. Madder, 'Detection and structural characterization of lipid-core plaques with intravascular NIRS-IVUS imaging', *Interv. Cardiol.*, vol. 7, no. 6, pp. 519–535, 2015.

[43] B. F. Waller, C. M. Orr, J. D. Slack, C. A. Pinkerton, J. Van Tassel and T. Peters, 'Anatomy, histology, and pathology of coronary arteries: A review relevant to new interventional and imaging techniques—Part I', *Clin. Cardiol.*, vol. 15, no. 7, pp. 451–457, 1992.

[44] GBD 2013 Mortality and Causes of Death Collaborators, 'Global, regional, and national age-sex specific all-cause and cause-specific mortality for 240 causes of death, 1990-2013: a systematic analysis for the Global Burden of Disease Study 2013', *Lancet*, vol. 385, no. 9963, pp. 117–171, 2015.

[45] 'Stroke Information Page', *Natl. Inst. Neurol. Disord. Stroke*, vol. 1, no. 1, pp. 1–6, 2018.

[46] J. P. Kistler and L. K. Furie, 'Carotid Endarterectomy Revisited', *New Engl. J. Med. Ed.*, vol. 342, no. 23, pp. 1743–1745, 2000.

[47] R. W. Hobson, W. C. Mackey, E. Ascher, M. H. Murad, K. D. Calligaro, A. J. Comerota, V. M. Montori, M. K. Eskandari, D. W. Massop, R. L. Bush, B. K. Lal and B. A. Perler, 'Management of atherosclerotic carotid artery disease : Clinical practice guidelines of the Society for Vascular Surgery', *J. Vasc. Surg.*, vol. 48, no. 2, pp. 480–486, 2008.

[48] J.-L. Mas, G. Chatellier, B. Beyssen, A. Branchereau, T. Moulin, J.-P. Becquemin, V. Larrue, M. Lièvre, D. Leys, J.-F. Bonneville, J. Watelet, J.-P. Pruvo, J.-F. Albucher, A. Viguier, P. Piquet, P. Garnier, F. Viader, E. Touzé, M. Giroud, H. Hosseini, J.-C. Pillet, P. Favrole, J.-P. Neau and X. Ducrocq, 'Endarterectomy Versus Stenting in Patients with Symptomatic Severe Carotid Stenosis', *N. Engl. J. Med.*, vol. 355, no. 16, pp. 1660–1671, 2006.

[49] J. F. Meschia, T. G. Brott and R. W. Hobson, 'Diagnosis and invasive management of carotid atherosclerotic stenosis', *Mayo Clin. Proc.*, vol. 82, no. 7, pp. 851–858, 2007.

[50] J. W. Norris, C. Z. Zhu, N. M. Bornstein and B. R. Chambers, 'Vascular risks of asymptomatic carotid stenosis', *Stroke*, vol. 22, no. 12, pp. 1485–1490, 1991.

[51] B. R. Chambers and G. Donnan, 'Carotid endarterectomy for asymptomatic carotid stenosis', *Cochrane Syst. Rev.*, vol. 4, 2005.

[52] M. Clinic, *Carotid Artery Disease*, 2007.

[53] M. Naghavi, 'Asymptomatic Atherosclerosis: Pathophysiology, Detection and Treatment', M. Naghavi, D. Berman, E. Falk, Z. Fayad, K. Nasir, M. Budoff, H. Hecht and P. Shah, Eds. Humana Press, 2010, pp. 1–737.

[54] C. Zhu, J.-H. Seo, H. Bakhshaee and R. Mittal, 'A Computational Method for Analyzing the Biomechanics of Arterial Bruits', *J. Biomech. Eng.*, vol. 139, no. 5, pp. 1–9, 2017.

[55] G. Stasi and E. M. Ruoti, 'A critical evaluation in the delivery of the ultrasound practice: The point of view of the radiologist', *Ital. J. Med.*, vol. 9, no. 1, pp. 5–10, 2015.

[56] I. Currie, 'Fundamental Mechanics of Fluids', Fourth Edi. CRC press.

[57] H. Tennekes and J. L. Lumley, 'A First Course in Turbulence'. 1974, pp. 1–3101.

[58] J. D. J. Anderson, 'A history of aerodynamics - and its impact on flying machines'. 1999, pp. 1–494.

[59] Osborne Reynolds, 'An Experimental Investigation of the Circumstances which determine whether the Motion of Water shall be Direct or Sinuous, and of the Law of Resistance in Parallel Channel', vol. 174, pp. 935–982, 1883.

[60] D. F. Young and F. Y. Tsai, 'Flow characteristics in models of arterial stenosis - II. Unsteady flow', *J. Biomech.*, vol. 6, no. 1955, pp. 547–559, 1973.

[61] N. Westerhof, N. Stergiopulos, M. I. Noble and B. E. Westerhof, 'Snapshots of hemodynamics: An aid for clinical research and graduate education. Arterial Stenosis.' *Snapshots Hemodynamics An Aid Clin. Res. Grad. Educ.*, pp. 1–314, 2018.

[62] Y. A. Cengel and J. M. Cimbala, 'Chapter 8: Flow in Pipes', in *Fluid Mech. Fundam. Appl.* 2008, pp. 1–354.

[63] J. R. Womersley, 'Flow in curved pipes.' *J. Physiol.*, vol. 127, pp. 553–563, 1955.

[64] N. Jaensson, 'Experimental analysis of flow in a curved tube using particle image velocimetry', PhD thesis, 2010, pp. 1–22.

[65] R. Baker, 'Internal Fluid Flow: The Fluid Dynamics of Flow in Pipes and Ducts. Review.' *J. Fluid Mech.*, vol. 113, pp. 530–535, 1981.

[66] J. R. Womersley, 'Method for the calculation of velocity, rate of flow and viscous drag in arteries when the pressure gradient is known', *J. Physiol.*, vol. 127, pp. 553–563, 1955.

[67] D. Xu, S. Warnecke, B. Song, X. Ma and B. Hof, 'Transition to turbulence in pulsating pipe flow', *J. Fluid Mech.*, vol. 831, pp. 418–432, 2017.

[68] D. Xu and M. Avila, 'The effect of pulsation frequency on transition in pulsatile pipe flow', *J. Fluid Mech.*, vol. 857, pp. 937–951, 2018.

[69] D. N. Ku, 'Blood Flow in Arteries', *Annu. Rev. Fluid Mech.*, vol. 29, no. 1, pp. 399–434, 1997.

[70] M. H. Friedman, 'Geometric Risk Factors for Arteriosclerosis', in *Johns Hopkins APL Tech. Dig.* 2, vol. 4, 1983, pp. 85–95.

[71] S. Chien, 'Mechanotransduction and endothelial cell homeostasis: The wisdom of the cell', *Am. J. Physiol. - Hear. Circ. Physiol.*, vol. 292, no. 3, 2007.

[72] U. Morbiducci, A. M. Kok, B. R. Kwak, P. H. Stone, D. A. Steinman and J. J. Wentzel, *Atherosclerosis at arterial bifurcations: Evidence for the role of haemodynamics and geometry*, 2016.

[73] H. Chen, A. Selimovic, H. Thompson, A. Chiarini, J. Penrose, Y. Ventikos and P. N. Watton, 'Investigating the Influence on Haemodynamic Stimuli on Intracranial Aneurysm Inception', *Ann. Biomed. Eng.*, vol. 41, pp. 1492–1504, 2013.

[74] K. Valen-Sendstad, M. Piccinelli and D. A. Steinman, 'High-resolution computational fluid dynamics detects flow instabilities in the carotid siphon: Implications for aneurysm initiation and rupture?', *J. Biomech.*, vol. 47, no. 12, pp. 3210–3216, 2014.

[75] P. F. Davies, A. Remuzzitt, E. J. Gordon, C. F. Dewey and M. A. Gimbrone, 'Turbulent fluid shear stress induces vascular endothelial cell turnover in-vitro', *Proc. Natl. Acad. Sci. U. S. A.*, vol. 83, pp. 2114–2117, 1986.

[76] C. K. Zarins, D. P. Giddens, B. K. Bharadvaj, V. S. Sottiurai, R. F. Mabon and S. Glagov, 'Carotid Bifurcation Atherosclerosis: Quantative Correlation of Plaque Localization with Flow Velocity Profiles and Wall Shear Stress', *Circ. Res.*, vol. 53, no. 4, pp. 502–514, 1983.

[77] W. Herrington, B. Lacey, P. Sherliker, J. Armitage and S. Lewington, 'Epidemiology of Atherosclerosis and the Potential to Reduce the Global Burden of Atherothrombotic Disease', *Circ. Res.*, vol. 118, no. 4, pp. 535–546, 2016.

[78] M. Noh, H. Kwon, C. H. Jung, S. U. Kwon, M. S. Kim, W. J. Lee, J. Y. Park, Y. Han, H. Kim, T. W. Kwon and Y. P. Cho, 'Impact of diabetes duration and degree of carotid artery stenosis on major adverse cardiovascular events: A single-center, retrospective, observational cohort study', *Cardiovasc. Diabetol.*, vol. 16, no. 1, pp. 1–9, 2017.

[79] N. Stergiopulos, D. F. Young and T. R. Rogge, 'Computer simulation of arterial flow with applications to arterial and aortic stenoses', *J. Biomech.*, vol. 25, no. 12, pp. 1477–1488, 1992.

[80] B. A. Younis, S. Spring, S. Olaf Neumann and B. Weigand, 'Simulation of flow in an exact replica of a diseased human carotid artery', *Appl. Math. Model.*, vol. 31, no. 11, pp. 2599–2609, 2007.

[81] M. Motomiya and T. Karino, 'Flow patterns in the human carotid artery bifurcation', *Stroke*, vol. 15, no. 1, pp. 50–56, 1984.

[82] S. B. Pope, 'Turbulent Flows'. 2000, vol. 1, pp. 1–771.

[83] S. A. Ahmed and D. P. Giddens, 'Pulsatile Poststenotic flow studies with Laser Doppler Anenometry', *J. Biomech.*, vol. 17, no. 9, pp. 695–705, 1984.

[84] C. A. Rickards and Y. C. Tzeng, 'Arterial pressure and cerebral blood flow variability: Friend or foe? A review', *Front. Physiol.*, vol. 5 APR, no. April, pp. 1–14, 2014.

[85] R. Peyret, 'Handbook of Computational Fluid Dynamics', *Acad. Press*, pp. 1–467, 1996.

[86] P. Moin and K. Mahesh, 'Direct Numerical Simulation: A Tool in Turbulence Research', *Annu. Rev. Fluid Mech.*, vol. 30, pp. 539–578, 1998.

[87] M. Bern and P. Plassmann, 'Handbook of Computational Geometry, Chapter 6: Mesh Generation', *Elsevier Sci. B.V.*, pp. 291–332, 1999.

[88] M. de Berg, M. van Kreveld, M. Overmars and O. Schwarzkopf, 'Computational Geometry'. 1997.

[89] S. Pirola, Z. Cheng, O. A. Jarral, D. P. O'Regan, J. R. Pepper, T. Athanasiou and X. Y. Xu, 'On the choice of outlet boundary conditions for patient-specific analysis of aortic flow using computational fluid dynamics', *J. Biomech.*, vol. 60, no. June, pp. 15–21, 2017.

[90] P. Reymond, F. Merenda, F. Perren and D. Ru, 'Validation of a One-Dimensional Model of the Systemic Arterial Tree', *Am. J. Physiol. - Hear. Circ. Physiol.*, vol. 297, pp. 208–222, 2009.

[91] F. D. Molina-Aiz, H. Fatnassi, T. Boulard, J. C. Roy and D. L. Valera, 'Comparison of finite element and finite volume methods for simulation of natural ventilation in greenhouses', *Comput. Electron. Agric.*, vol. 72, no. 2, pp. 69–86, 2010.

[92] S. S. Varghese, S. H. Frankel and P. F. Fischer, 'Direct numerical simulation of stenotic flows. Part 1. Steady flow', *J. Fluid Mech.*, vol. 582, pp. 253–280, 2007.

[93] I. Mahariq, H. I. Tarman and M. Kuzuoğlu, 'On the Accuracy of Spectral Element Method in Electromagnetic Scattering Problems', *Int. J. Comput. Theory Eng.*, vol. 6, no. 6, pp. 495–499, 2014.

[94] J. L. Guermond, P. Minev and J. Shen, 'An overview of projection methods for incompressible flows', *Comput. Methods Appl. Mech. Eng.*, vol. 195, no. 44-47, pp. 6011–6045, 2006.

[95] M. Mortensen and K. Valen-sendstad, 'Oasis: a high-level/high-performance open source Navier-Stokes solver', *Comput. Phys. Commun.*, vol. 188, pp. 177–188, 2015.

[96] ASME, ‘Guide for verification and validation in computational solid mechanics’, *Am. Soc. Mech. Eng.*, vol. PTC 60, no. V&V 10, pp. 1–15, 2006.

[97] W. L. Oberkampf and C. J. Roy, ‘Verification and Validation in Scientific Computing’, c. Cambridge Press, 2010, pp. 1–767.

[98] F. Nicoud, C. Chnafa, J. Siguenza, V. Zmijanovic and S. Mendez, ‘Large-Eddy simulation of turbulence in cardiovascular flows’, *Lect. Notes Appl. Comput. Mech.*, vol. 84, pp. 147–167, 2018.

[99] C. Meneveau, T. S. Lund and W. H. Cabot, ‘A Lagrangian dynamic subgrid-scale model of turbulence’, *J. Fluid Mech.*, vol. 319, pp. 353–385, 1996.

[100] J. Smagorinsky, ‘General Circulation Experiments with the Primitive Equations - I. The Basic Experiment’, *Mon. Weather Rev.*, vol. 91, no. 3, pp. 99–164, 1963.

[101] V. Mancini, A. W. Bergersen, J. Vierendeels, P. Segers and K. Valen-Sendstad, ‘High-Frequency Fluctuations in Post-Stenotic Patient Specific Carotid Stenosis Fluid Dynamics: A Computational Fluid Dynamics Strategy Study’, *Cardiovasc. Eng. Technol.*, vol. 10, no. 2, pp. 277–298, 2019.

[102] A. W. Bergersen, M. Mortensen and K. Valen-Sendstad, ‘The FDA nozzle benchmark: “In theory there is no difference between theory and practice, but in practice there is”’, *Int. j. numer. method. biomed. eng.*, vol. 35, no. e3150, 2019.

[103] V. Mancini, D. Tommasin, Y. Li, J. W. Reeves, R. Baets, S. E. Greenwald and P. Segers, ‘Detecting carotid stenosis from skin vibrations using Laser Doppler Vibrometry – an in-vitro proof-of-concept’, *PLoS One*, vol. 14, no. 6, pp. 1–17, 2019.

[104] V. Mancini, A. W. Bergersen, K. Valen-Sendstad and P. Segers, ‘Computed Post-Stenotic Flow Instabilities Correlate Phenotypically with Vibrations Measured Using Laser Doppler Vibrometry: Perspectives for a Promising In-Vivo Device for Early Detection of Moderate and Severe Carotid Stenosis.’ *J. Biomech. Eng.*, vol. 142, no. 9, p. 091 007, 2020.

[105] P. M. Rothwell, ‘Atherothrombosis and Ischaemic Stroke’, *Br. Med. J.*, vol. 334, pp. 379–380, 2007.

[106] M. de Weerd, J. P. Greving, B. Hedblad, M. Lorenz, E. Mathiesen, D. O’Leary, M. Rosvall, M. Sutzer, E. Buskens and M. L. Bots, ‘Prevalence Of Asymptomatic Carotid Artery Stenosis In The General Population: An Individual Participant Data Meta-Analysis’, *Stroke*, vol. 41, no. 6, pp. 1294–1297, 2010.

[107] T. M. Magyar, E.-M. Nam, L. Csiba, M. A. Ritter, B. E. Ringelstein and D. W. Droste, 'Carotid artery auscultation – anachronism or useful screening procedure?', *Neurol. Res.*, vol. 24, no. 7, pp. 705–708, 2002.

[108] P. A. G. Sandercock and E. Kavvadia, 'The Carotid Bruit', *Pract. Neurol. - Neurol. sign*, vol. 2, no. 4, pp. 221–224, 2002.

[109] P. J. Roache, K. N. Ghia and F. M. White, 'Editorial policy statement on the control of numerical accuracy', *J. Fluids Eng.*, vol. 108, no. 1, p. 2, 1986.

[110] K. Valen-Sendstad and D. A. Steinman, 'Mind the Gap : Impact of Computational Fluid Dynamics Solution Strategy on Prediction of Intracranial Aneurysm Hemodynamics and Rupture Status Indicators', *Am. J. Neuroradiol.*, vol. 35, no. 3, pp. 536–543, 2014.

[111] M. O. Khan, K. Valen-Sendstad and D. A. Steinman, 'Direct Numerical Simulation of Laminar-Turbulent Transition in a Non-Axisymmetric Stenosis Model for Newtonian vs. Shear-Thinning Non-Newtonian Rheologies', *Flow, Turbul. Combust.*, vol. 102, pp. 43–72, 2019.

[112] ——, 'Narrowing the expertise gap for predicting intracranial aneurysm hemodynamics: Impact of solver numerics versus mesh and time-step resolution', *Am. J. Neuroradiol.*, vol. 36, no. 7, pp. 1310–1316, 2015.

[113] K. Valen-Sendstad, K. A. Mardal and D. A. Steinman, 'High-resolution CFD detects high-frequency velocity fluctuations in bifurcation, but not sidewall, aneurysms', *J. Biomech.*, vol. 46, no. 2, pp. 402–407, 2013.

[114] J. P. Mynard and D. A. Steinman, 'Effect of Velocity Profile Skewing on Blood Velocity and Volume Flow Waveforms Derived From Maximum Doppler Spectral Velocity', *Ultrasound Med. Biol.*, vol. 39, no. 5, pp. 870–881, 2013.

[115] F. Iannaccone, S. De Bock, M. De Beule, F. Vermassen, I. Van Herzeele, P. Verdonck, P. Segers and B. Verhegghe, 'Feasibility of a priori numerical assessment of plaque scaffolding after carotid artery stenting in clinical routine: Proof of concept', *Int. J. Artif. Organs*, vol. 37, no. 12, pp. 928–939, 2014.

[116] *Http://www.nongnu.org/pyformex/doc-0.9/refman.html.*

[117] M. Piccinelli, A. Veneziani, D. A. Steinman, A. Remuzzi and L. Antiga, 'A framework for geometric analysis of vascular structures: Application to cerebral aneurysms', *IEEE Trans. Med. Imaging*, vol. 28, no. 8, pp. 1141–1155, 2009.

[118] H. C. Groen, L. Simons, Q. J. A. van den Bouwhuijsen, E. M. H. Bosboom, F. J. H. Gijsen, A. G. van der Giessen, F. N. van de Vosse, A. Hofman, A. F. W. van der Steen, J. C. M. Witteman, A. van der Lugt and J. J. Wentzel, 'MRI-based quantification of outflow boundary conditions for computational fluid dynamics of stenosed human carotid arteries', *J. Biomech.*, vol. 43, no. 12, pp. 2332–2338, 2010.

[119] F. Nicoud, H. Baya Toda, O. Cabrit, S. Bose and J. Lee, 'Using singular values to build a subgrid-scale model for large eddy simulations', *Phys. Fluids*, vol. 23, no. 8, 2011.

[120] J. Hunt, A. Wray and P. Moin, 'Eddies, Streams and Convergence Zones in Turbulent Flows', *Cent. Turbul. Res. Proc. Summer Progr. 1988*, vol. 193, no. 1970, 1989.

[121] P. D. Welch, 'The Use of Fast Fourier Transform for the Estimation of Power Spectra: A Method Based on Time Averaging Over Short, Modified Periodograms', *IEEE Trans. Audio Electroacoust.*, vol. 15, no. 2, pp. 70–73, 1967.

[122] M. O. Khan, C. Chnafa, D. Gallo, F. Molinari, U. Morbiducci, D. A. Steinman and K. Valen-Sendstad, 'On the quantification and visualization of transient periodic instabilities in pulsatile flows', *J. Biomech.*, vol. 52, pp. 179–182, 2017.

[123] M. Rieth, F. Proch, O. T. Stein, M. W. A. Pettit and A. M. Kempf, 'Comparison of the Sigma and Smagorinsky LES Models for Grid Generated Turbulence and a Channel Flow', *Comput. Fluids*, vol. 99, pp. 172–181, 2014.

[124] R. M. Lancellotti, C. Vergara, L. Valdettaro, S. Bose and A. Quarteroni, 'Large eddy simulations for blood dynamics in realistic stenotic carotids', *Int. j. numer. method. biomed. eng.*, vol. 33, no. 11, pp. 1–14, 2017.

[125] H. Baya Toda, O. Cabrit, K. Truffin, G. Bruneaux, H. B. Toda, O. Cabrit, K. Truffin, G. Bruneaux and F. Nicoud, 'Assessment of subgrid-scale models with an LES-dedicated experimental database : the pulsatile impinging jet in turbulent cross-flow', *Phys. Fluids*, vol. 26, no. 7, 2014.

[126] J. Vierendeels, B. Merci and E. Dick, 'Numerical Study of Natural Convective Heat Transfer With Large Temperature Differences', *Int. J. Numer. Methods Heat Fluid Flow*, vol. 11, no. 4, pp. 329–341, 2001.

[127] C.-F. Chen, R. Lotz and B. Thompson, 'Assessment of numerical uncertainty around shocks and corners on blunt trailing-edge supercritical airfoils', *Comput. Fluids*, vol. 31, no. 1, pp. 25–40, 2002.

[128] V. Mancini, A. W. Bergersen, P. Segers and K. Valen-sendstad, 'Investigating the Numerical Parameter Space for a Stenosed Patient-Specific Internal Carotid Artery Model', *SINTEF Proc.*, vol. 1, no. 2, pp. 133–138, 2017.

[129] A. N. Kolmogorov, 'The Local Structure of Turbulence in Incompressible Viscous Fluid for Very Large Reynolds Numbers', *Proc. R. Soc. A Math. Phys. Eng. Sci.*, vol. 434, no. 1890, pp. 9–13, 1991.

[130] K. Valen-Sendstad, K. A. Mardal, M. Mortensen, B. A. P. Reif and H. P. Langtangen, 'Direct numerical simulation of transitional flow in a patient-specific intracranial aneurysm', *J. Biomech.*, vol. 44, no. 16, pp. 2826–2832, 2011.

[131] S.-W. Lee and D. A. Steinman, 'On the Relative Importance of Rheology for Image-Based CFD Models of the Carotid Bifurcation', *J. Biomech. Eng.*, vol. 129, no. 2, p. 273, 2007.

[132] L. Antiga, B. Ene-Iordache, L. Caverni, G. P. Cornalba and A. Remuzzi, 'Geometric Reconstruction for Computational Mesh Generation of Arterial Bifurcations from CT Angiography', *Comput. Med. Imaging Graph.*, vol. 26, no. 4, pp. 227–235, 2002.

[133] M. P. Brewin, M. J. Birch, D. J. Mehta, J. W. Reeves, S. Shaw, C. Kruse, J. R. Whiteman, S. Hu, Z. R. Kenz, H. T. Banks and S. E. Greenwald, 'Characterisation of Elastic and Acoustic Properties of an Agar-Based Tissue Mimicking Material', *Ann. Biomed. Eng.*, vol. 43, no. 10, pp. 2587–2596, 2015.

[134] L. Taelman, J. Bols, J. Degroote, V. Muthurangu, J. Panzer, J. Vierendeels and P. Segers, 'Differential impact of local stiffening and narrowing on hemodynamics in repaired aortic coarctation: an FSI study', *Med. Biol. Eng. Comput.*, vol. 54, no. 2-3, pp. 497–510, 2016.

[135] V. Mancini, A. W. Bergersen, J. Vierendeels, P. Segers and K. Valen-Sendstad, *High-Frequency Fluctuations in Post-Stenotic Patient Specific Carotid Stenosis Fluid Dynamics: A Computational Fluid Dynamics Strategy Study. figshare. Fileset.* 2018.

[136] A. E. Tejada-Martínez and K. E. Jansen, 'On the interaction between dynamic model dissipation and numerical dissipation due to streamline upwind/Petrov-Galerkin stabilization', *Comput. Methods Appl. Mech. Eng.*, vol. 194, no. 9-11, pp. 1225–1248, 2005.

[137] EHN, 'European Cardiovascular Disease Statistics 2017 edition', *Eur. Hear. Network, Brussels*, p. 192, 2017.

[138] M. de Weerd, J. P. Greving, A. W. F. de Jong, E. Buskens and M. L. Bots, ‘Prevalence of Asymptomatic Carotid Artery Stenosis According to Age and Sex: Systematic Review and Metaregression Analysis’, *Stroke*, vol. 40, no. 4, pp. 1105–1113, 2009.

[139] P. M. Rothwell, R. J. Gibson, J. Slattery, R. J. Sellar, C. P. Warlow and E. Carotid, ‘Equivalence of Measurements of Carotid Stenosis’, *Am. Hear. Assoc.*, pp. 2435–2439, 1994.

[140] P. Likittanasombut, P. Reynolds, D. Meads and C. Tegeler, ‘Volume Flow Rate of Common Carotid Artery Measured by Doppler Method and Color Velocity Imaging Quantification (CVI-Q)’, *J. Neuroimaging*, vol. 16, no. 1, pp. 34–38, 2006.

[141] S. Uematsu, A. Yang, T. J. Preziosi, R. Kouba and T. J. Toung, ‘Measurement of carotid blood flow in man and its clinical application.’ *Stroke*, vol. 14, no. 2, pp. 256–266, 1983.

[142] G. Heinzel, A. Rüdiger, R. Schilling and T. Hannover, ‘Spectrum and spectral density estimation by the Discrete Fourier transform (DFT), including a comprehensive list of window functions and some new flat-top windows’, *Max Plank Inst.*, pp. 1–84, 2002.

[143] P. C. O’Brien and M. A. Shampo, ‘Statistical Considerations for Performing Multiple Tests in a Single Experiment. 4. Performing Multiple Statistical Tests on the Same Data’, *Mayo Clin. Proc.*, vol. 63, no. 10, pp. 1043–1045, 1988.

[144] A. M. Khalifa and D. P. Giddens, ‘Characterization and evolution of poststenotic flow disturbances’, *J. Biomech.*, vol. 14, no. 5, pp. 279–296, 1981.

[145] E. Y. Wong, H. N. Nikolov, R. N. Rankin, D. W. Holdsworth and T. L. Poepping, ‘Evaluation of distal turbulence intensity for the detection of both plaque ulceration and stenosis grade in the carotid bifurcation using clinical Doppler ultrasound’, *Eur. Radiol.*, vol. 23, no. 6, pp. 1720–1728, 2013.

[146] S. Kefayati, D. W. Holdsworth and T. L. Poepping, ‘Turbulence intensity measurements using particle image velocimetry in diseased carotid artery models: Effect of stenosis severity, plaque eccentricity, and ulceration’, *J. Biomech.*, vol. 47, no. 1, pp. 253–263, 2014.

[147] . GBD 2017 Causes of Death Collaborators, ‘Global, regional, and national age-sex-specific mortality for 282 causes of death in 195 countries and territories, 1980–2017: a systematic analysis for the Global Burden of Disease Study 2017’, *Lancet*, vol. 392, no. 10159, pp. 1736–1788, 2018.

[148] H. T. Banks, S. Hu, Z. R. Kenz, C. Kruse, S. Shaw, J. R. Whiteman, M. P. Brewin, S. E. Greenwald and M. J. Birch, 'Model Validation for a Noninvasive Arterial Stenosis Detection Problem', *Math. Biosci. Eng.*, vol. 11, no. 3, pp. 427–48, 2014.

[149] S. S. Varghese and S. H. Frankel, 'Numerical modeling of pulsatile turbulent flow in stenotic vessels.' *J. Biomech. Eng.*, vol. 125, no. 4, pp. 445–460, 2003.

[150] D. A. Steinman, T. L. Poepping, M. Tambasco, R. N. Rankin and D. W. Holdsworth, 'Flow patterns at the stenosed carotid bifurcation: Effect of concentric versus eccentric stenosis', *Ann. Biomed. Eng.*, vol. 28, no. 4, pp. 415–423, 2000.

[151] D. A. Steinman, 'Image-Based Computational Fluid Dynamics Modeling in Realistic Arterial Geometries', *Ann. Biomed. Eng.*, vol. 30, pp. 483–497, 2002.

[152] H. A. Kjeldsberg, A. W. Bergersen and K. Valen-Sendstad, 'morphMan: Automated manipulation of vascular geometries', *J. Open Source Softw.*, vol. 4, no. 35, p. 1065, 2019.

[153] D. Ratanakorn and J. Keandaoungchan, 'Volume flow rate', *Perspect. Med.*, vol. 1-12, no. 1, pp. 203–206, 2012.

[154] M. Conti, C. Long, M. Marconi, R. Berchiolli, Y. Bazilevs and A. Reali, 'Carotid artery hemodynamics before and after stenting: A patient specific CFD study', *Comput. Fluids*, vol. 141, pp. 62–74, 2016.

[155] M. O. Khan, D. A. Steinman and K. Valen-Sendstad, 'Non-Newtonian versus numerical rheology: Practical impact of shear-thinning on the prediction of stable and unstable flows in intracranial aneurysms', *Int. j. numer. method. biomed. eng.*, vol. 33, no. 7, pp. 1–10, 2017.

[156] T. Fawcett, 'An Introduction to ROC Analysis', *Pattern Recognit. Lett.*, vol. 27, no. 8, pp. 861–874, 2006.

[157] W. J. Youden, 'Index for rating diagnostic tests', *Cancer*, vol. 3, no. 1, pp. 32–35, 1950.

[158] Q. Jia, H. Liu, Y. Li, X. Wang, J. Jia and Y. Li, 'Combination of Magnetic Resonance Angiography and Computational Fluid Dynamics May Predict the Risk of Stroke in Patients with Asymptomatic Carotid Plaques', *Med. Sci. Monit.*, vol. 23, pp. 479–488, 2017.

[159] C. M. Schirmer and A. M. Malek, 'Computational Fluid Dynamic Characterization of Carotid Bifurcation Stenosis in Patient-Based Geometries', *Brain Behav.*, vol. 2, no. 1, pp. 42–52, 2012.

[160] E. P. Johansson and P. Wester, ‘Carotid Bruits as Predictor for Carotid Stenoses Detected By Ultrasonography: an Observational Study’, *BMC Neurol.*, vol. 8, pp. 1–8, 2008.

[161] T. H. Naylor and J. M. Finger, ‘Verification of Computer Simulation Models’, *Manage. Sci.*, vol. 14, no. 2, pp. 92–106, 1967.

[162] Https://fdacfd.nci.nih.gov., *Computational Fluid Dynamics Round Robin Study. Benchmark 1.* 2009.

[163] V. Zmijanovic, S. Mendez, V. Moureau and F. Nicoud, ‘About the numerical robustness of biomedical benchmark cases: Interlaboratory FDA’s idealized medical device’, *Int. j. numer. method. biomed. eng.*, vol. 33, no. 1, pp. 1–17, 2017.

[164] V. Mancini, D. Tommasin, Y. Li, J. W. Reeves, R. Beats, S. E. Greenwald and P. Segers, *Detecting carotid stenosis from skin vibrations using Laser Doppler Vibrometry – an in vitro proof-of-concept. figshare. Dataset.* 2019.

[165] D. E. M. Palmen, F. N. van de Vosse, J. D. Janssen and M. E. H. van Dongen, ‘The influence of minor stenoses on the flow in the carotid artery bifurcation’, 1994. 1993, pp. 313–320.